AN ABSTRACT OF THE DISSERTATION OF

Chaitanya Deepak Ghodke for the degree of Doctor of Philosophy in Mechanical Engineering presented on March 4, 2016.

Title: DNS study of Particle-bed–Turbulence Interactions in Oscillatory Flows

Abstract approved: _____

Sourabh V. Apte

Turbulent flows over rough surfaces are encountered in many engineering and geophysical applications. Flows of this nature, due to their increasing technological interests, have been a subject of rigorous investigation in recent years. Of the particular interest to the oceanographic community is the study of turbulent oscillatory flow over rough surfaces, representative of sediment-bed in a coastal environment. In particular, formulation of predictive criteria for onset of sediment motion requires detailed knowledge of the dynamics of the near-bed turbulence structure and resultant variations in the magnitudes and time-scales of the destabilizing drag and lift forces on sediment grains. The primary objectives of this work are (i) to quantify, using high-fidelity numerical experiments, sediment grain–turbulence interactions and (ii) provide data on the temporal variations in the magnitude of drag and lift forces on sediment grains, the time-scales associated with these variations, and their correlations with the near-bed turbulence in an oscillatory flow environment.

To this end, particle-resolved direct numerical simulations (DNS) are performed to investigate the behavior of an oscillatory flow field over a bed of closely packed fixed spherical particles for a range of Reynolds numbers in transitional and rough

turbulent flow regime. Presence of roughness leads to a substantial modification of the underlying boundary layer mechanism resulting in increased bed shear stress, reduction in the near-bed anisotropy, modification of the near-bed sweep and ejection motions along with marked changes in turbulent energy transport mechanisms. Characterization of such resulting flow field is performed by studying statistical descriptions of the near-bed turbulence for different roughness parameters. A double-averaging technique is employed to reveal spatial inhomogeneities at the roughness scale that provide alternate paths of energy transport in the turbulent kinetic energy (TKE) budget. Spatio–temporal characteristics of unsteady particle forces by studying their spatial distribution, temporal auto-correlations, frequency spectra as well as cross-correlations with near-bed turbulent flow variables are reported. Intermittency in the forces by means of impulse is also investigated.

DNS study of Particle-bed–Turbulence Interactions in Oscillatory Flows

by

Chaitanya Deepak Ghodke

A DISSERTATION

submitted to

Oregon State University

in partial fulfillment of
the requirements for the
degree of

Doctor of Philosophy

Presented March 4, 2016
Commencement June 2016

Doctor of Philosophy dissertation of Chaitanya Deepak Ghodke presented on March 4, 2016.

APPROVED:

Major Professor, representing Mechanical Engineering

Head of the School of Mechanical Industrial and Manufacturing Engineering

---

Dean of the Graduate School

I understand that my dissertation will become part of the permanent collection of Oregon State University libraries. My signature below authorizes release of my dissertation to any reader upon request.

Chaitanya Deepak Ghodke, Author

ACKNOWLEDGEMENTS

I owe my gratitude to all those people who have made this dissertation possible and because of whom the circuitous journey of graduate life has indeed been the most enjoyable one that I will cherish forever.

I am deeply indebted to my advisor Prof. Sourabh Apte who has been a tremendous mentor for me. During my time at the Computational Flow Physics Laboratory (CFPL), he gave me the opportunity to study fundamental problems in the field of turbulent flows that were of great practical importance. He inspired me to become an independent researcher and helped me realize the power of critical reasoning. His patience and kindness, as well as immense knowledge of the topic have been invaluable to me. I am also grateful for the continued financial support from the National Science Foundation (NSF-CBET-1133363) and computational resources provided by the Texas Advanced Computing Center.

My sincere thanks must go to Prof. James Liburdy, Prof. Deborah Pence, Prof. Chad Higgins and Prof. Merrick Haller for taking the time out to read this thesis, evaluate and give a critical review of this work. I also wholeheartedly thank Dr. Javier Urzay of Stanford University for agreeing to be a part of my thesis committee and sharing his expertise. The fruitful discussions with him during the Center for Turbulence Research summer program helped me develop a broader perspective to my thesis. I want to express my gratitude to Prof. S. K. Das for introducing me to the world of computational modeling and teaching the fundamental aspects pertaining to this topic. He has been a great mentor who encouraged and inspired me to pursue my doctoral studies. My sincere thanks extend to Prof. Suresh Menon for his support and advice during my master's degree at Georgia Institute of Technology.

I express my gratitude to the administrative staff in the MIME department not only for their prompt support but also for the kind care: Jean Robinson, Phyllis Helvie and Emma Bramwell. I have also benefited a lot from the truly professional support from the IT staff: Leanne Lai and Mike Sander.

The past and present members of the CFPL group have contributed immensely to my personal and professional time at Oregon State University (OSU). I am grateful to Justin Finn and Andrew Cihonski for answering my countless questions time and again and helping me understand the basics I needed to achieve this work. The excellent quality of their research motivated me to excel in my own work. Special thanks to my present lab-mates Xiaoliang He (Bryan) and Pedram Pakseresht who have been a source of friendship as well as good advice and collaboration. I also thank Joseph Skitka for helping me understand the solver code in my early days at CFPL. Many thanks to all my friends from OSU: Tracie Jackson, Erfan Rasouli, Reza Ziazi, Firas Siala, Alex Totpal, Cathy Huan Wang and Bo Liu.

I must also thank all my friends with whom I started my journey of learning CFD: Bipin Pande, Aloke Das, Sheetal Zaroo, Shyam Sundar Tallada, Murugeshbabu Mahadevan, Alay Shah, Ambarish Khot, Bhaskar Guptha, Ravindra Sarade, Suryabhaskar Reddy, Ravi Kumar Vesam, Abhinit Kishore, Sameer Kumar, Siddharth Pantvaidya, Senthilkumaran Murugesan and finally, Nityanand Sinha who is my go-to person for any technical questions. Memories of our hard work and good times we spent in Moscow will always be close to my heart.

I am eternally grateful to my friend Vinayak Jangam for allowing me to stay at his house and driving me to work during my month long visit to Stanford University for the summer program. I am also thankful to Karthikeyan Devendran who was always a phone call away and assisted me in every possible way. Special thanks to Stimit Shah; technical discussions on the topic of turbulence with him have been highly beneficial.

I cannot forget my friends from Georgia Tech who helped me through hard times, cheered me on, and celebrated each accomplishment: Rajiv Shenoy, Prashant Khare, Sayan Ghosh and Faisal Ahmed. Many thanks for the good times and everything that you have done to make this journey enjoyable.

I am deeply thankful to my family, back in India, who initially thought that I would be gone to the United States for only a couple of years, but soon realized that it would take a bit longer. I owe a lot to my parents, Anjali Ghodke and Deepak

Ghodke, who encouraged and helped me a lot at every stage of my academic life and longed to see this dream of mine come true. I am forever indebted to their love, support and sacrifices. Words cannot express my appreciation and love for my loving younger sister Chaitrali Ghodke. I am grateful to her for always being there for me as a friend and expressing confidence in my abilities. I will always cherish memories of good times we spent together, in particular, all our road trips and frequent visits to Portland.

I would like to express my gratitude to my parents-in-law Anita Gupte and Sanjay Gupte for their unfailing emotional support. Their endless patience and encouragement in my PhD endeavor from beginning to end is highly appreciable. In particular, the unconditional trust shown by allowing their daughter to marry a fresh graduate student who was uncertain of his future 7 years back. Special thanks must go to my brother-in-law Sumeet Gupte for supporting me throughout this journey.

Last, but not the least, I would like to acknowledge the most important person in my life, my wife Amruta, whom I have known for last 16 years. She has been a constant source of strength and inspiration. There were times of failures, frustration, hopelessness, and it was only her love, patience, determination and constant encouragement that ultimately made it possible for me to achieve something in life. She has been extremely supportive of me throughout this journey and has made countless sacrifices to help me get to this point. After all, it takes a lot to turn an amateur boyfriend with marginal intelligence into a husband with doctorate degree. There is no way to express how much it means to me to have a partner like you. Thank you for being my best friend. I owe you everything. *"Yo Amu, we did it!"*

CONTRIBUTION OF AUTHORS

Dr. Sourabh V. Apte contributed to the development of the numerical methods used in Chapters 2, 3, and 4, as well as to the interpretation of the results throughout this dissertation.

TABLE OF CONTENTS

TABLE OF CONTENTS (Continued)

Page

LIST OF FIGURES

LIST OF FIGURES (Continued)

Figure | Page

LIST OF FIGURES (Continued)

Figure Page

LIST OF TABLES

LIST OF TABLES (Continued)

Table | Page

LIST OF APPENDIX FIGURES

LIST OF APPENDIX FIGURES (Continued)

Figure Page

LIST OF APPENDIX TABLES

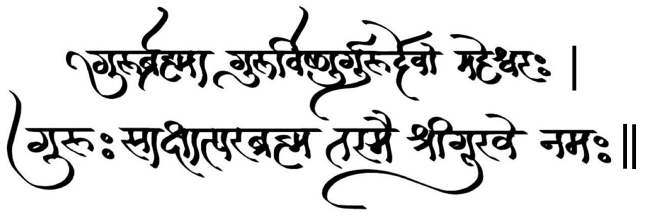

Dedicated to my Guru Shri Brahmachaitanya Gondavalekar Maharaj

RELATED PUBLICATIONS

The content of this thesis is based in parts on the following references, published in the course of this study. The contributions of the co-authors is highly acknowledged.

- **Ghodke, C. D.**, and Apte, S. V.,"**DNS study of particle-bed–turbulence interactions in an oscillatory wall-bounded flow**", *Journal of Fluid Mechanics, Vol. 792, 2016.* doi:10.1017/jfm.2016.85
- **Ghodke, C. D.**, and Apte, S. V.,"**Spatio-Temporal correlations of hydrodynamic forces on particles in an oscillatory wall-bounded flow environment**", to appear in *Proceedings of the ASME Fluids Engineering Summer Meeting, August 2016, USA*
- **Ghodke, C. D.**, and Apte, S. V.,"**A numerical investigation of particle-bed–turbulence interactions in oscillatory flows**", to appear in *Proceedings of ICMF 9th International Conference on Multiphase Flow, May 2016, Italy*
- **Ghodke, C. D.**, Skitka, J., and Apte, S. V.,"**Characterization of oscillatory boundary layer over a closely packed bed of sediment particles**", *Special Issue (invited) on Journal of Computational Multiphase Flows, Vol. 6, No. 4, November, 2014.* doi: 10.1260/1757-482X.6.4.447
- **Ghodke, C. D.**, Apte, S. V., and Urzay, J.,"**Direct numerical simulations of oscillatory wall-bounded flow over a closely-packed fixed bed of spherical particles**", *Center for Turbulence Research, Proceedings of the Summer Program 2014*
- **Ghodke, C. D.**, and Apte, S. V.,"**DNS of oscillatory boundary layer over a closely packed layer of sediment particles**", *Proceedings of the ASME Fluids Engineering Summer Meeting, August 2014*

DNS study of Particle-bed–Turbulence Interactions in Oscillatory Flows

Chapter 1: Introduction

A river or sea bed is made up of sediment particles that are in close contact with each other and retain the form of the bed through collision and cohesive forces (Fredsøe & Deigaard, 1992). Shear stresses exceeding a critical threshold can strip the particles from the bed, suspend them in the fluid and deposit them elsewhere (Drake *et al.*, 1988). Prediction of onset of sediment erosion and interactions of sediment bed with oscillatory turbulent flows are the two long-standing issues governing sediment transport in coastal environments.

Computations of sediment-laden flows typically employ simplistic quasi-steady models to study sediment transport, in particular, onset of sediment erosion (Bagnold, 1966; Fredsøe & Deigaard, 1992; Nelson *et al.*, 2000; Nino *et al.*, 2003). Historically, these models are based on (i) Shields parameter, $\theta = \bar{\tau}_w/(\rho_p - \rho)gD$ (Shields, 1936), which is the ratio of average bed shear stress ($\bar{\tau}_w$) to the stabilizing settling force due to gravitational acceleration (g). Here, ρ_p and ρ are sediment and fluid densities, respectively and D is the average particle size. The mean bed-load particle flux is then obtained as a function of particle size and bed shear stress; (ii) Sleaths parameter, $S = (-dp/dx)/(\rho_p - \rho)g$ (Sleath, 1995; Flores & Sleath, 1998; Sleath, 1999), incorporates pressure-gradient at the peak of the cycle and is used in wave-induced sediment transport models. Laboratory observations have tried to quantify onset of erosion based on exceeding the Shields or Sleaths parameters beyond a critical value. However, these models are deterministically based on mean values of the destabilizing forces, and do not consider effects of particle shape, bed arrangements, and more importantly, multi-scale interactions between turbulent

flow and sediment particles. More accurate descriptions can be developed using stochastic models by measuring or directly computing the probability of particle entrainment based on stochastic flow properties (Einstein, 1950; Mingmin & Qiwei, 1982; Cheng & Chiew, 1998; Papanicolaou *et al.*, 2002; Cheng & Law, 2003; Wu & Chou, 2003; Wu & Kuo-Hsin, 2004; Hofland & Battjes, 2006). Knowing the probability distributions of lift and drag forces on the particles under which particle dislodgement can take place is critical in developing such stochastic models. In many instances, as computations or measurements of drag and lift forces are not straightforward, these models often assume Gaussian or log-normal distribution for near-bed velocity fluctuations to correlate instantaneous hydrodynamic forces on particles to the near-bed flow.

Research hypothesis and objectives: The proposed research builds upon the following main hypothesis: the dynamics of near-wall turbulence structure and resultant variations in the magnitudes and time-scales of the destabilizing drag and lift forces on sediment grains are critical in formulating predictive criteria for onset of erosion. The numerical experiments are therefore designed to resolve this central hypothesis.

The main objectives of the proposed work is to conduct high-fidelity particle-resolved direct numerical simulations for a range of Reynolds numbers to obtain detailed data on coherent structures, Reynolds stresses, turbulent kinetic energy budget, and correlate wall-layer dynamics to the drag and lift forces on the particle-bed in an oscillatory turbulent flow. Investigation of the stochastic nature of particle forces by quantifying their higher-order statistics will also be carried out. To ascertain confidence in the simulations, results of the present analyses are compared against the data in the literature whenever possible.

Intellectual merit: The novelty of this research is in the development and use of a fully-resolved simulation approach based on first principles, without requiring models for drag and lift forces, to study particle-bed–turbulence interactions in oscillatory flows. This work will, for the first time, provide data on the temporal variations in the magnitude of drag and lift forces on the bed of fixed sediment

grains, the time-scales associated with these variations, and their correlations with near-bed turbulence in oscillatory flow environment. Any such measurements are extremely difficult to obtain from experiments and novel numerical methodologies are therefore necessary to provide detailed flow characteristics.

Outline of the thesis: The thesis is structured as follows. Chapter 2 presents DNS results of oscillatory flow field over a rough-bed of closely packed fixed spherical particles for a range of Reynolds numbers in transitional and rough turbulent regime. Characterization of near-bed turbulence in terms of mean velocity distribution, Reynolds stress variation, turbulent kinetic energy budget, near-bed flow structures and their anisotropy along with probability distribution functions of velocity and pressure perturbations are reported. In chapter 3, statistical descriptions of hydrodynamic forces are reported. The spatial and temporal structure of unsteady drag and lift forces on the particle-bed are investigated. Focus is given on characterizing unsteady forces in terms of spatial distribution, temporal auto-correlation, force spectrum, higher-order force statistics and intermittency as well as cross-correlations with measurable flow variables. In chapter 4, flow dynamics inside the roughness sublayer has been studied in detail by employing a double-averaging technique. In order to characterize modulation of the near-bed turbulence as it governs the nature of inner–outer layer interactions along with generation of drag on the roughness elements, the focus is given analyzing alternate pathways of kinetic energy transport mechanisms resulting from spatial inhomogeneities at the roughness scale. Finally, concluding remarks are given in chapter 5. Some additional supporting material is provided in the appendices.

Chapter 2: DNS study of particle-bed–turbulence interactions in an oscillatory wall-bounded flow

Chaitanya D. Ghodke and Sourabh V. Apte

Journal of Fluid Mechanics,
Vol. 792, pp 232-251, 2016
Cambridge University Press
doi:10.1017/jfm.2016.85

Abstract

Particle-resolved direct numerical simulations (DNS) are performed to investigate the behavior of an oscillatory flow field over a rough-bed, corresponding to the experimental setup of Keiller & Sleath (1976) for transitional and turbulent flows over a range of Reynolds numbers (95–400) based on the Stokes-layer thickness. It is shown that the roughness modulates the near-bed turbulence, produces streamwise horse-shoe structures which then undergo distortion and breaking, and therefore reduces the large-scale anisotropy. A fully developed equilibrium turbulence is observed in the central part of the oscillation cycle, with two-component turbulence in the near-bed region and cigar-shaped turbulence in the outer region. A double-averaging of the flow field reveals spatial inhomogeneities at the roughness scale and alternate paths of energy transport in the turbulent kinetic energy (TKE) budget. Contrary to the unidirectional, steady flow over rough beds, bed-induced production terms are important and comparable to the shear production term. It is shown that the near-bed velocity and pressure fluctuations are non-Gaussian, a result of critical importance for modeling of incipient motion of sediment grains.

2.1 Introduction

Turbulent flows over rough surfaces have been a subject of rigorous investigation owing to their increasing technological interests in engineering and geophysical applications (Raupach & Thom, 1981; Raupach *et al.*, 1991; Jiménez, 2004). There has been considerable work done on stationary, unidirectional turbulent flows over rough surfaces clearly identifying the effects of roughness elements on near-bed turbulence as increased bed shear stress, reduction in near-bed anisotropy, and marked changes in turbulent energy transport mechanisms (Krogstad *et al.*, 1992; Krogstad & Antonia, 1994; Krogstad *et al.*, 2005; Ikeda & Durbin, 2007; Chan-Braun & Uhlmann, 2011; Yuan & Piomelli, 2014*b*; Kempe *et al.*, 2014). Presence of roughness was also shown to greatly influence near-bed sweep and ejection motions

(Krogstad *et al.*, 1992, 2005). In many practical applications, such as, sediment transport in coastal flows, blood flow circulation, intake of a combustion chamber and so on, the flow conditions are mainly unsteady/non-stationary in nature. However, such detailed findings pertaining to turbulence modulation by rough-bed under oscillatory flow conditions have not been well documented. In order to improve the understanding of the mechanisms that lead to the onset of sediment erosion under coastal conditions, detailed knowledge of sediment-bed-turbulence interactions is necessary. Impact of near-bed sweep/ejection events on the onset of sediment motion can be significant and should be accounted for in the development of probabilistic models predicting sediment erosion. These models often assume Gaussian or log-normal distribution for near-bed velocity fluctuations (Einstein, 1950; Papanicolaou *et al.*, 2002). It is hypothesized that the near-bed flow dynamics, roughness effects, and flow through porous regions lead to non-Gaussian velocity fluctuations, and higher-order turbulence statistics, such as kurtosis and skewness, are necessary for better predictions (Wu & Kuo-Hsin, 2004).

Present understanding of oscillatory boundary layer over rough surfaces is mainly based on experimental investigations of Keiller & Sleath (1976); Jonsson & Carlsen (1976); Sleath (1987); Jensen *et al.* (1989), including more recent studies of Chen *et al.* (2007); Dixen *et al.* (2008); Mujal-Colilles *et al.* (2014); Corvaro *et al.* (2014). Keiller & Sleath (1976) first reported velocity measurements close to the rough-bed sinusoidally oscillating in its own plane. Jonsson & Carlsen (1976) later reported velocity measurements, but not turbulence, for fully turbulent oscillatory flow over a rough-bed. However, most detailed experimental studies of sinusoidally oscillating flow over rough beds are those of Sleath (1987) and Jensen *et al.* (1989). Sleath (1987) presented the measurements for velocity and near-bed turbulent intensities for moderately high Reynolds numbers, whereas Jensen *et al.* (1989) further expanded the research by carrying out experiments at higher Reynolds numbers and wider range of particle diameters. In essence, all these studies reported a common conclusion that the presence of roughness elements significantly affects near-bed turbulence by increasing turbulent intensities and

Reynolds stresses. Beyond this, however, due to experimental limitations these studies did not present detailed analysis of near-bed turbulence structure. On the other hand, owing to the enormous computational cost in resolving individual roughness elements and complexities in handling flow unsteadiness, performing detailed numerical investigations of these flows at high Reynolds numbers is still a challenge and very few numerical investigations have been reported so far (Fornarelli & Vittori, 2009; Ding & Zhang, 2010). However, none of these studies presented detailed characterization of near-bed turbulent flow dynamics.

This paper is therefore oriented towards fundamental understanding of roughness-turbulence interactions in symmetric, sinusoidally oscillating turbulent flow over a range of Reynolds numbers. To the best of our knowledge, no such detailed characterization of near-bed turbulence in oscillatory flows over rough surfaces by means of DNS has been reported to date. The outline of the paper is as follows: the computational setup and methodology are presented in § 2. In § 3, simulation results are presented; followed by main conclusions in § 4.

2.2 Methodology

2.2.1 *Computational setup and simulation parameters*

The computational domain, shown in Fig. 3.1, consists of a doubly periodic box (in x and y directions) with a smooth no-slip wall at $z = 0$ and a slip wall at $z = 30\delta$, where $\delta = \sqrt{2\nu/\omega}$ is the Stokes-layer thickness, ν is the kinematic viscosity, $\omega = 2\pi/T$ is the oscillation frequency and T is the period of the wave. Rough-bed made up of hexagonal pack of fixed spherical roughness elements is considered corresponding to the experimental configuration of Keiller & Sleath (1976). As shown in Fig. 3.1, x, y and z are, respectively, the streamwise, spanwise and wall-normal directions and u, v and w are the velocity components in those directions. The in-plane domain length is 24.1δ and 13.9δ in the streamwise and spanwise directions, respectively. The roughness element diameter normalized with the Stokes-layer thickness is, $D = d/\delta = 6.95$, equivalent to the gravel-type roughness (Sleath,

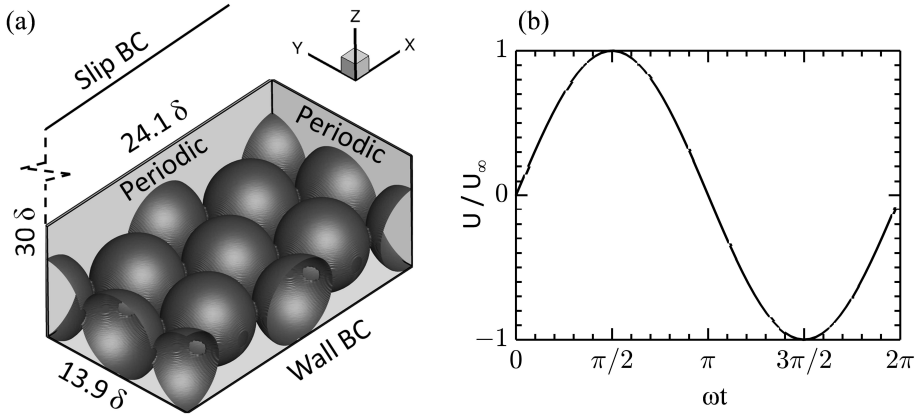

Figure 2.1: (a) Close-up view of the computational domain and boundary conditions. (b) A harmonic pressure forcing is imposed that results in a streamwise velocity component $U_\infty \sin(\omega t)$ far from the bed.

1987).

The dimensionless parameters of the problem to completely characterize the flow are outlined in Table 4.1, consist of the Reynolds number based on Stokes-layer thickness, $\mathrm{Re}_\delta = U_\infty \delta/\nu$, and the effective roughness Reynolds number, $k_s^+ = u_{\tau,max} k_s/\nu$. Here, U_∞ is the amplitude of the free-stream velocity, k_s is the Nikuradse roughness size and $u_{\tau,max}$ is the maximum friction velocity in a flow cycle. The corresponding particle Reynolds number, $\mathrm{Re}_D = U_\infty D/\nu$ and Reynolds number based on the wave amplitude, $\mathrm{Re}_a = U_\infty a/\nu$ are also given in Table 4.1. Here, a is the amplitude of wave oscillation given by, $a = U_\infty/\omega$. Figure 2.2 maps the different cases on a regime diagram ($a/k_s - Re_a$ map) for oscillatory flow over roughness elements showing the laminar, transitional, and rough turbulent regimes. The cases studied in this work span a broad range of Reynolds numbers, starting from transitional, where incipient vortex formation around the spheres leads to strong vertical velocities at $\mathrm{Re}_a = 4510$, up to fully turbulent, very rough regime, $\mathrm{Re}_a = 80000$.

Table 4.1 tabulates the parameters and spatial resolutions used in this study.

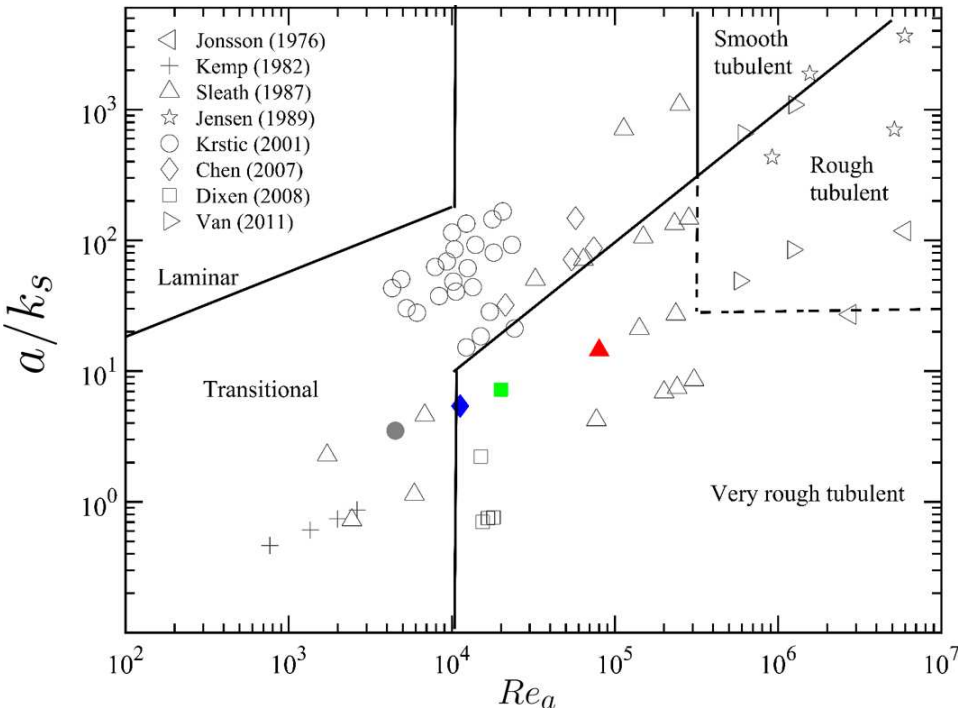

Figure 2.2: Delineation of different flow regimes for oscillatory flow illustrating previous studies (Jonsson & Carlsen, 1976; Kemp & Simons, 1982; Sleath, 1987; Jensen *et al.*, 1989; Krstic & Fernando, 2001; Chen *et al.*, 2007; Dixen *et al.*, 2008; van der A *et al.*, 2011) and present cases. Symbols represent: ●, $\mathrm{Re}_\delta = 95$; ♦, $\mathrm{Re}_\delta = 150$; ■, $\mathrm{Re}_\delta = 200$; ▲, $\mathrm{Re}_\delta = 400$.

Re_δ	Re_a	Re_D	k_s^+	Nx	Ny	Nz	Nz/D	a/k_s	Regime
95	4510	660	315	120	80	460	160	3.4	transitional
150	11250	1042	400	136	100	556	200	5.4	very rough turbulent
200	20000	1390	478	184	120	664	240	7.2	very rough turbulent
400	80000	2780	745	208	152	832	300	14.4	very rough turbulent

Table 2.1: Computational parameters and grid resolution details. k_s^+ is computed using maximum value of the friction velocity in a flow cycle. Present study assumes low Froude numbers.

Uniform grids, although not cubic, are used in the region surrounding the roughness bed (giving roughly around 160 to 300 points in the wall-normal direction per particle diameter) and grids are stretched in the wall-normal direction (above z = 10δ) using a hyperbolic tangent function. In all the cases, Δx^+ and Δy^+ are less than 5 and 3, respectively, and $\Delta z^+ < 1$ in the near-bed region (up to z = 10δ). Around 15 flow cycles per case are computed to obtain statistical convergence.

A systematic grid refinement study was performed to obtain optimum grid spacing, confirming a nearly second-order accuracy of the solver as shown in Ghodke *et al.* (2014*b*). Present grid resolution was chosen as the there were no discernible differences in the flow statistics of finest and current grid (see Appendix A). In addition, energy spectra were analyzed for different grid resolutions keeping the Courant number (CFL) close to 0.5 for time-accurate calculations. The streamwise and spanwise energy spectra (not shown) illustrated the adequacy of the computational grid to resolve the smallest scales of turbulence. The domain size is verified to be sufficiently large by calculating two-point spatial velocity correlation functions, in both streamwise and spanwise directions, by doubling the domain. The correlations showed no effect of domain size, and confirm the adequacy of the domain size to accommodate the largest turbulent structures (see Appendix B). Vertical size of the domain is chosen such that all turbulent statistics decay to

zero at almost half the vertical height. Increasing the vertical extent of the domain showed no effects on the near-bed flow statistics (see Appendix A). Similar computational domain sizes were used in the previous work by Fornarelli & Vittori (2009); Ding & Zhang (2010).

2.2.2 *Validation study*

The numerical solver used in this work is based on a co-located grid, fractional time-stepping, finite volume algorithm based on energy conserving principles and has been developed and validated thoroughly for a range of canonical and complex turbulent flows (Mahesh *et al.*, 2006; Moin & Apte, 2006; Apte *et al.*, 2003, 2009*a*,*b*). This solver was further extended to incorporate fictitious domain method to handle arbitrary shaped immersed objects without requiring the need for body-fitted grids (Apte *et al.*, 2008; Apte & Finn, 2013). The fictitious domain approach facilitates solution of freely moving particles for a wide range of fluid-particle density ratios, although the particles are held fixed in the present study. The solver is fully validated for a range of test cases including flow over a cylinder and sphere for different Reynolds numbers, flow over touching spheres at different orientations, flow developed by an oscillating cylinder, laminar and turbulent flow through porous media, among others. The details of the algorithm as well as very detailed verification and validation studies have been published elsewhere (Apte *et al.*, 2008; Apte & Finn, 2013). In addition, the solver was also used to perform direct one-to-one comparison with a body-fitted solver with known second-order accuracy for steady inertial, unsteady inertial, and turbulent flow through porous media (Finn & Apte, 2013). The details of this comparison focused on issues such as grid resolution needed near the wall, issues related to touching spheres and contact points, quality of solution compared to the body-fitted solver, comparison with experimental work of Suekane *et al.* (2003) on flow through a packed array of half spheres, and establishing the grid resolution requirement per particle diameter for predicting the unsteady flow-field in packed porous beds within 5% uncertainty based on the grid convergence index (GCI). Turbulent flow at pore Reynolds number of 600 was also

computed in the same configuration and compared with the body-fitted approach to obtain good predictive capability of the present fictitious domain solver. This same solver was also used to study turbulent flow in a randomly packed bed of 51 spheres capturing complex porescale flow features in agreement with published data.

In addition, in order to verify and validate the solver for the specific case under investigation, oscillatory flow over a particle-bed corresponding to $\mathrm{Re}_\delta = 95$ case is validated against experimental data of Keiller & Sleath (1976). Figure 2.3 shows variation of (a) normalized peak fluid-frame resultant velocity magnitude U_R, and (b) phase at which this peak velocity is recorded, plotted at various heights above the roughness crest for $\mathrm{Re}_\delta = 95$. Data from the experimental work of Keiller & Sleath (1976) along with recent simulations of Fornarelli & Vittori (2009); Ding & Zhang (2010) are also plotted. Existing literature pertaining to this topic frequently uses an alternative frame of reference, consistent with that of the classic experiments conducted by Keiller & Sleath (1976), which features an oscillating particle-bed in a fixed fluid-frame. Figure 2.3 is presented in the fluid-frame to be consistent with this convention. As seen in Fig. 2.3, current simulations data are generally in a better agreement with the experimental work of Keiller & Sleath (1976), suggesting the present choice of parameters is able to provide accurate descriptions of the oscillatory flow phenomena. Note that, the vertical trends in both the plots starting at around $(z - z_c)/\delta = 0.5$ are artifacts of the near-bed incipient ejection motions resulting in strong vertical velocity and are well captured in the current simulations. Additional comments are provided in Appendix C.

2.3 Results and discussion

Majority of the results presented below are for $\mathrm{Re}_\delta = 400$, which is in the fully turbulent, very rough regime. Similar trends are observed for other turbulent flow conditions $\mathrm{Re}_\delta = 150$ and 200. Following Mignot *et al.* (2009), a double averaging procedure is employed for the analysis described below that decomposes

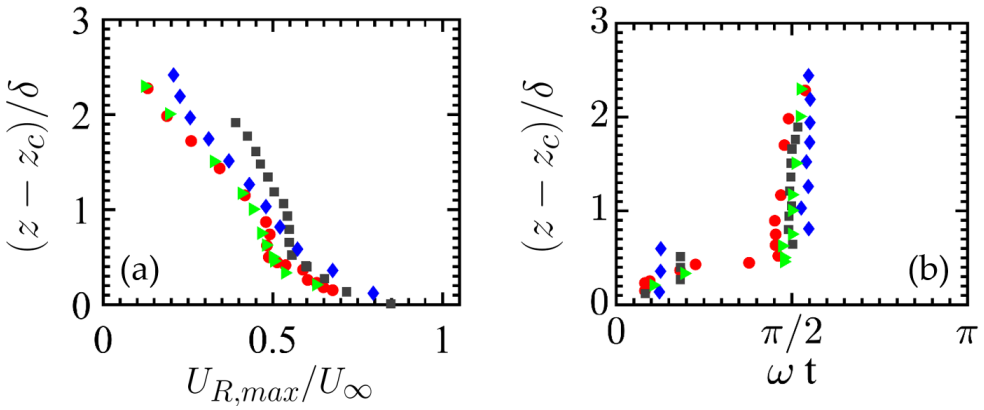

Figure 2.3: For $\mathrm{Re}_\delta = 95$, variation of (a) normalized peak fluid-frame resultant velocity magnitude U_R, and (b) phase at which the peak velocity is recorded, plotted at various heights above the roughness crest location z_c normalized by the Stokes-layer thickness δ. U_R is the resultant velocity magnitude of streamwise and vertical velocity components. Symbols represent: ●, (Keiller & Sleath, 1976); ♦, (Ding & Zhang, 2010); ■, (Fornarelli & Vittori, 2009); ▲, present data.

a flow quantity, ϕ into double average $\langle\overline{\phi}\rangle$ (where, overbar and brackets respectively denote phase and homogeneous spatial averages), the spatial disturbance of the phase-average $\widetilde{\phi}$ and the turbulent fluctuation ϕ',

$$\phi(x, y, z, \omega t) = \langle\overline{\phi}\rangle(z, \omega t) + \widetilde{\phi}(x, y, z, \omega t) + \phi'(x, y, z, \omega t) \tag{2.1}$$

2.3.1 *The mean flow field and Reynolds stresses*

Figure 2.4 shows profiles of double-averaged streamwise velocity in wall units, $u^+ = \langle\overline{u}\rangle/u_\tau$, plotted against $A(z - z_b)/k_s$ in a semi-log plot; where z_b is the zero-displacement plane (Dixen *et al.*, 2008). The logarithmic law for flow over a rough-bed can be written as,

$$\langle\overline{u}(z, \omega t)\rangle = \frac{u_\tau}{\kappa} \ln\left(\frac{A(z - z_b)}{k_s}\right), \tag{2.2}$$

with the von Karman constant $\kappa = 0.41$ and $A = 30$ as given by (Raupach & Thom, 1981). As discussed in Dixen *et al.* (2008), the zero-displacement plane z_b and Nikuradse's equivalent roughness k_s were determined by fitting the double-averaged velocity profile to the log-law given by Eq. 2.2. The values of $z_b = 0.7D$ and $k_s = 2d$, are in a good agreement with the literature (Sleath, 1987; Jensen *et al.*, 1989; Dixen *et al.*, 2008). As seen in Fig. 2.4, significant portion of the velocity curve that follows the log-law given by Eq. 2.2 is present from early-acceleration until mid-deceleration phases, i.e. from $2\pi/10$ until $7\pi/10$. This is due to the fact that late deceleration phases are characterized by absence of near-bed turbulence production as discussed later; during this period new laminar boundary layer starts to develop in the reverse direction, and continues to grow until early acceleration phases after which local friction velocity is large enough to trigger the turbulence. For $\omega t = 8\pi/10$, velocity close to the bed is therefore negative due to the near-bed flow reversal. Also, it is interesting to note that some portion of the velocity curve at this phase seem to follow log-law, although with the larger value of the slope, resulting in the departure from universal value of von Karman constant $\kappa = 0.41$.

Double averaged profiles of the Reynolds stresses and TKE normalized by U_∞^2 are plotted in Fig. 2.5. From early-acceleration until late-deceleration phases ($\omega t = 2\pi/10$ up to $8\pi/10$), presence of near-bed turbulence is evident as seen in Fig. 2.5. Reynolds stresses and TKE increase away from the effective bed location $(z - z_b)/D = 0$ and peak close to the roughness crest level $(z - z_b)/D = 0.3$, and decay to zero further in the outer region above $(z - z_b)/D > 1$. The streamwise component of the Reynolds stress $\langle\overline{u'^2}\rangle$ contributes most to the TKE and peaks at the roughness crest location. On the other hand, as a consequence of the near-bed turbulent motions, Reynolds shear stress $\langle\overline{u'w'}\rangle$ peaks slightly above the crest level.

To validate the numerical predictions and to further verify adequacy of the computational domain, grid resolution and rigid body treatment, boundary layer thickness, δ', and maximum friction factor, $f_{w,max} = 2\left(u_{\tau,max}/U_\infty\right)^2$, were calculated. Here, boundary layer thickness δ' is defined as the elevation of maximum

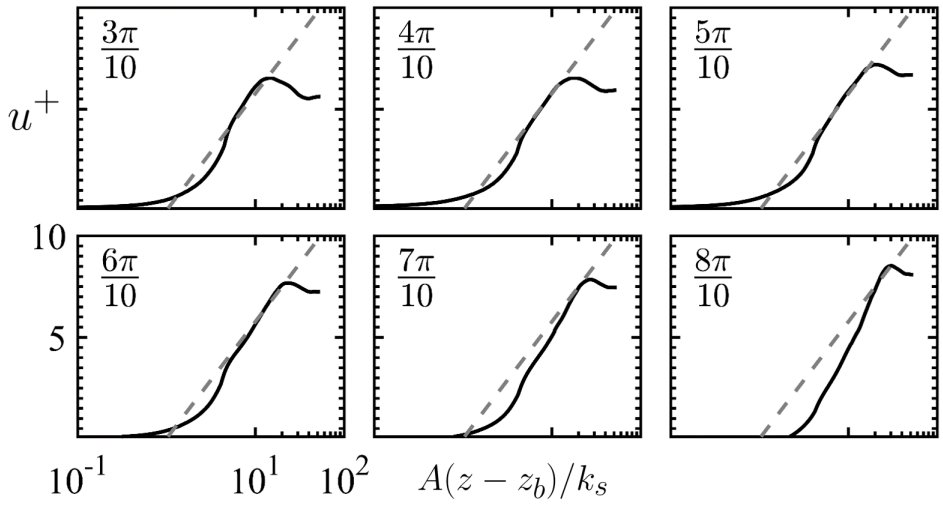

Figure 2.4: Phase evolution of double-averaged streamwise velocity profile normalized by u_τ for $\mathrm{Re}_\delta = 400$. The dash line represents the log-law.

overshoot in the streamwise velocity at a peak phase (Jensen *et al.*, 1989) measured from z_b. Following Yuan & Piomelli (2014*a*), the friction velocity u_τ is given as,

$$u_\tau^2 = -\overline{F_t}/\rho A \tag{2.3}$$

where, A is the horizontal area and F_t is the total streamwise drag acting on the roughness elements along with that on the smooth-wall and is computed explicitly in the solver by integrating viscous and pressure forces in the flow direction. Alternatively, u_τ can also be computed by fitting the mean velocity profile to the log-law as briefly described in Dixen *et al.* (2008); the latter yielding approximately same values as those obtained by the former method for the flow under consideration. Figure 2.6 shows phase variation of the friction velocity for range of Reynolds numbers in terms of dimensionless friction factor defined as, $f_w = 2\left(u_\tau/U_\infty\right)^2$. Consistent with Jensen *et al.* (1989), the evolution of friction factor and free-stream velocity are not in phase. However, as a result of increased momentum transfer due to turbulence, this phase delay decreases with the increase

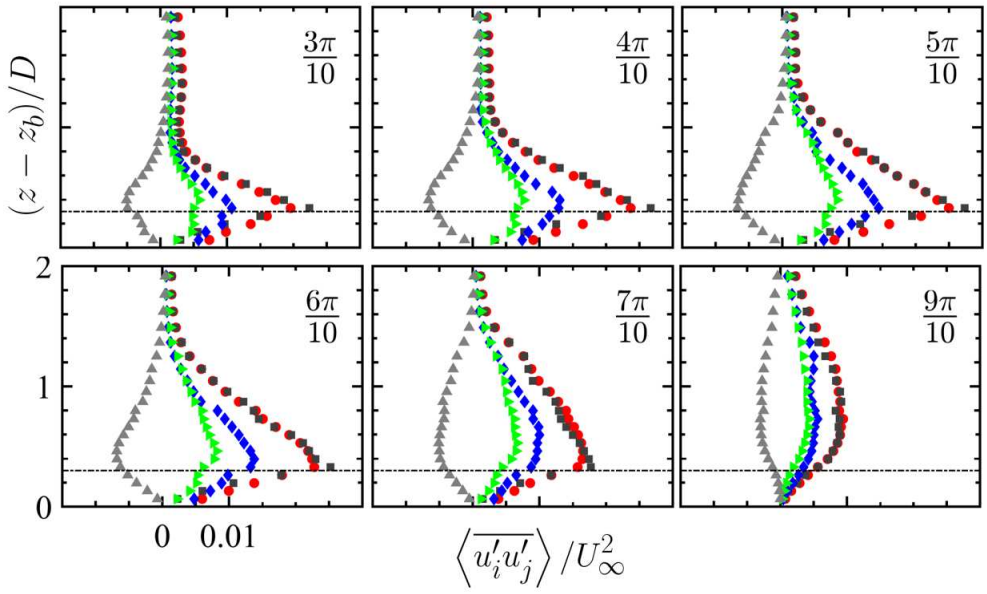

Figure 2.5: Phase evolution of double-averaged Reynolds stress and TKE for $\mathrm{Re}_\delta = 400$. Symbols represent: ●, TKE; ■, streamwise Reynolds stress $\langle \overline{u'^2} \rangle$; ◆, spanwise Reynolds stress $\langle \overline{v'^2} \rangle$; ▶, wall-normal Reynolds stress $\langle \overline{w'^2} \rangle$; ▲, Reynolds shear stress $\langle \overline{u'w'} \rangle$. The dash-dot line at $(z - z_b)/D = 0.3$ shows roughness crest level.

in Reynolds number.

Figure 2.7 (a) and (b), respectively, show variation of the normalized boundary layer thickness, δ'/k_s, and maximum friction factor, $f_{w,max}$ with the roughness parameter a/k_s for various Reynolds numbers. The present predictions show very good match against the experimental data (Jonsson & Carlsen, 1976; Sleath, 1987; Jensen *et al.*, 1989; Dixen *et al.*, 2008). With increase in Reynolds number, roughness parameter a/k_s also increases, resulting in turbulent and rough bed conditions. Period-averaged turbulence intensities for various values of a/k_s corresponding to different values of Reynolds numbers are also plotted in Fig. 2.7(c),(d) and compared with Sleath (1987). The numerical data tends to collapse onto a unique curve with increase in Reynolds number, confirming Sleath's observation. It can also be seen that, increase in a/k_s results in decrease in streamwise intensity, $\sqrt{\overline{u'^2}}$, and increase in the wall-normal intensity, $\sqrt{\overline{w'^2}}$. If compared with fully turbulent, smooth wall case from Jensen *et al.* (1989) (test no. 10 for $\mathrm{Re}_\delta \approx 3300$, not shown here), it is observed that for the present rough-bed cases, the ratio of wall-normal and spanwise turbulent intensities to streamwise component is higher than that in the smooth-wall case of Jensen *et al.* (1989). These results indicate the tendency of the roughness elements to redistribute the energy from streamwise to spanwise and wall-normal components, more so at the peak phase and therefore, decrease the overall large-scale near-bed anisotropy as also observed by Sleath (1987) in oscillatory flows.

2.3.2 *Turbulent kinetic energy budget*

TKE budget is studied to analyze the role and relative importance of different terms involved in energy transport mechanisms. Following Mignot *et al.* (2009), double-averaged TKE budget equation for flow over roughness with streamwise-

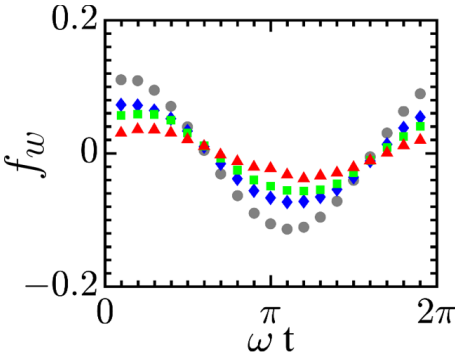

Figure 2.6: Phase variation of the friction factor f_w. Symbols represent: ●, $\mathrm{Re}_\delta = 95$; ♦, $\mathrm{Re}_\delta = 150$; ■, $\mathrm{Re}_\delta = 200$; ▲, $\mathrm{Re}_\delta = 400$.

spanwise homogeneity is given as,

$$\frac{\partial \langle \overline{u_i' u_i'} \rangle / 2}{\partial t} = \underbrace{-\langle \overline{u_i' w'} \rangle \frac{\partial \langle \overline{u_i} \rangle}{\partial z}}_{P_s} + \left[\underbrace{-\left\langle \widetilde{u_i' u_j'} \frac{\partial \widetilde{u}_i}{\partial x_j} \right\rangle}_{P_w} \underbrace{-\langle \overline{u_i' u_j'} \rangle \left\langle \frac{\partial \widetilde{u}_i}{\partial x_j} \right\rangle}_{P_m} \right]$$
$$- \frac{\partial}{\partial z} \left[\underbrace{\langle \overline{u_i' u_i' w'} \rangle / 2}_{F_k} + \underbrace{\langle \widetilde{u_i' u_i'} \widetilde{w} \rangle / 2}_{F_w} \right] - \frac{1}{\rho} \frac{\partial}{\partial z} \langle \overline{p' w'} \rangle + \nu \frac{\partial^2}{\partial z^2} \langle \overline{u_i' u_i'} \rangle / 2 - \langle \overline{\epsilon} \rangle \qquad (2.4)$$

where, the eight terms on the right side are, respectively, shear production term, P_s, that represents the work of double-averaged velocity against double-averaged shear; wake production term, P_w, is the work of wake-induced velocity fluctuations against the bed-induced shear; P_m is the work of the bed-induced velocity fluctuations against double-averaged shear; $\partial F_k / \partial z$ is turbulent transport, whereas, $\partial F_w / \partial z$ is the bed-induced turbulent transport followed by the sixth term of pressure transport and the seventh term of viscous transport of TKE. The last term on the right represents viscous dissipation. Note that the terms P_m, P_w and F_w arise as a result of spatial heterogeneity at roughness element length scale. Figure 2.8(a) and (b) respectively, show variation of production/dissipation terms

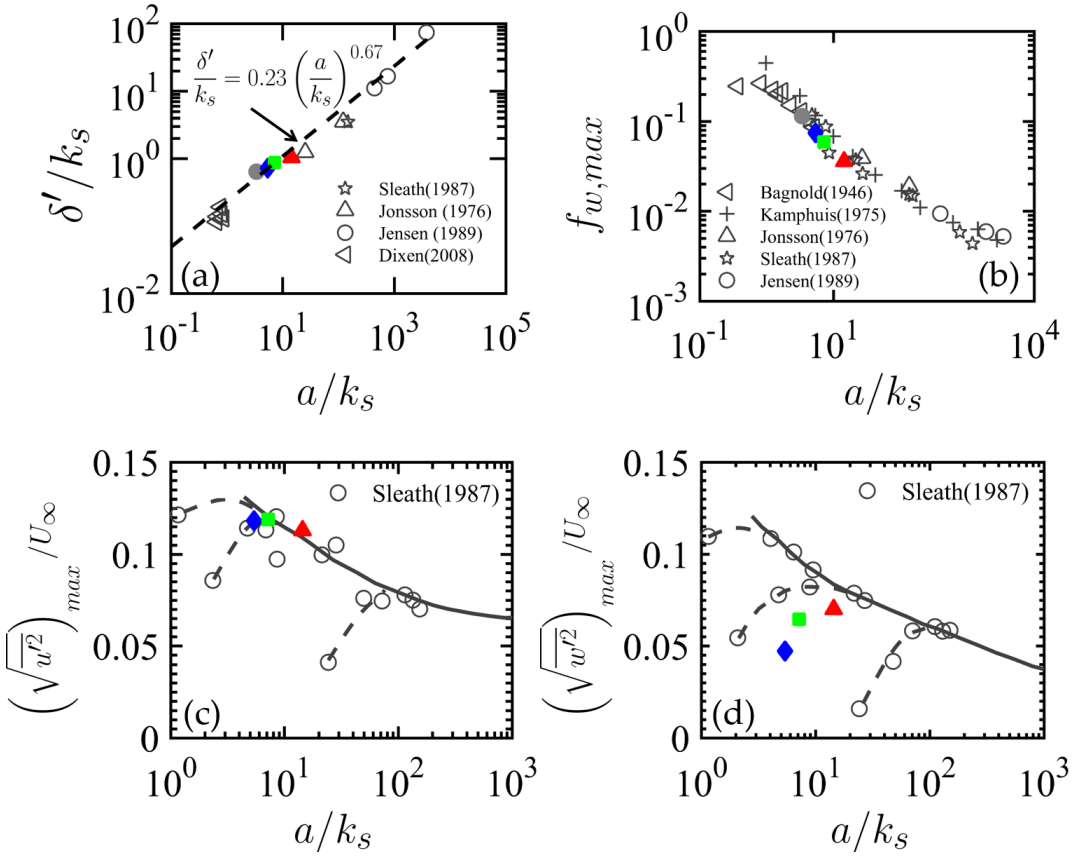

Figure 2.7: Variation with a/k_s of (a) normalized boundary layer thickness δ'/k_s; (b) maximum wave friction factor, given as, $f_{w,max} = 2\,(u_{\tau,max}/U_\infty)^2$; (c) peak period-averaged streamwise and (d) wall-normal turbulence intensity. Symbols represent: ●, $\mathrm{Re}_\delta = 95$; ♦, $\mathrm{Re}_\delta = 150$; ■, $\mathrm{Re}_\delta = 200$; ▲, $\mathrm{Re}_\delta = 400$. The proposed relation (dotted line) between δ'/k_s and a/k_s in (a) is based on Sleath (1987) and is slightly modified to accommodate lower a/k_s values from Dixen *et al.* (2008).

and TKE transport terms.

As seen in Figure 2.8(a), peak in the shear production, P_s, is seen just below the crest of the particle at 0.98D, a result of formation of shear layers near the crest. Dissipation peak is observed slightly below the production peak at 0.96D. The ratio of peak production to dissipation rate in the cycle is around 1.9. Variation of transport terms plotted in Fig. 2.8(b) shows that, the excess energy generated in the vicinity of the crest of the roughness elements is transported away mostly by turbulent diffusion and pressure transport, along with small amount of viscous diffusion. Also, pressure transport is significant mostly below the crest of the particle. These findings are consistent with the existing literature on unidirectional flows (Raupach *et al.*, 1991; Finnigan, 2000; Mignot *et al.*, 2009; Yuan & Piomelli, 2014*b*).

Contrary to the earlier studies of unidirectional flows; however, bed-induced production terms, P_m and P_w, are far from negligible and peak at around same location as P_s. Figure 2.8(c) shows important pathways and energy transfer mechanisms observed in the present work. It is interesting to note that the wake production term, P_w, is negative close to the roughness crest (see II in Fig. 2.8(a)), indicating the conversion of TKE to the wake kinetic energy (WKE) which is given as $\frac{1}{2}\langle\widetilde{u}_i\widetilde{u}_i\rangle$. At this location, streamwise component of the Reynolds stress, $\langle\overline{u'^2}\rangle$, contributes most to the TKE and is typically associated with near-bed turbulent structures of length scales larger than the roughness scale. Work of these large-scale structures against the pressure drag results in effective transfer of energy from TKE to WKE, therefore resulting in negative peak in the production term, P_w. On the other hand, secondary positive peak in P_w is seen just above the effective bed location at $(z - z_b)/D \approx 0.1$ (see I in Fig. 2.8(a)), indicating conversion of WKE to TKE. At this location, all three normal components of Reynolds stress are comparable and are associated with turbulent scales smaller than the roughness size; therefore resulting in conversion of WKE to TKE giving a positive peak in P_w.

Further away from the particle crest, for $(z - z_b)/D > 0.5$, all the terms except

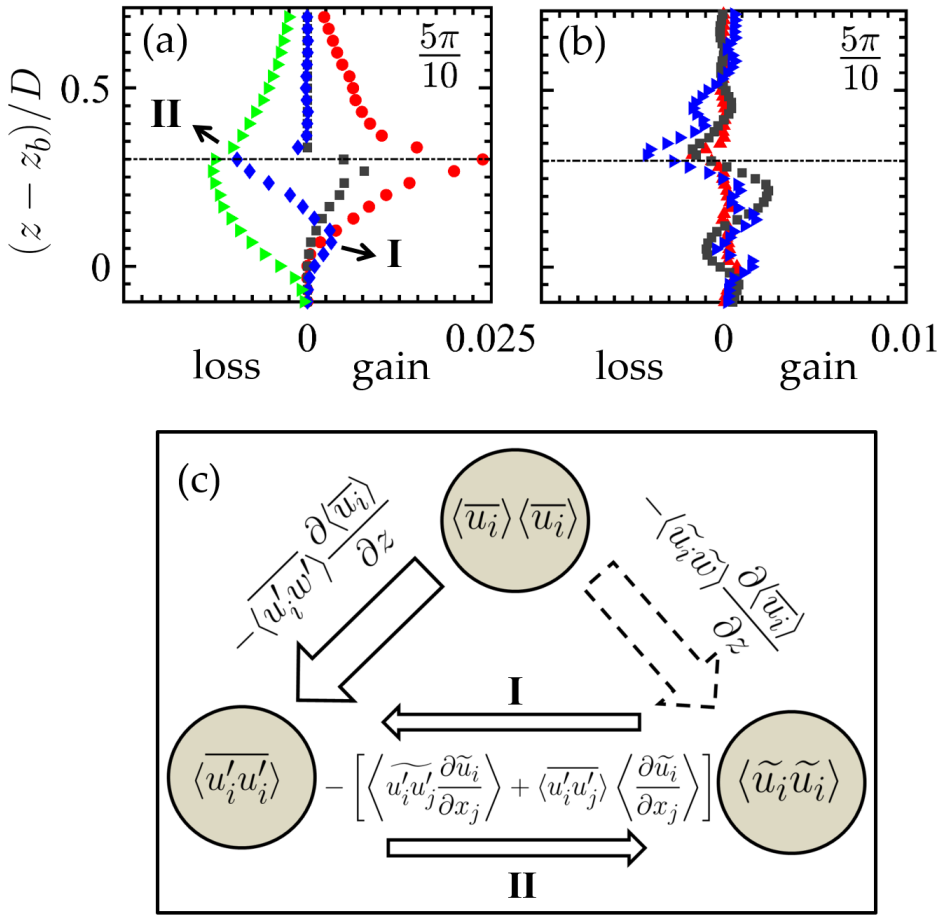

Figure 2.8: For $\mathrm{Re}_\delta = 400$ at peak phase, variation of (a) production and dissipation terms; symbols represent: ●, P_s; ■, P_m; ♦, P_w; ►, viscous dissipation; and (b) transport terms; symbols represent: ►, turbulent transport; ▲, viscous transport; ■, pressure transport. Bed-induced turbulent transport is negligible and is not plotted. The dash-dot line at $(z-z_b)/D = 0.3$ shows roughness crest level. All the terms are normalized by $u^4_{\tau,max}/\nu$; (c) schematic representation of energy transfer mechanisms. Dashed arrow path is not studied in this work.

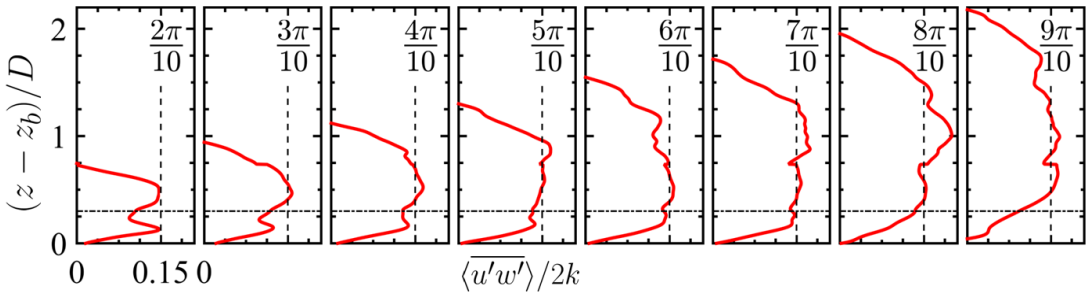

Figure 2.9: Phase evolution of the structure parameter, $a_1 = \langle\overline{u'w'}\rangle/2k$ for $\mathrm{Re}_\delta = 400$. Here, k is the TKE. The dash-dot and dash lines show roughness crest level at $(z - z_b)/D = 0.3$ and the value $a_1 = 0.15$, respectively.

shear production P_s and dissipation $\langle\overline{\epsilon}\rangle$ decay to zero, establishing equilibrium outer layer where the rate of production balances the rate of dissipation. The presence of local equilibrium is also evident from Fig. 2.4 as the flow in this region obeys the logarithmic law. Another measure to effectively quantify the presence of local equilibrium is the Townsend structure parameter, $a_1 = \langle\overline{u'w'}\rangle/2k$ (Townsend, 1961). As shown in Fig. 2.9, it was found that $a_1 \sim 0.15$, similar to the logarithmic layer for steady, unidirectional flows, in most of the fluid column over an entire oscillation cycle, confirming the presence of equilibrium turbulence and validating the approximate self-similarity in the log-law region for oscillatory flows over rough-bed.

2.3.3 *Near-bed turbulence structure*

Instantaneous near-bed flow structures are plotted in Fig. 4.1(a) in the form of λ_2-iso-surfaces (Jeong & Hussain, 1995) for the peak phase. There exists a complex forest of highly densed near-bed structures, slightly inclined with respect to the rough-bed. Contrary to the presence of near-wall horseshoe vortex structures in canonical smooth-wall flows, turbulent structures in this case appear to be "broken". This could be due to the fact that, presence of roughness elements typically

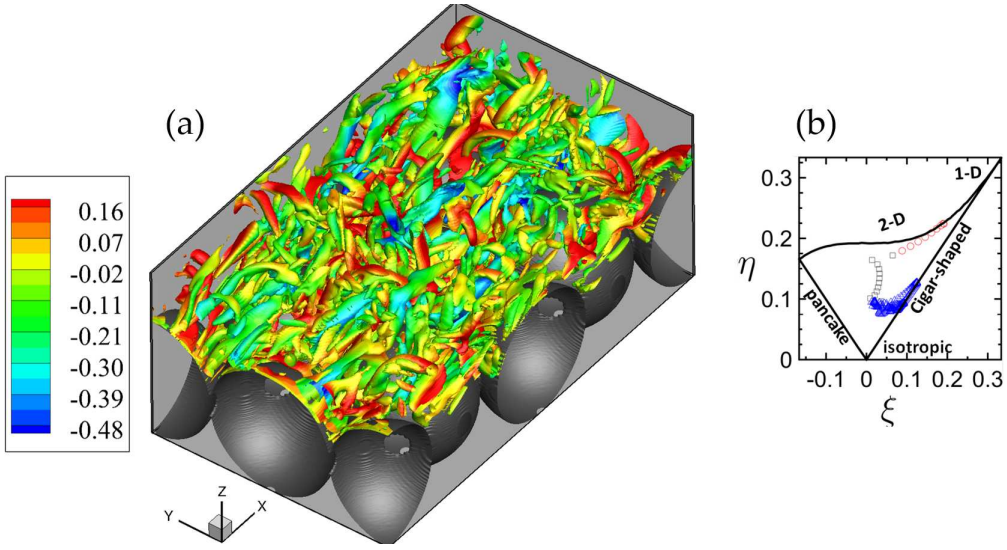

Figure 2.10: For $\mathrm{Re}_\delta = 400$ at peak phase (a) instantaneous iso-surfaces of the λ_2-parameter colored by u'/U_∞. The flow direction is the positive x-direction; (b) the anisotropy invariant map. Here, $\xi = (III_b/2)^{1/3}$ and $\eta = (-II_b/3)^{1/2}$, where II_b and III_b are, respectively, second and third principal invariants of the Reynolds stress anisotropy tensor. Symbols represent: $\circ$, $(z - z_b)/D \lesssim 0.1$; $\square$, $0.1 < (z - z_b)/D \lesssim 0.8$; $\triangle$, $(z - z_b)/D > 0.8$.

energizes wall-normal fluctuations as discussed earlier, that in turn distort these near-bed streamwise structures and cause flow isotropization near the bed; a phenomenon evident from these broken structures. The presence of these structures was speculated by Keiller & Sleath (1976); Sleath (1987); however, were not visualized based on the experimental data. To further quantify this tendency of flow isotropization and study the "shape" of near-bed turbulence, local anisotropy in the Reynolds stresses by constructing the anisotropy invariant map (also known as Lumley's triangle) (Choi, 2001) is quantified, which contains all the possible turbulent states. As seen in Fig. 4.1(b), the data reveals following observations: close to the effective bed location, for $(z - z_b)/D \lesssim 0.1$, two-component type of turbulence is present as wall-normal fluctuations are much weaker compared to streamwise and spanwise ones. Further above this region, $0.1 < (z - z_b)/D \lesssim 0.8$, wall-normal fluctuations gain in strength as discussed earlier, decreasing near-wall anisotropy and the turbulent state crosses over from upper to the lower branch of the triangle (note that the data in this region is almost parallel to η axis indicating reduction in the anisotropy). Further away from the particle crest $(z - z_b)/D > 0.8$, the roughness effects are not pronounced and the cigar-shaped structures dominate, as streamwise fluctuations stay significantly larger than spanwise and wall-normal ones.

Quadrant analysis (Wallace *et al.*, 1972) is also performed to understand the near-bed turbulence structure. Figure 2.11(a) shows phase variation of the quadrant contributions towards the Reynolds stress from ejection, sweep, inward and outward motions collected at a spatial location very close to the roughness crest. In general, significant contributions come from sweep and ejection motions, whereas, contributions from inward and outward motions are minimal. The wall-normal distributions of the quadrant contributions at peak phase are plotted in Fig. 2.11(b), which shows that the sweep motions are more significant below the roughness crest and ejection motions play important role above the crest level. On the other hand, overall contributions from inward and outward motions throughout the fluid column remain insignificant. Fig. 2.11(c) shows instantaneous iso-surfaces of the

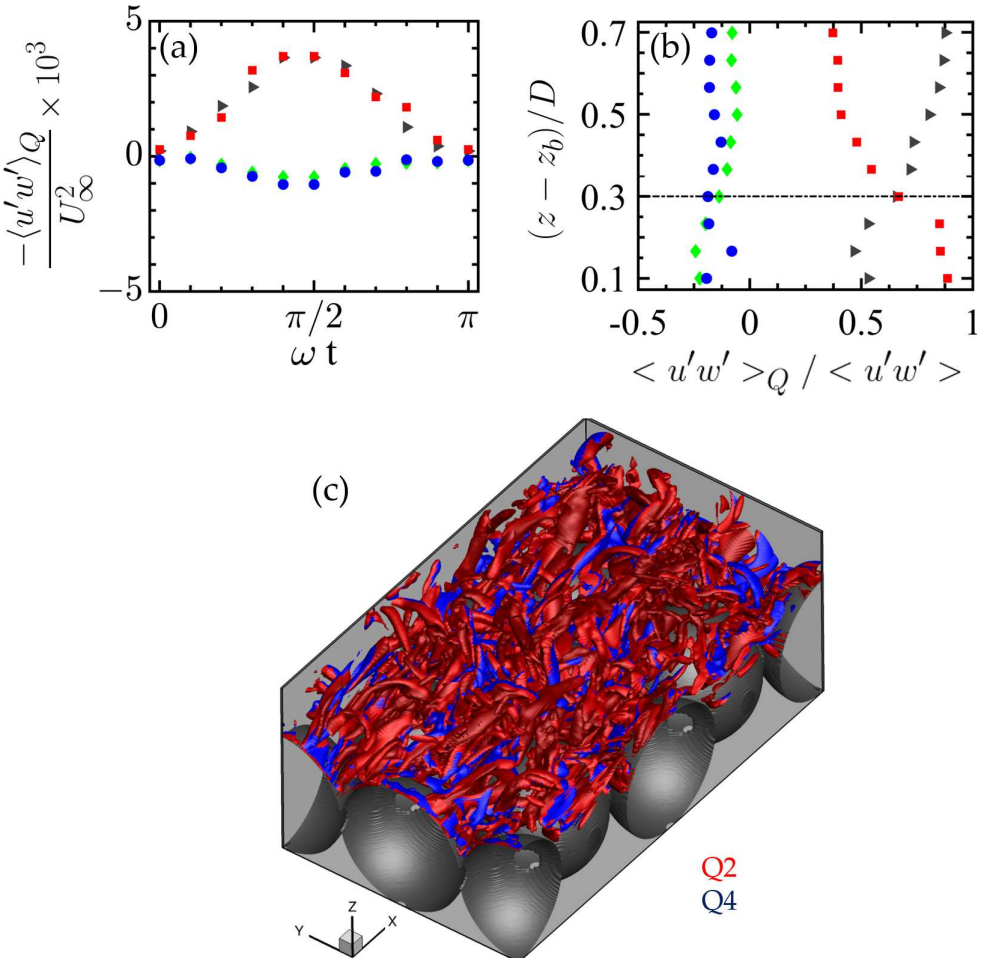

Figure 2.11: For $\mathrm{Re}_\delta = 400$ (a) Phase variation of the quadrant contribution at a location close to the roughness crest; (b) spatial variation of the quadrant contribution plotted at peak phase. Symbols represent: ●, outward; ▶, ejection; ♦, inward; ■, sweep. Here, Q indicates quadrant number; (c) instantaneous isosurfaces of the λ_2-parameter at peak phase colored by ejection (red) and sweep (blue) motions.

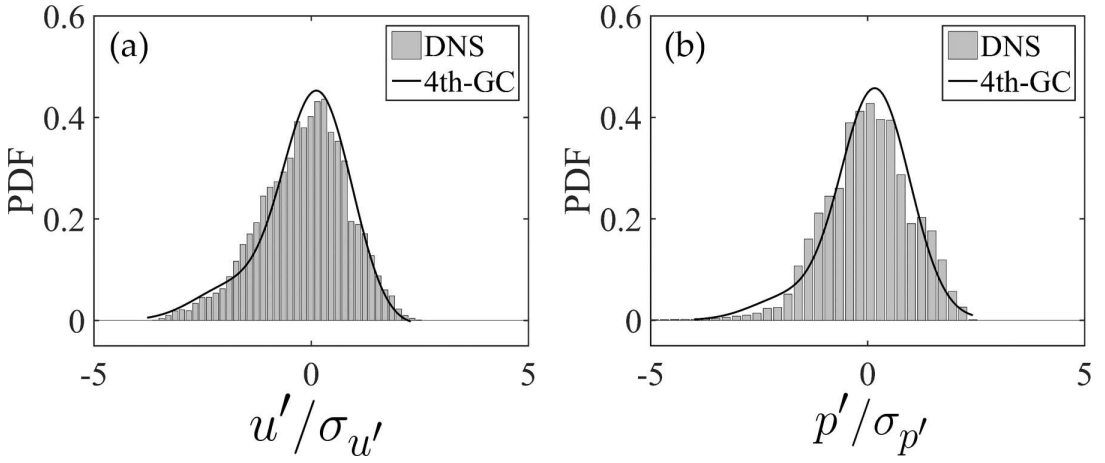

Figure 2.12: For $\mathrm{Re}_\delta = 400$ at a peak phase, PDF of normalized by standard deviations; (a) streamwise velocity and (b) pressure fluctuations. DNS data, recorded at around $0.5D$ above the effective bed location z_b, is represented by histograms and solid line represents fourth-order Gram-Charlier distribution (Eq. 3.2). Skewness $= -0.93$, flatness $= 3.5$ for velocity, whereas skewness $= -0.54$ and flatness $= 4.5$ for pressure fluctuations.

λ_2-parameter (Jeong & Hussain, 1995) colored by indicator function for ejections (red) and sweep (blue) plotted for peak phase, confirming that the upper portion of the near-bed structures relate much closely to the ejection, whereas lower portion of these structures are due to sweep motions. Based on these results, question arises as to what is the distribution of the near-bed flow variables and if an assumption of Gaussian distribution is valid. The probability-density function (PDF) of the near-bed (a) velocity and (b) pressure fluctuations in the region above the rough-bed at a peak phase for $\mathrm{Re}_\delta = 400$, are plotted in Fig. 2.12. As hypothesized, these distributions are highly non-Gaussian, and the PDFs fit well with the fourth-order Gram-Charlier model, given by,

$$f_{GC4}(\psi') = \frac{\exp(-\psi'^2/2)}{\sqrt{2\pi}}\left[1 + \frac{S_{\psi'}}{3!}(\psi'^3 - 3\psi') + \frac{F_{\psi'} - 3}{4!}(\psi'^4 - 6\psi'^2 + 3)\right], \quad (2.5)$$

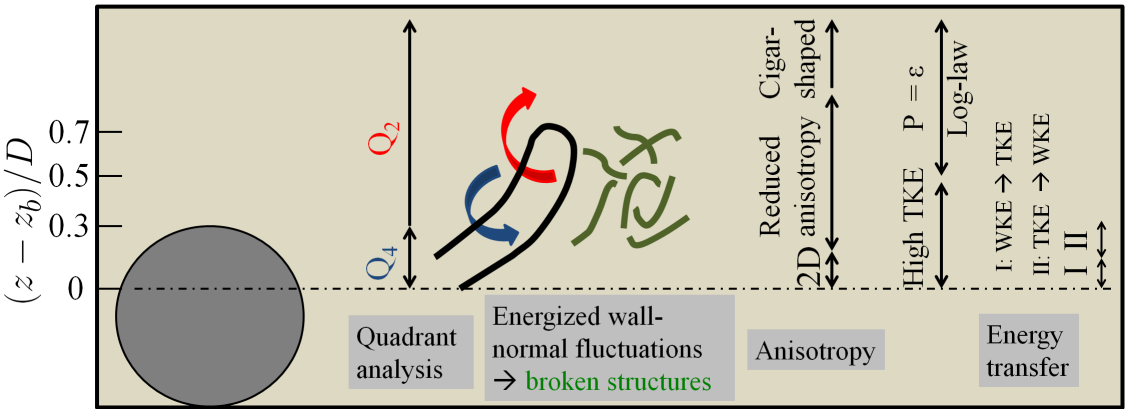

Figure 2.13: Schematic representation (not to scale) to show important near-bed processes.

where ψ' is the normalized fluctuating flow variable, $S_{\psi'}$ and $F_{\psi'}$ are skewness and flatness of its distribution, respectively. The data are recorded at around $0.5D$ above the effective bed location z_b. The choice of this location is based on the high values of correlation between flow parameters and destabilizing hydrodynamic forces on roughness-bed as reported by Ghodke *et al.* (2014*a*), a subject presently under investigation. Similar distributions are observed for all other Reynolds numbers under consideration. The peaked-ness as well as the long positive tails of such distributions can play critical role in destabilizing the particle-bed and therefore should be included in probabilistic models for onset of erosion. Equation 3.2 facilitates incorporation of higher-order flow statistics describing the effect of near-bed bursting phenomena into such models.

2.3.4 *Summarizing near-bed oscillatory turbulence*

A schematic view summarizing important near-bed flow features of oscillatory turbulent flow over a rough-bed is shown in Fig. 2.13.

Although the statistics of turbulent oscillatory flow differ significantly from that

of unidirectional flow, the nature of near-bed processes in oscillatory flow is almost the same as that in unidirectional flow; especially in regards to significant contribution from ejection and sweep motions and reduction in large-scale anisotropy. As indicated in Fig. 2.13, quadrant analysis revealed dominance of sweep motions below the roughness crest and ejection motions above the crest level. Ejections are therefore responsible for flux of TKE away from the wall, whereas sweeps will cause energy diffusion towards the wall. These sweep-burst cycles therefore, may directly influence the sediment particle entrainment and deposition in coastal flows. Similar observations were also reported by Krogstad *et al.* (1992); Yuan & Piomelli (2014*b*) in their study of unidirectional flow.

Also, as in the case of steady flows, presence of roughness is seen to greatly influence these near-bed turbulent structures by redistribution of the energy from streamwise fluctuations to spanwise and wall-normal, causing near-bed flow isotropization and therefore resulting in overall reduction of large-scale anisotropy. Again, these observations are consistent with the unidirectional steady flow literature (Krogstad & Antonia, 1994; Antonia & Krogstad, 2001; Ikeda & Durbin, 2007; Yuan & Piomelli, 2014*b*).

Despite the similar nature of these near-bed flow motions, there exist some differences in the elementary processes that maintain the turbulence production in oscillatory flows. Contrary to the unidirectional flows, bed-induced production terms due to spatial inhomogeneity are comparable to the shear production term. Present data for the gravel-type roughness also indicates energy transfer from WKE to TKE and also from TKE to WKE; latter typically found absent in unidirectional flows (Raupach & Thom, 1981; Raupach *et al.*, 1991; Mignot *et al.*, 2009).

Furthermore, unlike unidirectional flows, all of these important near-bed processes are pronounced for a range of phases in a flow cycle, more so, close to the peak phase for high Reynolds number oscillatory flows. In other words, depending on the friction velocity, turbulence is present only in a part of the oscillation cycle followed by flow re-laminarization. Such time varying nature of near-bed turbulence in oscillatory flows greatly affects destabilizing forces on particle-bed,

a subject of future investigation.

2.4 Conclusions

Particle-resolved DNS of transitional and turbulent oscillatory flows over a rough-bed were performed. Double averaging technique is employed to study spatial heterogeneity at roughness length scale.

Characterization of oscillatory flow in terms of mean velocity distribution, Reynolds stress variation, TKE budget, near-bed flow structures and PDF distributions of velocity and pressure perturbations is reported.

(i) Double-averaged streamwise velocity followed logarithmic law from early-acceleration until mid-deceleration phases ($\omega t = 2\pi/10$ to $7\pi/10$), indicating the presence of fully-developed equilibrium turbulence; also confirmed by the uniform value of structure parameter ($a_1 \approx 0.15$) and the ratio of shear production to dissipation rate close to unity in this region.

(ii) The spatial inhomogeneity at roughness length scale introduced additional production and transport terms in double-averaged TKE budget. Contrary to the unidirectional, steady flows over rough beds, bed-induced production terms, both P_m and P_w, for the present gravel-type roughness, were comparable to the shear production terms, P_s. Negative peak in P_w at the roughness crest level was observed and could be attributed to the conversion of turbulent kinetic energy to wake kinetic energy as a result of work of large-scale structures associated with $\langle\overline{u'^2}\rangle$ at this location against pressure drag of roughness elements. Secondary positive peak in P_w is observed close to the effective bed location, indicating the conversion of wake kinetic energy to turbulent kinetic energy of scales smaller than roughness length scale at this location. Bed-induced transport term was found to be negligible.

(iii) Increasing the effective roughness energized wall-normal fluctuations while dampened the streamwise ones. This led to break-up of streamwise near-bed structures and caused reduction in large-scale anisotropy. As a result, broadly two separate regions, a near-bed region of two-component turbulence and an outer region

of cigar-shaped turbulence were observed.

(iv) Quadrant analysis showed dominance of ejection and sweep type motions over inward/outward interactions. The wall-normal distributions of the quadrant contributions showed that the sweep motions are more significant below the roughness crest and ejection motions play important role above the crest level.

(v) The PDF distributions of the velocity and pressure fluctuations showed a non-Gaussian behavior that followed a fourth-order Gram-Charlier distribution, indicating importance of higher-order turbulence statistics. This finding is especially critical for the development of probabilistic models of sediment erosion.

Acknowledgments

This work is supported by the National Science Foundation (NSF-CBET - 1133363). The computations were performed on the Texas Advanced Computing Center's Stampede machine. Authors thank Dr. Javier Urzay of Stanford University for fruitful discussions during the CTR Summer Program 2014. Authors also thank anonymous reviewers for useful suggestions leading to the improvement of the manuscript.

Chapter 3: Spatio–temporal analysis of hydrodynamic forces on the particle-bed in an oscillatory flow environment

Chaitanya D. Ghodke and Sourabh V. Apte

to be submitted to
Journal of Fluid Mechanics
Cambridge University Press

Abstract

A numerical investigation of unsteady hydrodynamic forces on the particle-bed in an oscillatory flow environment is performed by means of direct numerical simulations (DNS). Statistical descriptions of drag and lift forces for two particle sizes of diameter 375 and 125 in wall units corresponding to the large size gravel and the small size sand particle, respectively, in a very rough turbulent flow regime are reported. Characterization of unsteady forces in terms of spatial distribution, temporal auto-correlation, force spectrum as well as cross-correlations with measurable flow variables is carried out. Based on the concept of impulse, intermittency in drag and lift forces is also investigated.

Temporal correlations show drag and lift to be positively correlated with a time-delay, that is approximately equal to the Taylor micro-scale related to the drag/lift fluctuations. The force spectra for drag and lift reveal roughly two scaling regions, $-11/3$ and $-7/3$; former typically represents turbulence–mean-shear interactions, whereas latter indicates dominance of turbulence–turbulence interactions. Particle forces are strongly correlated with streamwise velocity and pressure fluctuations in the near-bed region for both flow cases. In comparison to the gravel case, the spatial extent of these correlations is $2-3$ times larger in homogeneous directions for the sand particle, a feature that is reminiscent of longer near-bed structures typically found in the sand case.

It is shown that the distributions of drag (lift) fluctuations, in particular, peaked-ness and long tails match remarkably well with fourth-order Gram-Charlier distributions of velocity (pressure) fluctuations. Furthermore, it is demonstrated that the intermittency is larger in the case of lift force compared to that for the drag. Distributions of impulse events are heavily and positively skewed and are well described by General extreme value distribution.

3.1 Introduction

Essential to the study of sediment transport is the criterion for onset of erosion, as it defines the threshold conditions for initiation of the sediment motion, also known as incipient motion and is often used to set a lower bound in the models to predict the transport of sediment particles. The prediction of such erosion onset to describe threshold of bed mobility has attracted many researchers in the past (Bagnold, 1966; Fredsøe & Deigaard, 1992; Sleath, 1995; Flores & Sleath, 1998; Cheng & Chiew, 1998; Sleath, 1999; Nelson *et al.*, 2000; Papanicolaou *et al.*, 2002; Nino *et al.*, 2003; Cheng & Law, 2003; Wu & Chou, 2003; Wu & Kuo-Hsin, 2004; Hofland & Battjes, 2006).

These flows are typically turbulent in nature and to study the dynamics of particle-bed mobility, it is important to understand the complex interactions between turbulence and sediment grains. Turbulent flow induces fluctuating forces on the particle-bed, that if exceed a critical threshold, can strip the particles off the bed, suspend them in the fluid and deposit them elsewhere. Furthermore, Diplas and co-workers (Diplas *et al.*, 2008; Valyrakis *et al.*, 2010; Celik *et al.*, 2010, 2013) introduced the concept of impulse and indicated that, along with the temporal bursts in drag or lift forces above a critical threshold, the duration over which they act are also critical in predicting the onset of erosion. On the other hand, the presence of particles is also seen to greatly affect the structure of the near-bed turbulence, indicated by increased bed shear stress, reduction in the near-bed anisotropy, and marked changes in turbulent energy transport mechanisms (Krogstad *et al.*, 1992; Krogstad & Antonia, 1994; Krogstad *et al.*, 2005; Ikeda & Durbin, 2007; Chan-Braun & Uhlmann, 2011; Yuan & Piomelli, 2014*b*; Kempe *et al.*, 2014; Ghodke & Apte, 2016). As a result of interdependence, the prediction of erosion onset, therefore, often requires linking destabilizing hydrodynamic forces on the particle-bed to the turbulent motion of fluid around it.

Several studies have been reported so far to provide indirect estimation of hydrodynamic forces on the particle-bed using local pressure measurements (Rosenthal & Sleath, 1986; Hofland *et al.*, 2005; Hofland & Battjes, 2006; Schmeeckle

et al., 2007; Dwivedi *et al.*, 2010; Detert *et al.*, 2010; Amir *et al.*, 2014). However, owing to the experimental difficulties, detailed spatial structure and temporal characteristics of the fluctuating hydrodynamic forces on the particle-bed yet remain elusive. Recently, Chan-Braun & Uhlmann (2011) reported spatio–temporal characteristics of particle forces in an unidirectional, steady open-channel flow in the low Reynolds number regime by means of DNS. Although, such fully-resolved simulations can provide high-fidelity data of particle forces without requiring any *ad hoc* models, generally are extremely challenging and require enormous computational cost for large Reynolds number turbulent flows in the rough regime.

Alternative approaches for estimating particle forces to predict erosion onset include use of statistical tools. Based on theoretical derivations, statistical data of particle forces are calculated indirectly by assuming a cross-correlation with Gaussian or log-normal near-bed velocity fluctuations (Einstein, 1950; Cheng & Chiew, 1998; Papanicolaou *et al.*, 2002; Cheng & Law, 2003; Wu & Chou, 2003; Wu & Kuo-Hsin, 2004; Hofland & Battjes, 2006). However, recent studies show that the near-bed flow dynamics, roughness effects, and flow through porous regions lead to non-Gaussian velocity fluctuations and higher-order turbulence statistics such as kurtosis and skewness are necessary for better predictions (Wu & Kuo-Hsin, 2004; Ghodke & Apte, 2016). Moreover, it is also unclear, whether, up to what spatial extent such cross-correlations of forces with near-bed turbulent flow exist.

Most of the aforementioned studies pertaining to this topic are reported for unidirectional, steady flows. However, detailed information of spatio–temporal characteristics of the hydrodynamic forces on the particle-bed in an oscillatory, non-stationary turbulent flow representative of coastal environment has not been documented. The scope of the present paper is to analyze, by means of numerical experiments, spatial structure and temporal characteristics of unsteady hydrodynamic forces on the rough-bed made up of hexagonal pack of fixed spherical particles in a symmetric and sinusoidally oscillating flow for Reynolds numbers in the turbulent rough regime. To study the effects of roughness size, particles of

diameters 375 and 125 wall units, former corresponds to large size gravel particle while latter represents smaller sand particle, are studied. Statistical descriptions of drag and lift forces on the particle-bed along with their cross-correlations with near-bed turbulent motions are also reported. Based on the concept of impulse, investigation of critical threshold of drag and lift forces is carried out. To the best of our knowledge, no such detailed characterization of unsteady hydrodynamic forces on the particle-bed in an oscillatory flow environment using DNS has been reported to date. The outline of the paper is as follows: the flow configuration and methodology are presented in § 2, simulation results are presented in § 3, followed by main conclusions in § 4.

3.2 Flow configuration

The overall flow configuration is similar to the setup of oscillatory flow over a layer of spherical particles studied in Ghodke & Apte (2016). As shown in Fig. 3.1, x, y and z are, respectively, the streamwise, spanwise and wall-normal directions and u, v and w are the velocity components in those directions. The computational domain shown in Fig. 3.1 consists of a doubly periodic box in streamwise and spanwise directions. The rough-bed is formed by a single layer of hexagonal pack of fixed spherical particles that are touching each other. A smooth no-slip wall is located at $z = 0$ and a slip wall at $z = 45\delta$, where $\delta = \sqrt{2\nu/\omega}$ is the Stokes-layer thickness, ν is the kinematic viscosity, $\omega = 2\pi/T$ is the oscillation frequency and T is the period of the wave. In this notation, hydrodynamic force components in the streamwise x-direction and wall-normal z-direction are denoted as drag and lift force, respectively. Considering an instantaneous value of the variable ϕ, its fluctuation with respect to phase and spatial average over wall-parallel planes is defined as, $\phi' = \phi - \langle\overline{\phi}\rangle$. Here, an overbar and brackets, respectively, denote phase and homogeneous spatial averages. Note that, in the context of double-averaging, the fluctuating quantity ϕ' includes contribution from spatial disturbance resulting from flow inhomogeneity at the roughness length scale (Ghodke & Apte, 2016).

Case	D/δ	Re_δ	Re_a	Re_D	k_s^+	D^+	$f_{w,max}$	D/Δ_x	D/Δ_y	D/Δ_z	a/k_s	Regime
Gravel	6.95	400	80000	2780	745	375	0.036	40	55	300	14.4	rough turbulent
Sand	2.68	545	148500	950	250	125	0.015	15	20	100	50	rough turbulent

Table 3.1: Computational parameters and grid resolution details: $\mathrm{Re}_\delta = U_\infty \delta/\nu$ is the Reynolds number based on the Stokes-layer thickness, $\mathrm{Re}_a = U_\infty a/\nu$ is the Reynolds number based on the wave amplitude, $\mathrm{Re}_D = U_\infty D/\nu$ is the particle Reynolds number, $k_s^+ = u_{\tau,max} k_s/\nu$ is the effective roughness Reynolds number and $D^+ = u_{\tau,max} D/\nu$ is the particle size in wall units. Here, U_∞ is the amplitude of the free-stream velocity, $a = U_\infty/\omega$ is the amplitude of wave oscillation, $k_s \approx 2d$ is the Nikuradse roughness size and $u_{\tau,max}$ is the maximum friction velocity in a flow cycle. Maximum value of a wave friction factor, $f_{w,max} = 2\left(u_{\tau,max}/U_\infty\right)^2$ is also given. Details of calculation of friction velocity are given in Ghodke & Apte (2016). Present study assumes low Froude numbers.

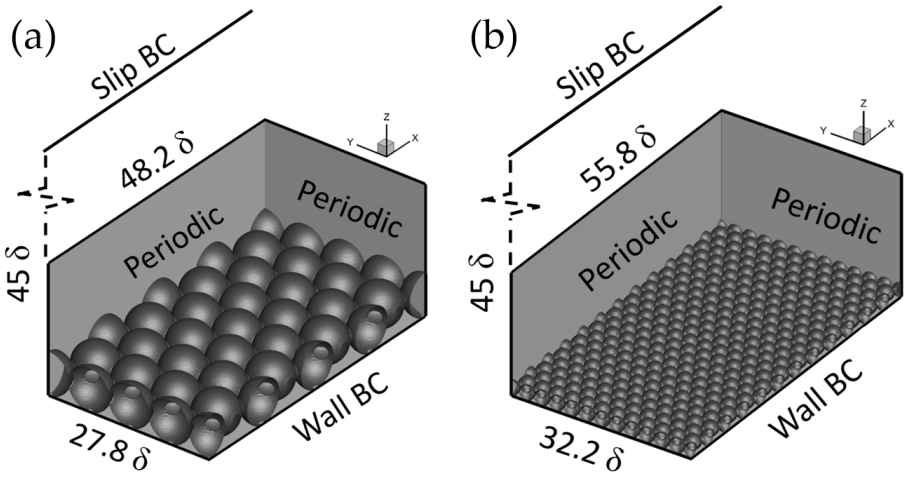

Figure 3.1: Close-up view of the computational domain and boundary conditions for (a) gravel and (b) sand case. A harmonic pressure forcing is imposed that results in a streamwise velocity component $U_\infty \sin(\omega t)$ far from the bed.

The dimensionless parameters to characterize the flow are outlined in Table 3.1. To study the effects of particle size on spatio–temporal characteristics of force statistics, two sizes of particle diameter normalized by the Stokes-layer thickness, $D = d/\delta$, corresponding to the large size gravel ($D = 6.95$) and small size sand particle ($D = 2.68$) are studied. Figure 3.2 maps the different flow cases on a regime diagram ($a/k_s - Re_a$) for oscillatory flow over roughness elements depicting the limits of laminar, transitional, smooth turbulent and rough turbulent regimes. Present case of the gravel ($a/k_s = 14.4$) and the sand particle ($a/k_s = 50$) at given Reynolds numbers correspond to very rough turbulent regime, latter approaching the limit of rough turbulent regime. Table 4.1 also tabulates the flow parameters and spatial resolutions used in this study. As described in Ghodke & Apte (2016), uniform grids, although not cubic, are used only in the region surrounding the particles giving roughly around 100 to 300 points in the wall-normal direction per particle diameter, and the grids are stretched in the flow normal direction above z = $8\delta(6\delta)$ for the gravel (sand) using hyperbolic tangent function typically

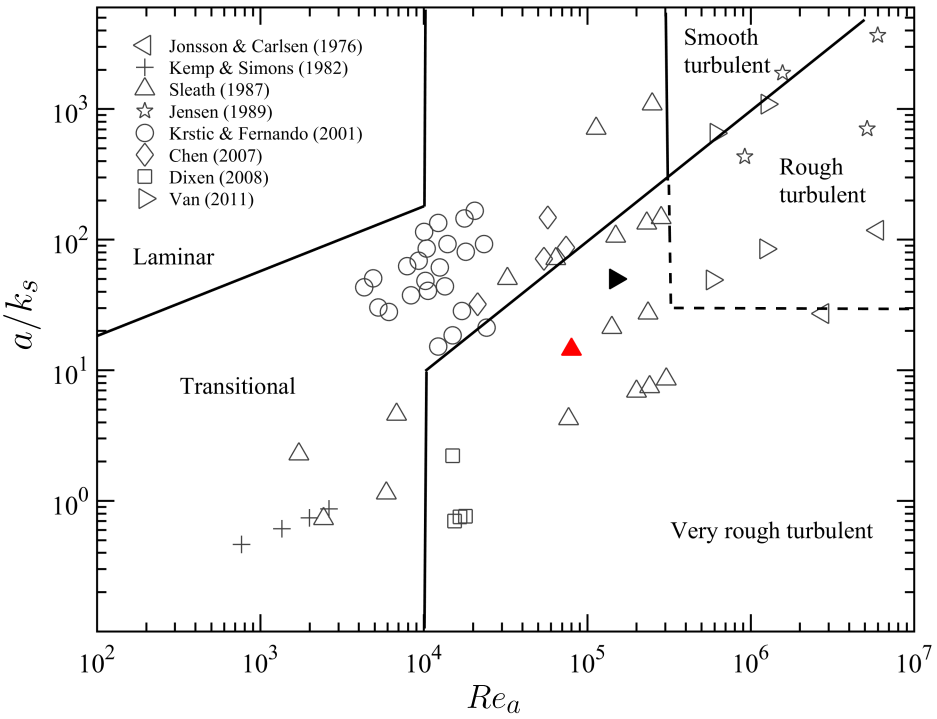

Figure 3.2: Delineation of different flow regimes for oscillatory flow illustrating previous studies (Jonsson & Carlsen, 1976; Kemp & Simons, 1982; Sleath, 1987; Jensen *et al.*, 1989; Krstic & Fernando, 2001; Chen *et al.*, 2007; Dixen *et al.*, 2008; van der A *et al.*, 2011) and present cases. Symbols represent: ▲, $\mathrm{Re}_\delta = 400$ (gravel); ▶, $\mathrm{Re}_\delta = 545$ (sand).

used in boundary layer and channel flow calculations (Kim *et al.*, 1987; Moin & Mahesh, 1998). Around 15 flow cycles per case are computed to obtain statistical convergence.

As indicated in Fig. 3.1, the flow domain is around $48\delta(56\delta)$ long in the flow direction, $28\delta(32\delta)$ wide in the spanwise direction and 45δ in the wall-normal direction for the gravel (sand) case. Compared to Ghodke & Apte (2016), larger domains are used in the present study to incorporate more particles in order to obtain sufficient samples for force statistics. Vertical size of the domain is chosen such that all turbulent statistics decay to zero at almost half the vertical height for large Reynolds number sand case under consideration. See Appendix A and Appendix B for details.

The numerical solver based on fictitious domain algorithm (Apte & Finn, 2013), that facilitates solution of freely moving particles for a wide range of fluid-particle density ratios is used, although the particles are held fixed in the present study. The solver is fully validated for a range of test cases including flow over a cylinder and sphere for different Reynolds numbers, flow over touching spheres at different orientations, flow developed by an oscillating cylinder, laminar and turbulent flow through porous media, among others. The details of the algorithm as well as very detailed verification and validation studies have been published elsewhere (Apte *et al.*, 2008; Apte & Finn, 2013). In addition, present configuration of oscillatory flow over rough-bed is also validated against experimental data of Keiller & Sleath (1976) for the gravel particle at $\mathrm{Re}_\delta = 95$ as shown in Ghodke & Apte (2016). In particular, variation of peak velocity magnitude and the phase at which this peak velocity is recorded, plotted at various heights above the roughness crest are shown to agree reasonably well with experimental work of Keiller & Sleath (1976). Other numerical predictions or parameters such as friction factor and boundary layer thickness for the gravel particle over a range of Reynolds numbers, $\mathrm{Re}_\delta = 95 - 400$, also show good comparison with experimental data, further confirming adequacy of the computational domain, grid resolution and rigid body treatment (Ghodke & Apte, 2016).

3.3 Results and discussion

In this section, spatio–temporal characteristics of unsteady drag and lift forces on the particle-bed are presented. To begin with, differences in the near-bed flow structures in the gravel and the sand case are discussed.

3.3.1 *Flow structures*

As noted in Table 3.1, the amplitude based Reynolds number (Re_a) in the sand case is almost two times larger than that in the gravel case. On the other hand, effective roughness Reynolds number (k_s^+) in the gravel case is almost three times higher than that in the sand case. As a result, there exist some discernible differences in the elementary processes that govern the near-bed turbulence in the gravel and the sand particle case.

For the gravel-type roughness, a/k_s is smaller (large roughness size) compared to that for the sand particles. The size of the individual gravel particle is large enough to cause vortex shedding that is in a way also responsible for triggering the turbulence much earlier in the flow cycle (Ghodke & Apte, 2016). Contrary to this, as a result of large a/k_s value (smaller roughness size) of the sand-type roughness, the near-bed flow exhibits an unsteady inertial behavior in the early acceleration cycle, until the local friction velocity is large enough to trigger the turbulence. This behavior is evident from Fig. 3.3 where product of instantaneous streamwise (u) and wall-normal (w) velocity is plotted for (a) gravel and (b) sand case. The significant vortex shedding along with sweep-bursts motions in the gravel case result in strong cross-correlation signal uw from the beginning of the flow cycle. However, as shown in Fig. 3.3(b), such cross-correlation is significant for the sand case only from peak phase to late deceleration phases where inertial effects play an important role in triggering the turbulence.

To further elucidate the near-bed flow behavior, instantaneous flow structures in the form of λ_2-iso-surfaces (Jeong & Hussain, 1995) are plotted at the peak phase in Fig. 3.4 for (a) gravel and (b) sand particle. For the gravel-bed, there exists

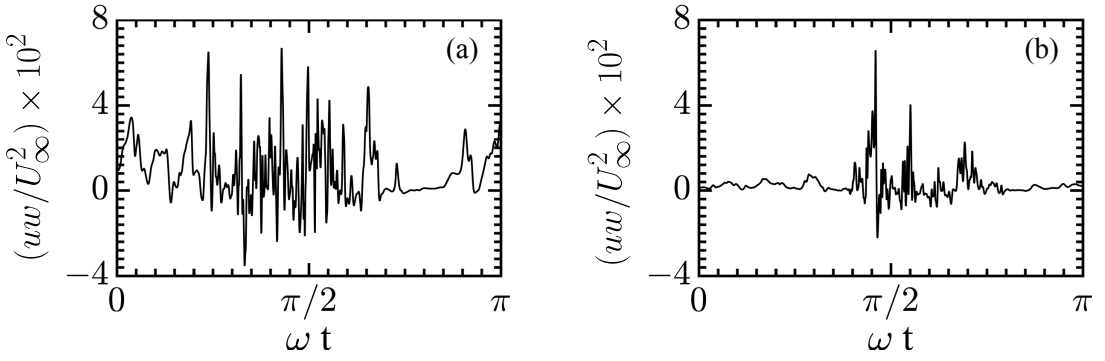

Figure 3.3: Variation over a half cycle of the normalized product of instantaneous streamwise (u) and wall-normal (w) velocity plotted for (a) gravel and (b) sand case.

a complex forest of highly densed near-bed structures that appear to be broken and are slightly inclined with respect to the horizontal direction. The disruption of these flow structures is an artifact of energized wall-normal velocity fluctuations in the gravel case that in turn distort the streamwise structures resulting in flow isotropization, as already discussed in Ghodke & Apte (2016). On the other hand, presence of larger elongated horseshoe structures that span over more than few particles diameter in the flow direction along with the small-scale broken structures is clearly evident in the sand case shown in Fig. 3.4 (b). Contrary to the gravel, these structures appear to be less broken, suggesting lower degree of near-bed flow isotropization in the sand case. Such near-bed structures could play a significant role in influencing spatio–temporal characteristics of hydrodynamic forces on the particle-bed. Detailed quantification of the near-bed turbulence structure in the gravel and the sand particle case is a subject of future investigation.

3.3.2 *Particle-bed force history*

In the following, nature of unsteady forces on the particle-bed is analyzed. Figure 3.5 shows phase variation of instantaneous drag/lift forces on each particle (thin

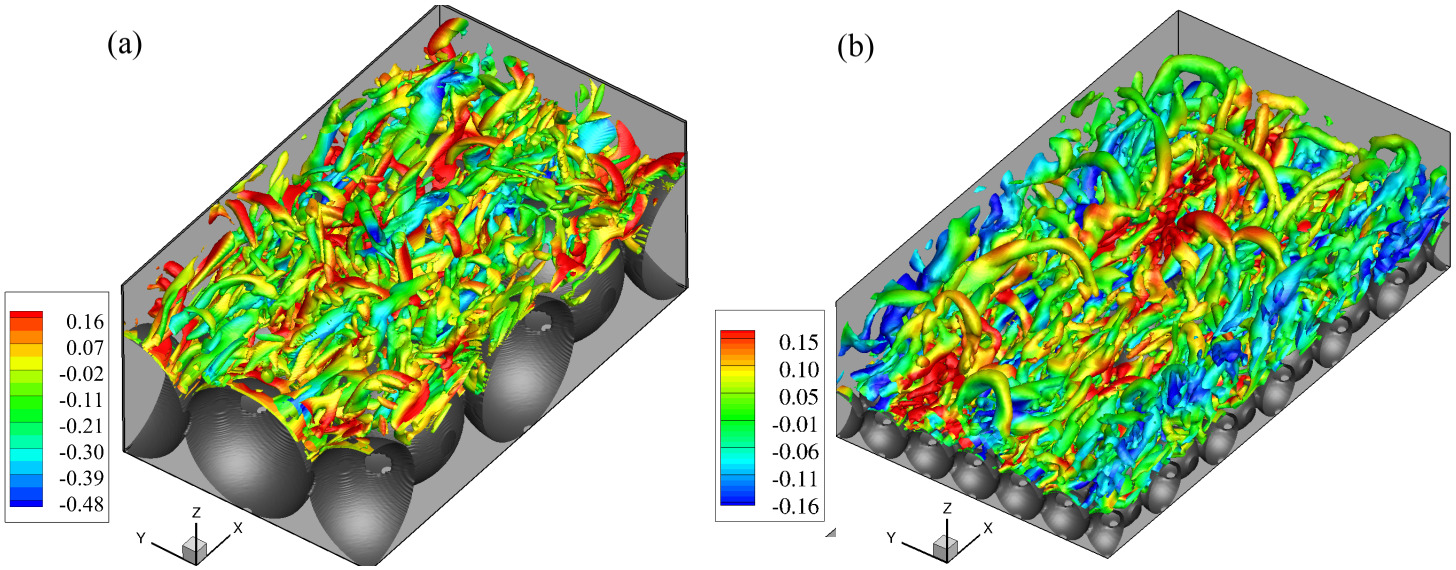

Figure 3.4: Close-up view of the instantaneous iso-surfaces of the λ_2-parameter colored by u'/U_∞ for (a) gravel and (b) sand case plotted at a peak phase, $\omega t = 5\pi/10$. The flow direction is the positive x-direction.

black lines) plotted along with the average force on the particle-bed (thick red line). For the illustration purpose, data for 4 cycles are plotted. Figure 3.5 (a) and (b), respectively, show drag (C_D) and lift (C_L) coefficient in the gravel case and Fig. 3.5 (c) and (d) show that in the sand case. Phase variation of the streamwise velocity far from the bed is also shown for the reference. Contrary to unidirectional flows, average force on the particle-bed in oscillatory flows varies over a cycle. As seen in Fig. 3.5 (a) and (b) the variability of the instantaneous forces on each sphere from the average value is significant throughout the entire cycle for large diameter gravel case. On the other hand, such variability of the instantaneous forces is significant only from late acceleration up to early deceleration phases for the sand particle case as shown in Fig. 3.5 (c) and (d). Such differences in the force history for the gravel and the sand case are mainly a result of different nature of the near-bed turbulence in both flow cases as discussed earlier.

To further elucidate the differences in the nature of gravel and sand particle forces, phase variation of the average force on the particle-bed in both flow cases is discussed in detail. Figures 3.6 shows variation over a cycle of the normalized phase-averaged force on the particle-bed in the streamwise ($\overline{C}_D$, coefficient of drag) and wall-normal ($\overline{C}_L$, coefficient of lift) direction for the gravel- and sand-type roughness. Phase variation of the streamwise velocity far from the bed is also shown for the reference.

Unlike drag, sign for the lift force is the same whether the flow is in the positive or negative x-direction and has a period of half the forcing function. In the case of gravel shown in Fig. 3.6 (a), both drag and lift coefficients peak earlier in the flow cycle, respectively exhibiting the phase-lag of $\omega t = 0.87$ and 0.34 with the free-stream velocity. In comparison, as a result of increased Reynolds number Re_a in the sand case, reduced phase-lag of respectively, $\omega t = 0.080$ and 0.086 for drag and lift with the free-stream velocity is observed as shown in Fig. 3.6 (b). Note that, the phase-lag between drag and lift force also decreases as the Reynolds number is increased as in the sand case.

As seen in Fig. 3.6 (b), there exist sharp spikes in the drag and lift records

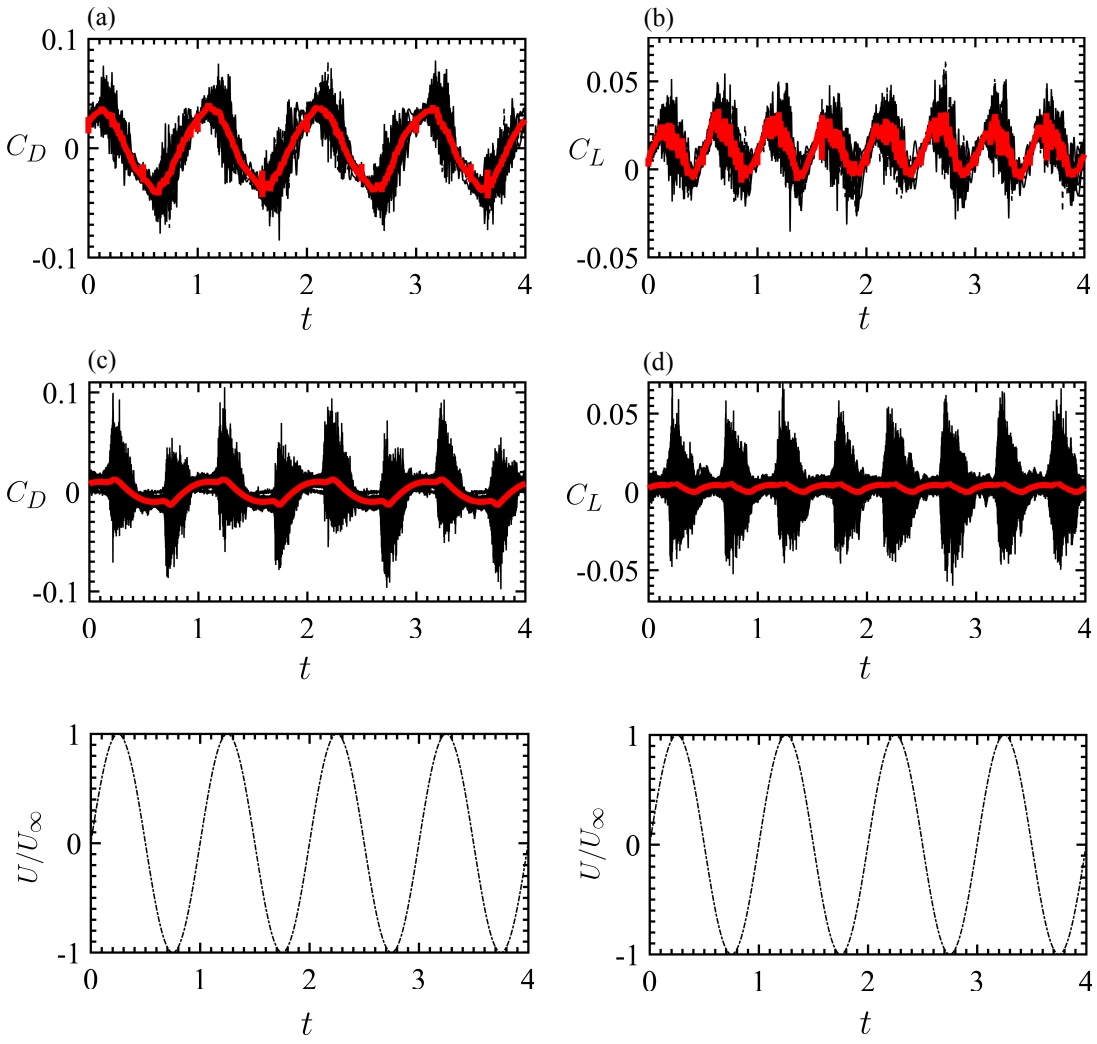

Figure 3.5: Variation over several cycles of the normalized instantaneous drag, C_D plotted in (a,c) and lift, C_L plotted in (b,d) for each particle in the flow setup. Panels (a,b) are for the gravel case and panels (c,d) are for the sand case. Thick red line indicates average value of the force. Here, $C_i = F_i/(0.5\rho A_p U_\infty^2)$ is the instantaneous force on a particle, i stands for drag or lift, A_p is the area of a particle. Phase variation of the streamwise velocity far from the bed is shown by (- - -).

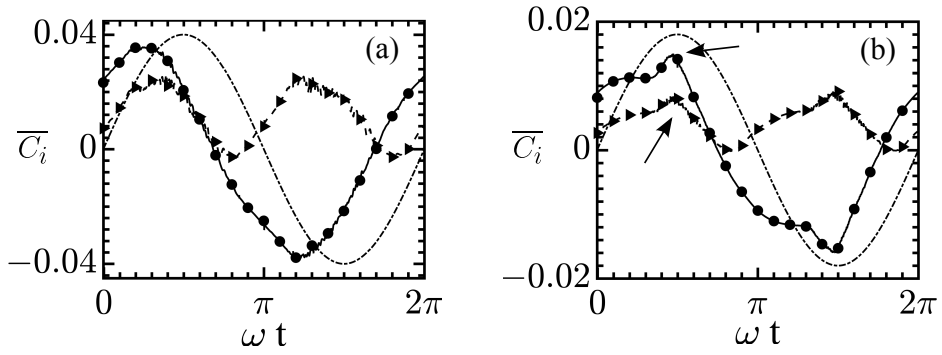

Figure 3.6: Variation over a cycle of the normalized phase- and spatially-averaged drag, $\overline{C}_D$ (—•—) and lift, $\overline{C}_L$ (- - -▶- - -) for (a) gravel and (b) sand case. Here, $\overline{C_i} = \langle\overline{F_i}\rangle/(0.5\rho A_b U_\infty^2)$ is the normalized phase- and spatially-averaged force on the particle-bed, i stands for drag or lift, A_b is the total projected area of the particle-bed. Phase variation of the streamwise velocity (not to scale) far from the bed is shown by (···). Arrows in (b) indicate spikes in the drag and lift record for the sand case.

for the sand case, however, such distinct spikes are absent in the gravel case. As a result of significant vortex shedding along with sweep-burst motions, there is no clear demarcation of onset of turbulence that may result in distinct spikes in the drag and lift forces on the gravel-bed. Contrary to this, occurrence of sweep-bursts motions resulting into sudden transition to turbulence close to the peak velocity phase results in distinct spikes in the drag and lift record in the sand case. Note that, the phase instant of these spikes in Fig. 3.6 (b) matches clearly well with spikes in the uw signal for the sand case shown in Fig. 3.3 (b).

Table 3.2 summarizes the particle-bed force statistics for the gravel and the sand-type roughness. In both the cases, the net lift and drag coefficients remain positive and their magnitude is decreased as the Reynolds number is increased. The higher-order moments such as skewness and kurtosis of drag/lift fluctuations over several half flow cycles are also reported in Table 3.2. In both flow cases, skewness values of drag and lift forces are positive, indicating that the positive events of drag and lift are more likely to occur than the negative ones. Moreover,

Case	$\overline{C}_{D,max}$	$\overline{C}_{L,max}$	$\overline{C}_{D,avg}$	$\overline{C}_{L,avg}$	$S_{D'}$	$S_{L'}$	$K_{D'}$	$K_{L'}$
Gravel	0.036	0.026	0.013	0.012	0.12	0.0012	4.8	4.4
Sand	0.015	0.0087	0.0062	0.0041	0.56	0.018	8.3	7.8

Table 3.2: Force statistics for the particle-bed of gravel and sand-type roughness. Here, $\overline{C}_{D,max}$ ($\overline{C}_{L,max}$) and $\overline{C}_{D,avg}$ ($\overline{C}_{L,avg}$) respectively show maximum and period-averaged value of the drag (lift) force coefficient over a half flow cycle; $S_{D'}(S_{L'})$ and $K_{D'}(K_{L'})$ respectively denote skewness and kurtosis of the drag (lift) fluctuations over a half flow cycle.

high values of kurtosis of drag and lift fluctuations indicate large intermittency in the force-field that results in longer tails of rare but strong events. With increase in Reynolds number (sand case) such extreme events become stronger, resulting in higher values of kurtosis. Take a note that, kurtosis values in the sand case are almost two times larger than that in the gravel case. Such extreme force events might play an important role in destabilizing the particle-bed. Similar observations were reported by Chan-Braun & Uhlmann (2011) in their study of unidirectional flow over a rough-bed.

3.3.3 *Spatial distribution of the forces*

After studying phase variation of the drag/lift forces, their distribution on the particle surface needs to be investigated. In the following, spatial distribution at a peak phase of the phase-averaged drag and lift force on the gravel and the sand particle is plotted in Fig. 3.7. Here, Fig. 3.7 (a), (b) show isometric view and Fig. 3.7 (c), (d) present top view of the particle. Panels (a,c) and (b,d) show force distribution on the gravel and the sand particle, respectively. Note that, the drag and the lift force plotted in Fig. 3.7 indicate phase- and spatially-averaged forces. Therefore, the spheres shown in this figure do not represent a particular particle but rather show an averaged force-field on any particle in the setup. As shown in

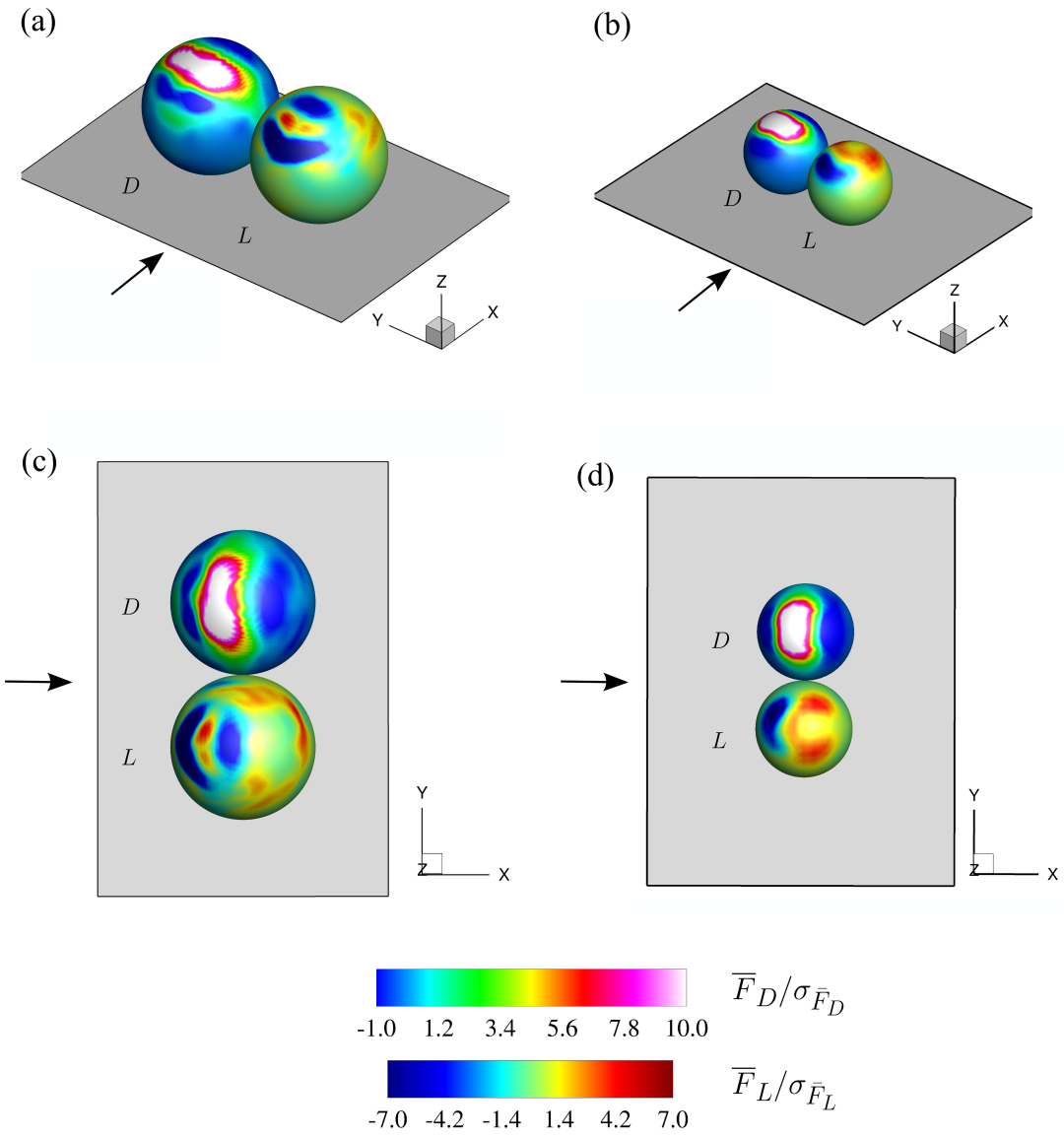

Figure 3.7: Spatial distribution of the phase- and spatially-averaged drag ($\overline{F}_D$) and lift ($\overline{F}_L$) force at a peak phase normalized by their respective standard deviations for the gravel (a,c) and the sand (b,d) particle. Here, D and L, respectively, denote drag and lift force. The direction of the flow is indicated by an arrow. Sizes of the particles are not to scale.

Fig. 3.6, average forces on the particle at the peak phase in both flow cases are positive, however, local drag/lift force can either be positive or negative depending on the direction of the local velocity near the particle surface.

For both gravel and sand case, there exists a region of strong positive drag near the top of the sphere, a result of maximum strain in the streamwise velocity component at this location. Also, owing to the pronounced curvature effects due to larger particle size, a region of smaller positive drag is also present in the front and aft side of the gravel as seen in Fig. 3.7 (a,c); however, is clearly absent in the sand case shown in Fig. 3.7 (b,d).

The small patches of weak positive drag found especially in the case of gravel are artifacts of pore-scale flow features and are dominant mainly in the larger size particle-bed. Furthermore, variation of the drag force in the wall-normal direction reveals the location of the effective level at which the bulk drag force is exerted, also called zero-displacement plane. In the present study, this zero-displacement plane is found to be located at $0.7D$ ($0.85D$) for gravel (sand) particle. This further indicates that the total drag force is distributed on a larger area of the upper hemisphere of the gravel compared to that in the case of the sand particle.

The spatial distribution of the lift force also shows some discernible differences between the gravel and the sand particle. As shown in Fig. 3.7 (b,d), the lift force of positive magnitude is distributed mostly in the top portion of the upper hemisphere of the sand particle and is a result of lower values of pressure due to flow acceleration near the particle crest. On the other hand, lift distribution in the case of gravel particle shows larger positive magnitudes on the side and aft region of the particle as shown in Fig. 3.7 (a,c). This could be attributed to the combined effects of enhanced three-dimensionality of the boundary layer and shielding effects in a hexagonal arrangement of the particles along with the complex pore-scale flow in the gaps between the particles. As a result, lower pressure regions are mainly observed on the side and aft portion of the gravel particle that contribute positively to the lift. In comparison to the sand case, these effects are more pronounced for the large diameter gravel particle due to strong curvature effects.

3.3.4 *Temporal correlations of the forces*

In the following, temporal characteristics of the force fluctuations on the gravel and the sand particle-bed are studied. Time scales of drag and lift fluctuations in both flow cases are obtained from their respective temporal auto-correlations. In addition, cross-correlation of drag and lift fluctuations is also reported to reveal their interdependence on each other.

Following Chan-Braun & Uhlmann (2013), three-dimensional correlation function given as,

$$R_{\phi'\psi'}(\Delta x, \Delta y, z, \Delta t) = \frac{1}{N_c N_p} \sum_{i=1}^{N_c} \sum_{j=1}^{N_p} \phi'(x_{p,j}, y_{p,j}, z_{p,j}, t_i)\ \psi'\left[(x_{p,j} + \Delta x), (y_{p,j} + \Delta y), z, (t_i + \Delta t)\right] \tag{3.1}$$

is defined, where the sub-index p refers to the particle position, and N_p and N_c are the number of particles and flow cycles, respectively. Using this function, temporal auto-correlation at zero spatial separation can be calculated by setting $\phi' = \psi'$ and $\Delta x = \Delta y = 0$ in Eq. 3.1. Figure 3.8 shows variation of auto-correlation function of drag (solid line) and lift (dashed line) fluctuations for (a) gravel and (b) sand particle case.

In the case of gravel, auto-correlation functions for drag and lift exhibit local minima of small negative values (drag: -0.066 at $\Delta t U_\infty/d = 3.1$ and lift: -0.039 at $\Delta t U_\infty/d = 2.9$). For the sand case, the local minimum in the drag takes positive value (0.087 at $\Delta t U_\infty/d = 2.1$) and that for the lift takes negative value (-0.024 at $\Delta t U_\infty/d = 3.2$). Chan-Braun & Uhlmann (2013) in their DNS study of unidirectional flow over a rough-bed also observed such local minima in drag/lift auto-correlations. They argued that the minimum peak in drag/lift auto-correlations might be linked to the effects of pressure; analogous to a pronounced minimum of negative value of pressure auto-correlation on a smooth wall in a turbulent channel flow. The present results also show similar trends, however,

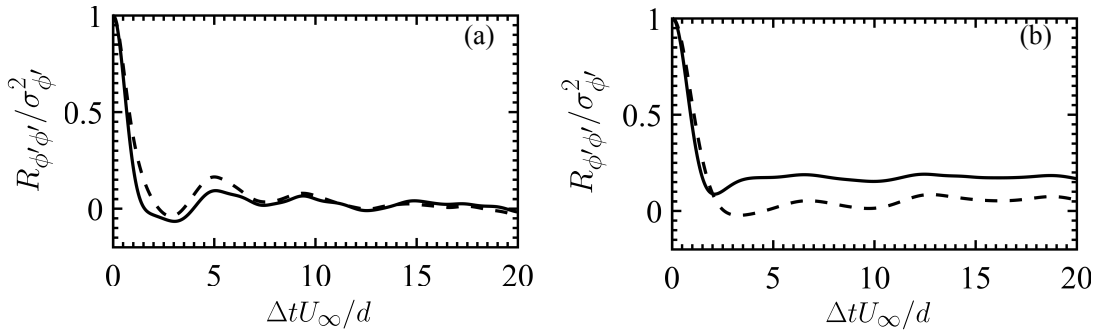

Figure 3.8: Temporal auto-correlation of (—) drag and (- - -) lift fluctuations for (a) gravel and (b) sand case plotted as a function of separation in time. Only small fraction of the signal in which non-negligible correlation exists is plotted.

values of local minima are typically $3-4$ times smaller than the ones reported by Chan-Braun & Uhlmann (2013). It should be noted that the unidirectional flow study reported by Chan-Braun & Uhlmann (2013) falls under hydrodynamically smooth and transitional regime, whereas Reynolds numbers in present cases are dramatically higher and fall under very rough turbulent regime.

Using temporal auto-correlation function, two different time scales, integral (t_l) and Taylor micro-scale (t_λ) for drag and lift fluctuations are calculated. The integral time scale, defined as the integral of the auto-correlation, is computed in the integration domain within which value of auto-correlation function monotonically decreases and goes to zero (here, $\Delta t U_\infty/d \in [0, 15]$). The short-time behavior of the auto-correlation function can be quantified using Taylor micro-scale (t_λ), defined by the zero-crossing of the parabola osculating the correlation function at zero separation.

Table 3.3 tabulates integral time scales and temporal Taylor micro-scales of drag/lift fluctuations for the gravel and the sand case and the following observations could be noted comparing both flow cases: (i) integral time scales of force fluctuations for the gravel are typically smaller than that for the sand particle when scaled in outer units. This could be attributed to the different nature of the

Case	Outer	F'_D	F'_L	Inner	F'_D	F'_L
Gravel	$t_l U_\infty/d$	0.97	1.49	$t_l u_\tau^2/\nu$	48.8	75.1
Sand	$t_l U_\infty/d$	8.44	3.32	$t_l u_\tau^2/\nu$	92.7	36.4
Gravel	$t_\lambda U_\infty/d$	0.86	0.91	$t_\lambda u_\tau^2/\nu$	44.9	46.7
Sand	$t_\lambda U_\infty/d$	1.18	1.38	$t_\lambda u_\tau^2/\nu$	13	14.6

Table 3.3: Integral time scale (t_l) and temporal Taylor micro-scale (t_λ) of drag and lift fluctuations for gravel and sand case. Time scales are non-dimensionalized using inner units ($\nu/u_{\tau,max}^2$) and outer units (d/U_∞).

near-bed turbulence in both flow cases. The broken streamwise structures of the time scale $\sim d/U_\infty$ in the gravel case are responsible for inducing drag/lift fluctuations on the gravel particle, resulting in integral time scales almost close to unity when scaled in outer units. On the contrary, presence of elongated streamwise structures of the size several particle diameters results in larger values of integral time scales of force fluctuations in the sand case. (ii) As a result of significant flow isotropization, Taylor micro-scales of drag/lift fluctuations for gravel particle are almost comparable to their integral time scales, suggesting the absence of large separation of scales. In the case of sand, small scale drag/lift fluctuations are dominated by small scale turbulent motions of the time scale $\sim d/U_\infty$, typically resulting in Taylor micro-scales of the order of unity when scaled in outer units. (iii) As a result of large effective roughness Reynolds number (k_s^+) in the gravel case, time scales of force fluctuations for the gravel particle are typically $2-3$ times larger than that for the sand when scaled in inner units. In general, these results indicate that the small diameter sand-bed typically exhibits force fluctuations of the longer duration as that compared to the gravel-bed under investigation.

To further understand the behavior of particle-bed forces, temporal cross-correlation function of drag and lift fluctuations is computed. This would help to investigate if drag and lift fluctuations are correlated in time and get affected by similar near-bed flow structures. Phase-averaged cross-correlation is calculated

by setting $\phi' = F'_D$, $\psi' = F'_L$ and $\Delta x = \Delta y = 0$ in Eq. 3.1 and is plotted in Fig. 3.9. For no shift in time ($\Delta t = 0$), the cross-correlation is very small and the drag and lift fluctuations are weakly correlated. The cross-correlation reaches maximum value 0.45 (0.48) for separation in time $\Delta t U_\infty/d = 0.86$ (1.08) for gravel (sand) case, indicating that the drag and lift fluctuations, on an average, are positively correlated with each other. This suggests that the positive fluctuation in the drag (result of stagnation pressure) corresponds to the simultaneous positive fluctuation in the lift (result of streamline contraction). It is also interesting to note that the time-lag of maximum value of correlation function approximately matches Taylor micro-scale of drag and lift fluctuations (cf. Table 3.3). Furthermore, as shown in Fig. 3.9, the cross-correlation takes the minimum value -0.39 (-0.45) for separation in time $\Delta t U_\infty/d = -0.73$ (-0.98) for gravel (sand) case. For larger negative separation times, the correlation function for sand increases from minimum value to reach zero, whereas, correlation for gravel again becomes positive before going to zero. In comparison to previous unidirectional flow studies (Hofland, 2005; Dwivedi, 2010; Chan-Braun & Uhlmann, 2013; Amir *et al.*, 2014), there exist significant differences in the present case in terms of flow conditions, particle Reynolds number, particle shape and arrangement, methodologies for the flow data measurements, etc; however, it is promising to see that the overall behavior of the cross-correlation function, i.e. local maximum (minimum) for positive (negative) separation remains identical. Also, the maximum values of the cross-correlation function between 0.12 to 0.55 were reported in these studies and interestingly, present values for gravel and sand case also fall well within this range. Such behavior of the cross-correlation of drag and lift fluctuations seems to be very robust and is conjectured to be the effect of a strong influence of the pressure field on the particle-bed forces. This interpretation is in favor of a model approach proposed by Hofland (2005) based on a convected frozen pressure field.

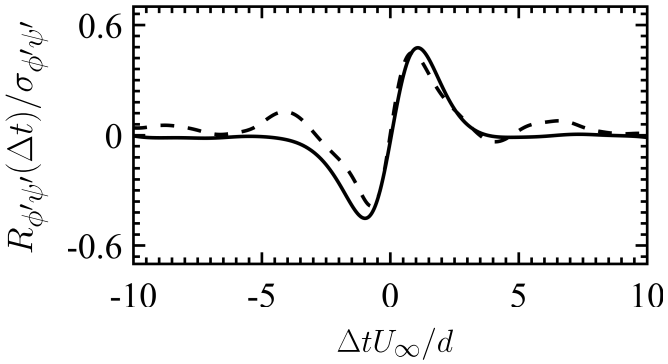

Figure 3.9: Temporal cross-correlation of drag and lift fluctuations plotted as a function of separation in time for the gravel (- - -) and the sand (—) case. Only small fraction of the signal in which non-negligible correlation exists is plotted.

3.3.5 *Spectra*

To understand the spectral content of drag and lift fluctuations, their frequency spectra $\widehat{R}_{\phi'\phi'}(f)$ are investigated. Due to the finite nature of the signal, modified periodogram method of Welch (1967) with 50% overlap and applying a Hamming window to the original signal is employed. Here, spectra are averaged for all the particles and flow cycles and are normalized by integral of spectra over all the frequencies. Figure 3.10 shows normalized spectra of drag (solid line) and lift (dashed line) fluctuations for (a) gravel and (b) sand case. It can be seen that in both gravel and sand case, a reasonably good collapse of spectra for drag and lift fluctuations is observed, with the largest spectral contributions at lower frequencies. Also, all spectra display roughly two scaling regions, $-11/3$ and $-7/3$ in the mid- and high-frequency regions, respectively. Earlier, George *et al.* (1984) performed spectral analysis of turbulent pressure fluctuations in a homogeneous constant mean-shear flow and reported the presence of $-11/3$ and $-7/3$ scaling in the pressure spectrum when turbulence–mean-shear and turbulence–turbulence interactions dominate, respectively. Interestingly, present data of oscillatory flow over rough-bed also reveal similar scaling for drag and lift fluctuations.

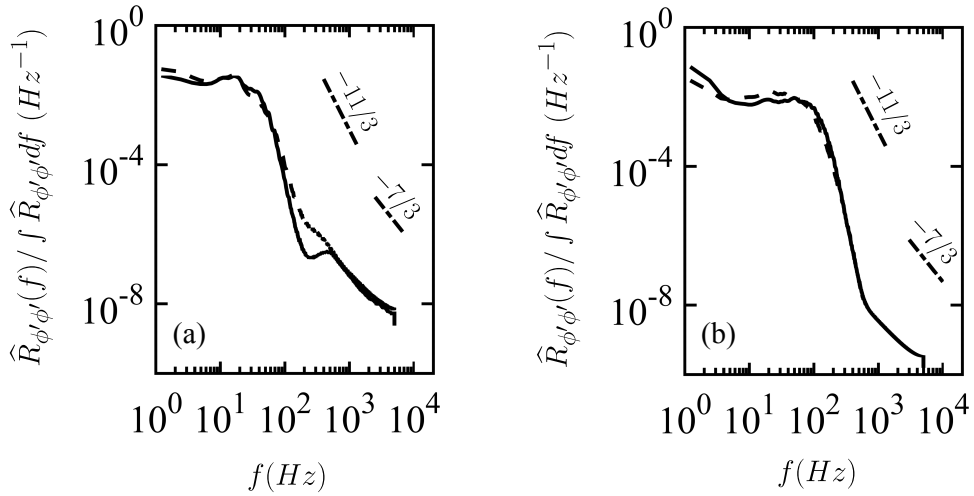

Figure 3.10: Spectra of drag (—) and lift (- - -) fluctuations for (a) gravel and (b) sand case.

In comparison to the gravel, $-11/3$ scaling region for the sand case extends little further up to higher frequencies ($\approx 600Hz$) suggesting wider range of scales are dominated by turbulence–mean-shear interactions. On the other hand, as a result of significant flow isotropization in the case of the gravel, it is possible that the turbulence–turbulence interactions play equally important role exhibiting $-7/3$ scaling for much higher frequencies ($\approx 100Hz$). Recently, Hofland (2005); Detert *et al.* (2010) in their unidirectional flow studies showed that the turbulent wall pressure spectra exhibit $-7/3$ scaling, whereas Amir *et al.* (2014) reported the presence of $-11/3$ scaling region. Contrary to these laboratory studies where only pressure spectra were analyzed, present results provide spectral energy content of total drag and lift fluctuations. Nevertheless, it is interesting to see that the present data for the gravel and the sand case typically exhibit similar behavior as that observed in unidirectional studies, and therefore indicating universal nature of the force fluctuations on the roughness-bed.

3.3.6 *Particle forces and turbulent flow-field correlations*

The aim of this investigation is to shed light on the role of near-bed flow features that are responsible for inducing unsteady fluctuating forces on the particle-bed. As noted earlier, computations or measurements of drag and lift forces on the particle-bed are not straightforward. Instead, they are calculated indirectly by assuming a cross-correlation with near-bed velocity fluctuations. In this context, two questions arise as to what is the distribution of the near-bed velocity and to what spatial extent it is cross-correlated with unsteady forces on the particle-bed. To answer the former, Ghodke *et al.* (2014*a*,*b*) showed the probability-density function (PDF) of the near-bed velocity and pressure fluctuations in the region above the particle to be non-Gaussian and follow fourth-order Gram-Charlier distribution model given by,

$$f_{GC4}(\psi') = \frac{\exp(-\psi'^2/2)}{\sqrt{2\pi}}\left[1 + \frac{S_{\psi'}}{3!}(\psi'^3 - 3\psi') + \frac{K_{\psi'} - 3}{4!}(\psi'^4 - 6\psi'^2 + 3)\right], \quad (3.2)$$

where ψ' is the normalized fluctuating flow variable, $S_{\psi'}$ and $K_{\psi'}$ are skewness and kurtosis of its distribution, respectively. To answer the latter, evaluation of the spatial extent of the cross-correlation between forces on the particle-bed and the streamwise velocity and pressure fluctuations is carried out in a similar manner as done by Chan-Braun & Uhlmann (2013) for unidirectional steady flow. To this end, three-dimensional correlation function given by Eq. 3.1 is computed by taking ϕ' as the force-field of the fluctuating drag/lift and ψ' as the flow variable fluctuations. Note that, the local three-dimensional force-field on a particle is considered for the calculations. As per Eq. 3.1, the correlation function $R_{\phi'\psi'}$ is averaged for all the particles and around 15 flow cycles in each case. Here, $R_{\phi'\psi'}$ is normalized by using maximum friction velocity $u_{\tau,max}$ and $\rho u^2_{\tau,max}$ as characteristic scales for velocity and pressure fluctuations, respectively and by using standard deviation of the respective force fluctuations. As a result, the correlation is not bounded by unity. The maximum and minimum values of the correlations, $R_{\phi'\psi'}$,

Correlation	Gravel	Sand
	max (min)	max (min)
$(F'_D,\, u')$	1.13 (-1.39)	2.03 (-0.63)
$(F'_L,\, p')$	1.33 (-12.42)	1.93 (-11.61)

Table 3.4: Maximum (minimum) amplitude of the correlation between particle force and the flow field, $R_{\phi'\psi'}$, in the case of the gravel and the sand particle at the peak phase. Here, $R_{\phi'\psi'}$ is normalized by using maximum friction velocity $u_{\tau,max}$ and $\rho u^2_{\tau,max}$ as characteristic scales for velocity and pressure fluctuations, respectively and by using standard deviation of the respective force fluctuations.

are given in Table 3.4.

In the following, cross-correlations of drag with velocity fluctuations (F'_D–u') and lift with pressure fluctuations (F'_L–p') at the peak phase are presented. This choice is based on the following considerations. In the given setup of closely-packed bed, lift is expected to be strongly dependent on the near-bed pressure distribution. Also, for a smaller size sand particles viscous force (which is mainly related to streamwise velocity) is predominant contributor in the drag over the pressure. In this context, drag (lift) is cross-correlated with velocity (pressure) fluctuations. Take a note that, drag and lift fluctuations, on an average, are positively correlated with a time-lag (cf. Fig. 3.9) and therefore, given correlation fields should suffice for complete description of the flow field at the peak phase.

Figure 3.11 shows iso-contours of correlation function of drag and velocity fluctuations for gravel (a,b) and sand (c,d) particles plotted at a peak phase. Planes at zero spanwise shift ($\Delta y = 0$) and zero streamwise shift ($\Delta x = 0$) are shown in Fig. 3.11 (a,c) and (b,d), respectively. Close-up view of the domain where significant correlations exists is presented. As shown in Fig. 3.11 (a), drag is positively correlated with velocity fluctuations at around one diameter distance upstream and downstream from the gravel particle. Spanwise view shown in Fig. 3.11 (b) reveals the presence of "wing-shaped" positive correlation between drag and velocity fluc-

tuations. As shown in Fig. 3.11 (c,d), similar shape of the correlation is observed in the case of sand particle. However, in comparison to gravel, the spatial extent of the correlation is typically $2-3$ times larger in both streamwise and spanwise directions for the sand particle. As discussed earlier, this could be attributed to the presence of longer near-bed flow structures found in the case of sand-bed. On the contrary, as a result of significant flow isotropization in the gravel case, only local flow structures around the particle are responsible for inducing hydrodynamic forces on the particle. Also, take a note that, in comparison to the sand case, "wing-shaped" correlation in the gravel case appears to be more inclined to the x-axis, a consequence of energized wall-normal motions as discussed in (Ghodke & Apte, 2016). Such "wing-shaped" correlations were clearly absent in the case of square arrangement of particles studied by Chan-Braun & Uhlmann (2013). This is attributed to the complex shielding effects due to hexagonal packing of the bed that result in disruption of the typical pattern of high-speed/low-speed streaks found in the square arrangement of the particles.

As seen in Fig. 3.11 (a,b), there exists a region of negative correlation between drag and velocity fluctuations just above the crest of the gravel particle, however, in the case of sand-bed the correlation is positive at this location as shown in Fig. 3.11 (c). It is conjectured that such region of negative correlation in the gravel case is an artifact of local near-bed flow deceleration before the end of the peak phase and is typically less predominant in the high Reynolds number sand case, a behavior also evident from phase-lag between particle forces and outer flow as discussed in § 3.3.2. These effects are attributed to the oscillatory nature of the flow and were not seen in unidirectional flow study (Chan-Braun & Uhlmann, 2013).

Figure 3.12 presents iso-contours of correlation function of lift and pressure fluctuations for gravel (a,b) and sand (c,d) case plotted at a peak phase. Overall shape of the correlation is similar for gravel and sand particles. In both the cases, negative correlation between lift and pressure fluctuations is observed in the region above the particle crest, indicating negative fluctuation in the pressure results in

positive fluctuation in the lift. This region extends up to $1D$ distance upstream and downstream in the streamwise direction from the gravel and the sand particle center as shown in Fig. 3.12 (a,c). Similar to Fig. 3.11 (b,d), the presence of "wing-shaped" positive correlation between lift and pressure fluctuations for both gravel and sand case is clearly evident in Fig. 3.12 (b,d). Again, the overall shape of this correlation is comparable for the gravel and sand particle, although little wider for the latter as shown in Fig. 3.12 (d).

In summary, presence of such regions of significant correlations between forces on particles and turbulent flow field around them further provides the evidence of the direct link between near-bed flow structures and unsteady hydrodynamic forces on the roughness-bed.

3.3.7 *Particle force distributions*

In order to further explore the possibility of influencing probabilistic models for sediment incipient motion, it would be of interest to analyze the PDF of near-bed flow parameters and relate it with the hydrodynamic forces on the particles. Given the high correlation of particle forces with the near-bed flow parameters, it is expected that they follow similar distribution as that of the velocity and pressure fluctuations. In that case, statistics of forces on the particle-bed could be obtained by using the information of measurable near-bed flow variables.

To this end, PDFs of drag and lift fluctuations are constructed for the gravel and the sand case. Also, pressure and velocity data are collected in the regions of high correlations as shown in Fig. 3.11 and Fig. 3.12 and their higher-order moments such as skewness and kurtosis are used to build a fourth-order Gram-Charlier distribution given by Eq. 3.2. Figure 3.13 show PDFs of (a,c) drag and (b,d) lift fluctuations represented by histograms for the (a,b) gravel and (c,d) sand case plotted at a peak phase. PDFs of (a,c) velocity and (b,d) pressure fluctuations constructed by using fourth-order Gram-Charlier distribution are also plotted (solid line). In both the cases, PDFs of drag (lift) fluctuations, in particular, peaked-ness and long tails match remarkably well with fourth-order Gram-Charlier

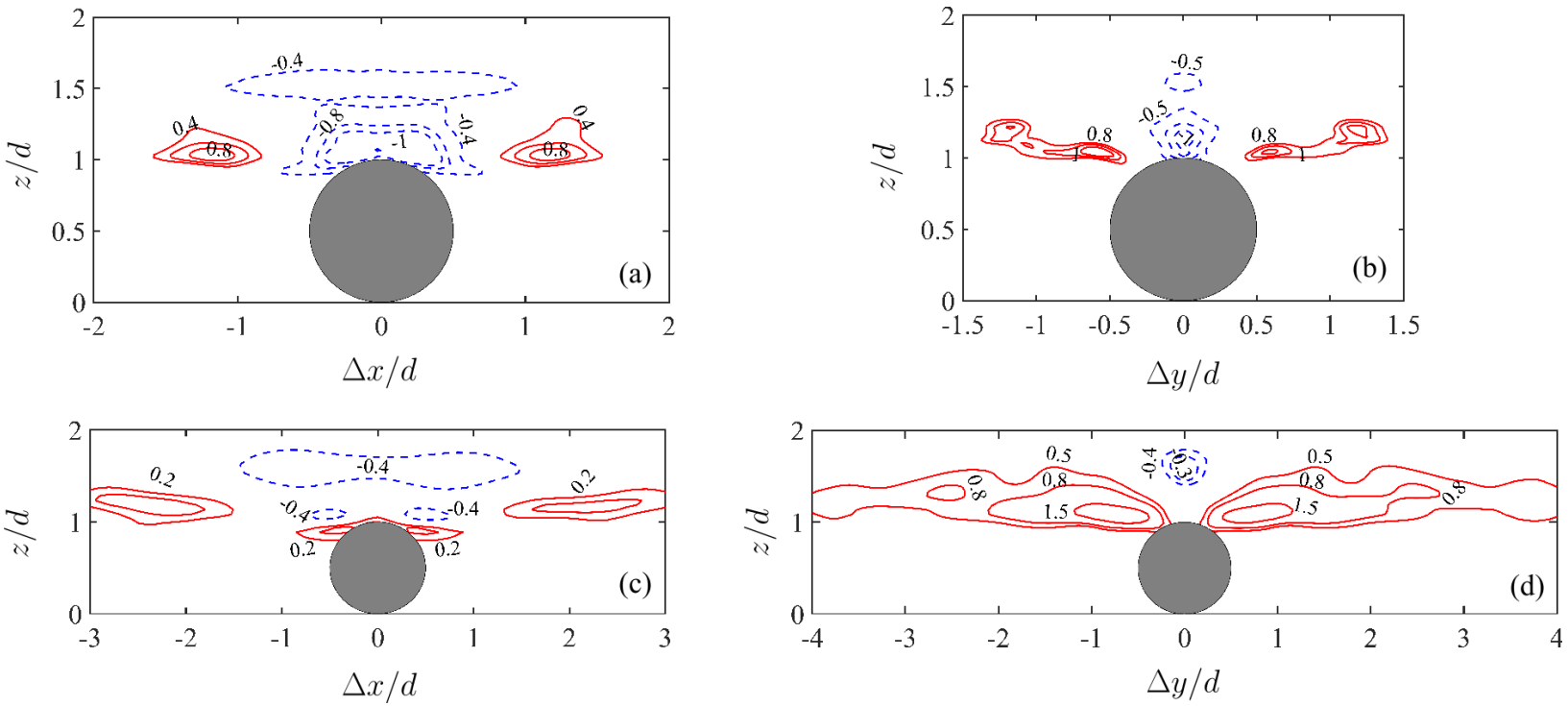

Figure 3.11: Close-up view of iso-contours of correlation function $R_{\phi'\psi'}$ of drag (F'_D) and streamwise velocity (u') fluctuations for gravel (a,b) and sand (c,d) particles plotted at a peak phase. Panels (a,c) show planes at zero spanwise shift ($\Delta y = 0$) and (b,d) show planes at zero streamwise shift ($\Delta x = 0$). Here, correlation is normalized by $u_{\tau,max}$ and standard deviation of drag fluctuations $\sigma_{F'_D}$ at a peak phase. Solid (dashed) lines indicate positive (negative) correlation.

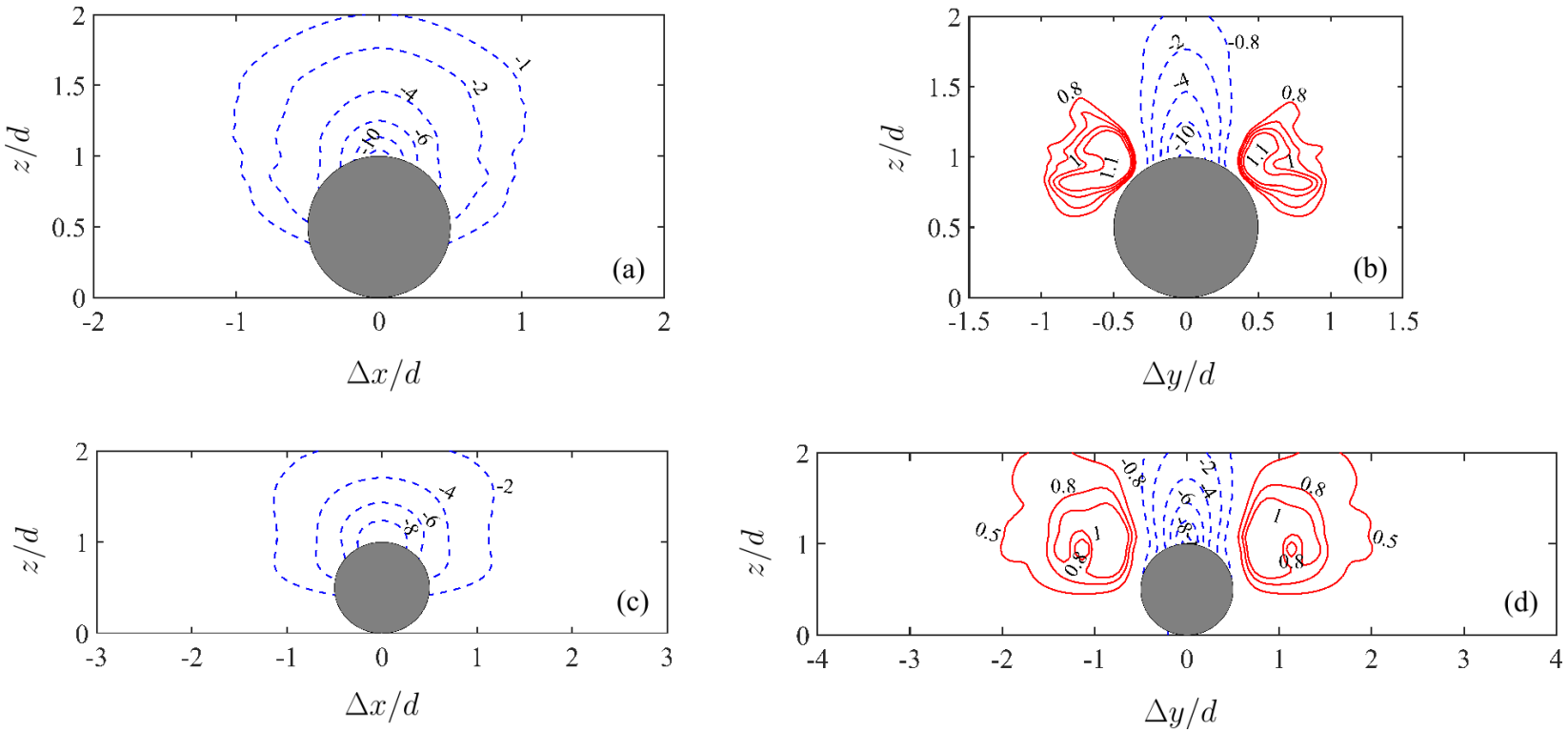

Figure 3.12: Close-up view of iso-contours of correlation function $R_{\phi'\psi'}$ of lift (F_L') and pressure (p') fluctuations for gravel (a,b) and sand (c,d) particles plotted at a peak phase. Panels (a,c) show planes at zero spanwise shift ($\Delta y = 0$) and (b,d) show planes at zero streamwise shift ($\Delta x = 0$). Here, correlation is normalized by $\rho u_{\tau,max}^2$ and standard deviation of lift fluctuations $\sigma_{F_L'}$ at a peak phase. Solid (dashed) lines indicate positive (negative) correlation.

distributions of velocity (pressure) fluctuations. These findings imply that the distribution of hydrodynamic forces on the particle-bed is influenced by near-bed flow structures and can be constructed through higher-order flow statistics, further re-emphasizing the need of incorporating the effects of near-bed bursting phenomena into probabilistic models for onset of erosion.

3.3.8 *Concept of impulse*

Diplas and co-workers (Diplas *et al.*, 2008; Valyrakis *et al.*, 2010; Celik *et al.*, 2010, 2013, 2014) introduced the concept of impulse indicating the importance of both magnitude and duration of fluctuating hydrodynamic forces on sediment erosion. Although such approach hold promise in accounting for the intermittent dynamics of turbulent flows, there are certain difficulties in describing such a criterion. For example, detecting the peak events to calculate impulse from the time signal of a force history requires *a priori* specification of a threshold/critical value of the force. It is difficult, however, to determine the correct choice of such a threshold that is best suited to predict the incipient motion. Present investigation deals with fixed particle-bed and it is not possible to detect the peak events resulting in particle erosion. Nevertheless, to shed some light on the topic, statistical analyses to provide brief description of intermittency in fluctuating forces by means of counts and duration of peak events, impulse magnitude and their PDFs for a range of threshold conditions are provided. Such characterization of force intermittency might serve as a useful tool in making reasonable choice of a threshold criterion.

Consider a sample time history of the drag force (F_D) on a gravel particle as shown in Fig. 3.14. In this case although period-averaged drag force (dashed line) on the particle is less than the specified threshold (dash-dot line), the instantaneous force exceeding the threshold for a long duration could still possibly result in particle dislodgement (Diplas *et al.*, 2008). As shown in Fig. 3.14, such extreme force events are identified when the instantaneous force value exceeds the threshold and duration of such events (t_{I_1}, t_{I_2}, t_{I_3}, etc) are also computed. Based on this, impulse on a particle for a given duration is calculated using

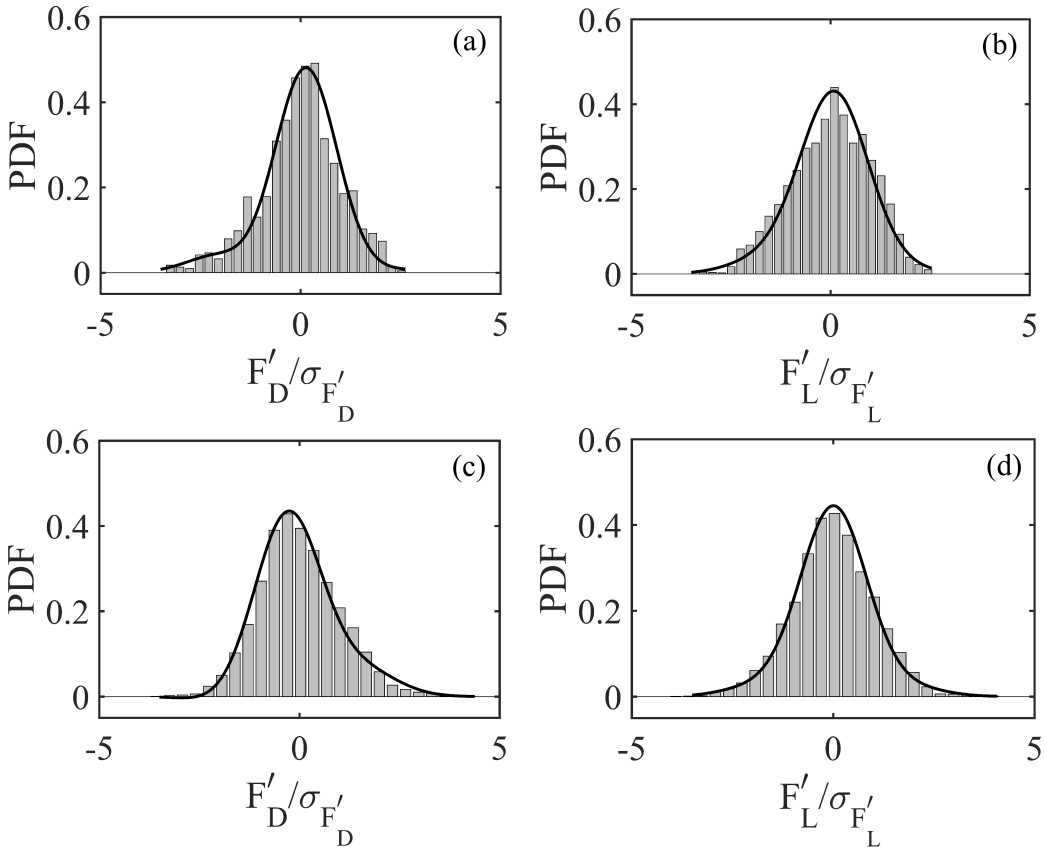

Figure 3.13: PDF normalized by standard deviations at a peak phase: (a,c) drag (velocity) fluctuations and (b,d) lift (pressure) fluctuations represented by histograms (solid line). Panels (a,b) and (c,d) are for gravel and sand, respectively. PDFs of velocity and pressure fluctuations (solid line) are constructed by using forth-order Gram-Charlier distribution (Eq. 3.2).

$$Impulse = I\ (\phi > \phi_{thr}) = \int_{t_I} \phi\ dt, \tag{3.3}$$

where ϕ_{thr} is the specified threshold value of the variable ϕ. Implementing this procedure for gravel- and the sand-bed, number of such peak force events, their duration and impulse magnitude are calculated for various threshold conditions ($0 \leq \phi_{thr}/\sigma_\phi \leq 5$). Subsequently, averaging is carried out for number of particles and flow cycles. Note that, change in the sign of the drag force after flow reversal is taken into consideration while identifying peak force events.

Figure 3.15 (a) and (b) show average number of intervals, N_I, of peak force events per flow cycle for the gravel and the sand particle, respectively. In both flow cases, number of intervals for the lift force are typically larger than that for the drag force, indicating higher intermittency in the lift. In the case of gravel-bed, number of intervals N_I initially increase (more rapidly for the lift) with increase in the threshold, indicating the presence of relatively low-magnitude and high-frequency local peaks. Note that, these local peaks are otherwise counted as a single peak for small threshold values under present peak-detection scheme as represented in Fig. 3.14. With further increase in the threshold value, N_I for drag and lift begins to decline gradually isolating extreme force events. As shown in Fig. 3.15 (a), peak value N_I for the lift is almost two times higher than that for the drag. Therefore, in comparison to the drag, number high-frequency peak events is typically more in the case of lift. Moreover, peak in the magnitude of N_I for drag (lift) is seen at $\phi_{thr}/\sigma_\phi \approx 1(2)$. This further shows that, on an average, extreme events in the lift force for the gravel particle also have higher magnitudes as that compared to those in the drag.

In the case of sand-bed, this behavior is more intricate. Consistent with the gravel case, N_I for the lift in the sand case initially increases rapidly with increase in the threshold indicating the presence of low-magnitude local peaks; however, N_I for the drag decreases slowly exhibiting a local maximum close to $\phi_{thr}/\sigma_\phi \approx 0.6$. Based on the Fig. 3.15 (b), two observations for the sand case can be drawn as

follows. First, similar to the gravel case, peak in the N_I for the lift is almost $1.5 - 2$ times higher than that for the drag. And second, both the peaks are observed at around same threshold value ($\phi_{thr}/\sigma_\phi \approx 0.6$). Former suggests that the lift data consists of more number of high-frequency peak events than those found in the drag, whereas latter indicates that the peaks in the lift and drag force have comparable magnitudes.

Furthermore, all the profiles for N_I in both gravel and sand case exhibit a recognizable change in the slope after which the drop in the value of N_I is more gradual (e.g. after $\phi_{thr}/\sigma_\phi \approx 1$ in the sand case). Such flattening of profiles can be interpreted as the presence of well pronounced isolated peaks in the drag and lift forces on the particle-bed.

Figure 3.16 (a) and (b) respectively show variation of average duration, t_I, of peak force events per flow cycle for the gravel and the sand particle. In the case of gravel-bed, time duration of lift is typically $1.5 - 2$ times higher that of the drag force. This corroborates Fig. 3.15 (a) and (b) suggesting the presence of more number of high-frequency peak events in the lift that results in larger time duration as that compared to drag, albeit for the sand particle this difference in drag and lift duration is indeed smaller. In both gravel and sand case, average time duration decreases with increase in the threshold value. Also, take a note of sudden change in the slope of the profiles shown in Fig. 3.16 (a) and (b). As the threshold value increases, it is evident that the change in the t_I is more gradual. This further provides the evidence of presence of pronounced isolated peaks in drag and lift forces.

Based on this, an average impulse on a particle per flow cycle is calculated using Eq. 3.3 and is plotted in Fig. 3.17 (a) and (b) for the gravel and the sand case, respectively. Consistent with the earlier observations, impulse based on the lift force is higher than that based on the drag. With increase in the threshold, impulse related to the lift for gravel (sand) particle is seen to decrease, however that of the drag almost stays constant up to the threshold value of 1 (0.7). It is possible that impulse is dominated by few local events that get detected until this

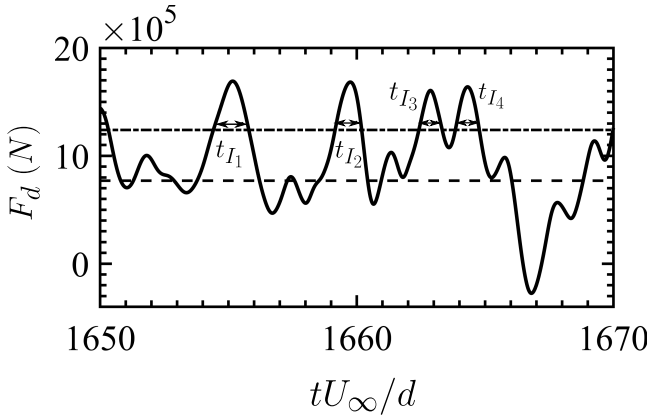

Figure 3.14: Representative time history (—) of the drag force (F_D) on a gravel particle. Period-averaged drag force (- - -) along with the specified threshold, $\phi_{thr}/\sigma_\phi = 1$ (···) are also indicated. Local peaks in F_D exceeding the threshold are detected as shown. The widths of the local peaks indicate their duration t_I.

threshold value. Again, the profiles of average impulse show very gradual decrease for high threshold values. For the illustration purpose, the distribution of impulse events at a threshold value $\phi_{thr}/\sigma_\phi = 1$ is plotted in Fig. 3.18 for (a) gravel and (b) sand particle. All distributions are heavily and positively skewed and are well described by General extreme value distribution.

Based on these results, it is reasonable to suggest that using a threshold value $\phi_{thr}/\sigma_\phi > 1.5$ (2) for drag and lift in the case of gravel (sand) particle might be sufficient to identify well pronounced peak events. As noted earlier, present study considers the roughness-bed made up of fixed particles and therefore it is only conjectured that these events could possibly result in particle dislodgement, a subject of future investigation. Nevertheless, these results are typically in agreement with recently reported unidirectional studies (Chan-Braun, 2012; Celik *et al.*, 2014). For example, Celik *et al.* (2014) used threshold value based on the pressure, $\phi_{thr}/\sigma_\phi = 2$, for the D^+ values in between $330 - 440$. Distribution of impulse events reported by Celik *et al.* (2010, 2013, 2014) also showed highly skewed nature similar to that observed in Fig. 3.18.

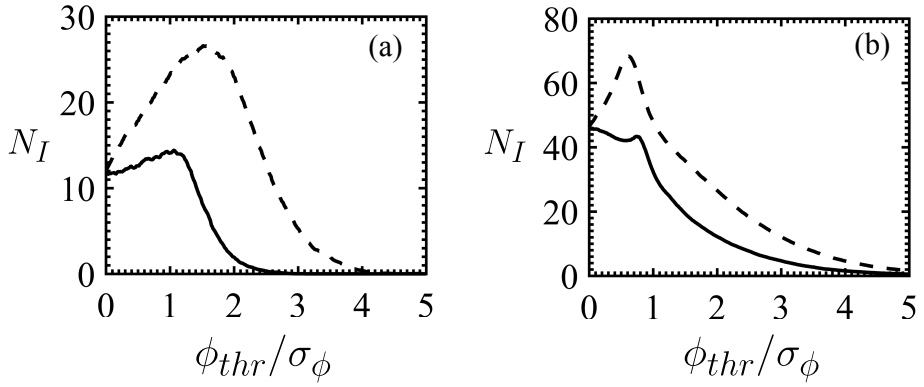

Figure 3.15: Variation with threshold values for (a) gravel and (b) sand, of average number of peak force events, N_I, experienced by a particle per flow cycle. The lines indicate drag (—) and lift (- - -).

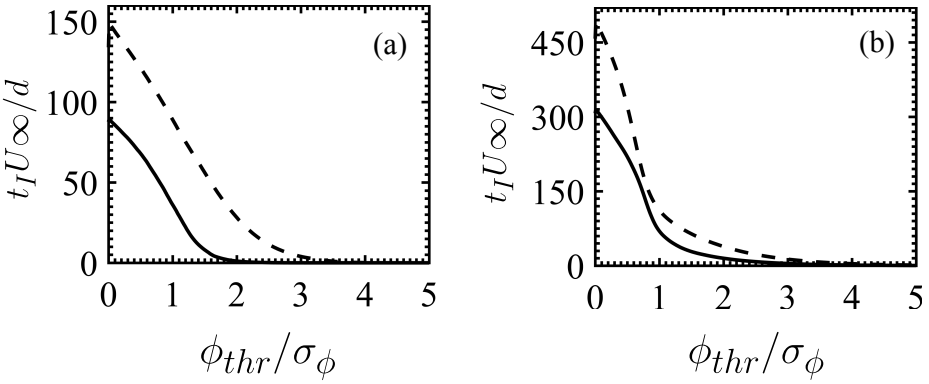

Figure 3.16: Variation with threshold values of average time duration of peak force events, $t_I U_\infty/d$, for a particle per flow cycle. Line styles and panels are same as in Fig. 3.15.

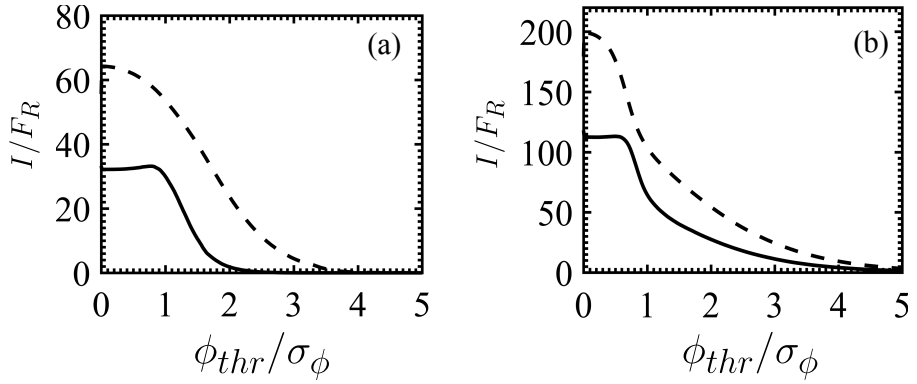

Figure 3.17: Variation with threshold values of average impulse, I, for a particle per flow cycle. Here, $F_R = \rho u_{\tau,max}^2 A_s U_\infty / d$, where A_s is the projected area of a single spherical particle given by $\pi d^2/4$. Line styles and panels are same as in Fig. 3.15.

3.3.9 *Summarizing implications of flow oscillations*

Oscillatory nature of the near-bed turbulence governs overall structure of hydrodynamic forces on the particle-bed. The near-bed flow depending on the Reynolds number is typically out of sync with the external pressure gradient, resulting in early deceleration of local flow in the vicinity of the particle-bed. Consequence of this, drag and lift record shows phase-delay with the free-stream velocity. Furthermore, contrary to unidirectional flows, turbulence is present only in some part of the oscillation cycle. In present investigation, especially for the sand case, sudden occurrence of turbulence followed by flow relaminarization is evident, former provides favorable conditions for dislodgement of the particles whereas latter typically offers stability to the particle-bed. Such behavior of near-bed flow also greatly influences spatial structure of the forces on the particles resulting in local patches of positive/negative forces. As a result, strong non-Gaussian behavior of both fluctuating near-bed flow and force statistics is observed in oscillatory flows.

On the other hand, although the overall structure of turbulent oscillatory flow differ significantly from that of unidirectional flow, there are some similarities

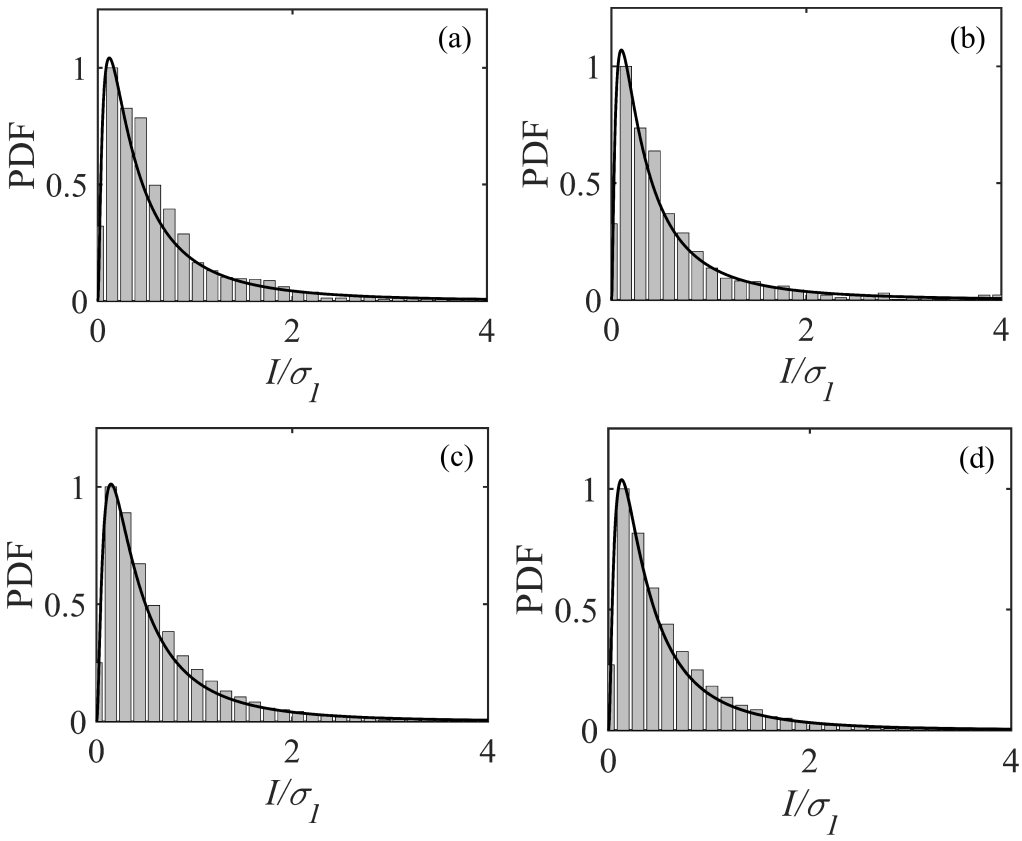

Figure 3.18: Distribution of impulse normalized by standard deviations at a threshold $\phi_{thr}/\sigma_\phi = 1$ for (a,c) drag force and (b,d) lift force represented by histograms. Panels (a,b) and (c,d) are for gravel and sand, respectively. Solid line represents General extreme value distribution.

in the characteristics of drag/lift forces that appear to be robust. For example, cross-correlation of drag and lift depicts qualitatively similar variation as that observed in other unidirectional studies, albeit with differences in the amplitudes of maxima and minima. In addition, scaling regions observed in force spectra as well as distribution of impulse events suggest universal nature of force fluctuations on the particle-bed.

3.4 Conclusions

Present investigation focused on studying spatial and temporal structure of unsteady hydrodynamic forces on the particle-bed subjected to oscillatory flow environment. Two particle sizes of diameter 375 (125) in wall units corresponding to gravel (sand) particle in a very rough turbulent flow regime are studied. Characterization of unsteady drag and lift forces in terms of spatial distribution, temporal auto-correlation, force spectrum as well as cross-correlations with measurable flow variables were carried out. The implications of selecting a certain threshold criterion for erosion onset based on the intermittency in the unsteady forces were also reported.

Time history of phase-averaged drag and lift force showed discernible differences between the gravel and the sand case. In the case of gravel, both drag and lift coefficients peak earlier in the flow cycle exhibiting phase-lag with the free-stream velocity. Conversely, as a result of increased Reynolds number, Re_a, this phase-lag is considerably reduced in the case of sand particle. The small phase-lag between drag and lift typically observed for the gravel particle was also seen to decrease in the case of sand. Moreover, presence of sharp spikes in drag and lift records were detected for the sand particle but were absent in the gravel case. Such distinct spikes were attributed to the sudden occurrence of turbulence close to the peak phase in the sand case.

In both gravel and sand case, the period-averaged lift and drag coefficients remained positive. The higher-order moments such as skewness and kurtosis of drag and lift fluctuations were found to exhibit strong non-Gaussian behavior. For

both flow cases, skewness values of drag and lift fluctuations were positive. High values of kurtosis indicated large intermittency in the forces that resulted in longer tails of rare but strong events. Also, kurtosis values in the sand case were almost two times larger than that in the gravel case, indicating larger intermittency in the forces for the former case.

Spatial distribution of the forces revealed region of strong positive drag near the top of the sphere, along with small patches of weak positive drag in the front and the aft portion of the particle; latter only present in the case of gravel-bed. Lift force of positive magnitude was observed mostly in the top portion of the upper hemisphere of the sand particle, a result of lower values of pressure due to flow acceleration near the particle crest. In the case of gravel-bed, positive lift force was mostly distributed on the side and the aft region of the particle. This was found to be the effect of enhanced three-dimensionality of the boundary layer and shielding effects along with the complex pore-scale flow in the gaps between the particles, all typically more pronounced in the case of large diameter gravel particle.

The time scales of drag and lift fluctuations were studied by means of temporal auto-correlation functions. The broken near-bed structures of the size comparable to the gravel resulting from flow isotropization governed the time scales of fluctuating forces on the gravel-bed. As a result, integral and Taylor micro-scales of drag and lift fluctuations on the gravel particle were of the order unity when scaled in outer units. Conversely, as a result of large Reynolds number (Re_a) and small size of particles, streamwise structures were more energetic and longer in length in the case of sand particle. This resulted in larger separation of scales causing disparity in integral and Taylor micro-scales in the case of sand-bed, former typically $4 - 8$ times larger than latter when scaled in outer units.

Cross-correlations between drag and lift were also studied. In both gravel and sand case, drag and lift, on an average, were positively correlated with a time-delay which was approximately equal to the Taylor micro-scale related to drag/lift fluctuations. Such behavior of the cross-correlation function appears to be very

robust as it is in general agreement with previously reported experimental studies that dealt with different flow conditions, particle Reynolds number, particle shape and arrangement, etc.

The spectral content of drag and lift fluctuations was examined by plotting their frequency spectra. In both gravel and sand case, a reasonably good collapse of spectra for drag and lift fluctuations was observed, with the largest spectral contributions at lower frequencies. Two scaling regions, $-11/3$ and $-7/3$ in the mid- and high-frequency regions, respectively were observed for all the spectra; former typically represents turbulence–mean-shear interactions, whereas latter indicates dominance of turbulence–turbulence interactions. In comparison to the gravel, $-11/3$ scaling region for the sand case was present up to higher frequencies suggesting wider range of scales were dominated by turbulence–mean-shear interactions. Again, present data for the gravel and the sand case exhibit similar behavior as that observed in previously reported unidirectional studies, and therefore indicates universal nature of the force fluctuations on the roughness-bed.

Three-dimensional cross-correlation function between drag (lift) and velocity (pressure) revealed the direct link between flow parameters and force fluctuations. Drag force was well correlated with the streamwise velocity fluctuations upstream and downstream of the particle center in the streamwise direction, along with the wing-shaped positive correlation in the spanwise direction for both flow cases. In comparison to the gravel case, the spatial extent of drag–velocity correlation was $2-3$ times larger in homogeneous directions for the sand particle, a feature that is reminiscent of longer near-bed structures typically found in the sand case. Additionally, negative drag–velocity correlation was observed just above the gravel crest and was argued to be an effect of local near-bed flow deceleration before the end of the peak phase. The pressure fluctuations were anti-correlated with the lift force in the regions around the gravel and the sand particle when plotted in the zero spanwise shift plane. The wing-shaped positive correlation in the spanwise direction was also observed for lift–pressure fluctuations in both gravel and sand case. In addition, PDF distributions of drag (lift) fluctuations, in particular, peaked-ness and

long tails matched remarkably well with fourth-order Gram-Charlier distributions of velocity (pressure) fluctuations.

Finally, characterization of impulse generating force events was carried out by studying the number and average duration of such events. In both flow cases, higher intermittency was found in the lift force as that compared to the drag. The magnitude of impulse showed gradual decrease for large threshold values, indicating the presence of isolated well pronounced peaks in the particle-bed forces. Distributions of impulse events for both flow cases were heavily and positively skewed and were well described by General extreme value distribution. Such statistical analyses of force intermittency is especially critical for better specification of a threshold value in erosion models.

Acknowledgments

This work is supported by the National Science Foundation (NSF-CBET - 1133363). The computations were performed on the Texas Advanced Computing Center's Stampede machine. Authors thank Dr. Javier Urzay of Stanford University for fruitful discussions during the CTR Summer Program 2014.

Chapter 4: Roughness effects on second-order turbulence statistics in oscillatory flows

Chaitanya D. Ghodke and Sourabh V. Apte

In preparation for submission

Abstract

Effects of roughness on the near-bed turbulence characteristics in oscillatory flows are studied by means of particle-resolved direct numerical simulations (DNS). Two particle sizes of diameter 375 and 125 in wall units corresponding to the large size gravel and the small size sand particle, respectively, in a very rough turbulent flow regime are reported. A double-averaging technique is employed to study the nature of the wake field, i.e., the spatial inhomogeneities at the roughness length scale. This introduced additional production and transport terms in double-averaged Reynolds stress budget, indicating alternate pathways of turbulent energy transfer mechanisms. Budgets of normal components of Reynolds stress reveal redistribution of energy from streamwise component to other two components and is attributed to the work of pressure in both flow cases. It is shown that the large diameter gravel particles significantly modulate the near-bed flow structures, leading to pronounced isotropization of the near-bed flow; while in the sand case, elongated horseshoe structures are found as a result of high shear rate. Effect of mean shear rate on the near-bed anisotropy is significant in the sand case, while it is minimal for the gravel-bed. Redistribution of energy in the gravel case showed reduced dependence on the flow oscillations, while for the sand particle it is more pronounced towards the end of an acceleration cycle.

4.1 Introduction

Interactions between rough surfaces and turbulent structures have been, and continue to be, a long standing topic subjected to rigorous investigation. Several pioneering studies identifying the effects of roughness elements on the near-bed turbulence have been reported so far (Raupach & Thom, 1981; Raupach *et al.*, 1991; Jiménez, 2004).

Presence of roughness can lead to a substantial modification of the underlying boundary layer, resulting in increased bed shear stress, reduction in the near-bed

anisotropy, modification of the near-bed sweep and ejection motions along with marked changes in turbulent energy transport mechanisms (Krogstad *et al.*, 1992; Krogstad & Antonia, 1994; Krogstad *et al.*, 2005; Ikeda & Durbin, 2007; Yuan & Piomelli, 2014*b*; Ghodke & Apte, 2016). Presence of roughness is also seen to provide alternate paths of energy transport as a result of spatial inhomogeneities in the flow arising from the local effects of the individual roughness elements. A double-averaging technique has been widely used, in particularly for vegetation canopies, to study such effects (Raupach & Thom, 1981; Raupach & Shaw, 1982; Finnigan, 2000; Nikora *et al.*, 2001) and has been recently extended to study unidirectional flows over sediment-bed (Mignot *et al.*, 2009; Dey & Das, 2012). As a result of spatial inhomogeneities in the wake of the roughness, total kinetic energy has an additional contribution known as "wake kinetic energy" (WKE), generated from the work of mean flow against the pressure drag of roughness elements (Raupach & Shaw, 1982). Double-averaging method has been proven to be a useful tool that potentially offers new insights into understanding such paths of energy transfer mechanisms; from mean kinetic energy (MKE) to turbulent kinetic energy (TKE), from MKE to WKE and subsequently the bi-directional exchange between TKE and WKE (Yuan & Piomelli, 2014*b*; Ghodke & Apte, 2016). In order to characterize modulation of the near-bed turbulence as it governs the nature of inner–outer layer interactions along with generation of the drag on the roughness elements, it is important to analyze energy transport mechanism in detail.

While many attempts to investigate such turbulence characteristics have been based on laboratory studies, obtaining some of the terms related to pressure and small-scale energy dissipation is extremely challenging. On the other hand, owing to the enormous computational cost in resolving individual roughness elements, performing detailed numerical investigations of these flows at high Reynolds numbers is still a challenge and very few numerical investigations studying spatial inhomogeneities have been reported so far (Coceal *et al.*, 2006; Yuan & Piomelli, 2014*b*). Furthermore, most of the aforementioned studies pertaining to this topic are reported for unidirectional, steady flows. However, detailed information of the

effects of roughness on the near-bed turbulence in oscillatory, non-stationary flows yet remain elusive.

As a first step towards fundamental understanding of such flows, detailed simulations studying effects of gravel-type roughness on the oscillatory turbulence have been recently reported in (Ghodke & Apte, 2016). Presence of roughness was shown to alter near-bed TKE transport mechanism, resulting in reduction of large-scale anisotropy. Supplementing (Ghodke & Apte, 2016), present investigation aims to study several other aspects of the interactions between rough-bed and oscillatory turbulence; in particular, effects of size of the roughness elements, redistribution of energy between normal components of Reynolds stress as well as budgets of WKE to understand the energy transfer between the wake and the turbulence, among others. To the best of authors' knowledge, such detailed characterization is the first of its kind and may have direct relevance to applications such as sediment transport in coastal flows. The outline of the paper is as follows: the computational setup and methodology are presented in § 2. In § 3, simulation results are presented followed by main conclusions in § 4.

4.2 Computational setup

In the present notation x, y and z, respectively, denote the streamwise, spanwise and vertical directions and u, v and w denote the velocity components in those directions. Viscous length of the problem is defined by Stokes-layer thickness $\delta = \sqrt{2\nu/\omega}$, where ν is the kinematic viscosity, $\omega = 2\pi/T$ is the oscillation frequency and T is the period of the wave. The rough-bed is made up of a single layer of hexagonal pack of fixed spherical particles that are touching each other. To study the effects of particle size on turbulence characteristics, two sizes of particle diameter normalized by the Stokes-layer thickness, $D = d/\delta$, corresponding to the large diameter gravel ($D = 6.95$) and the small diameter sand-type roughness ($D = 2.7$) are studied. Based on (cf. Fig. 2) from Ghodke & Apte (2016), both gravel and sand case correspond to very rough turbulent regime; latter approaching the limit of rough turbulent regime.

Case	D/δ	Re_δ	Re_a	Re_D	k_s^+	D^+	$f_{w,max}$	D/Δ_x	D/Δ_y	D/Δ_z	a/k_s	Regime
Gravel	6.95	400	80000	2780	745	375	0.036	50	75	300	14.4	rough turbulent
Sand	2.68	545	148500	950	250	125	0.015	15	20	100	50	rough turbulent

Table 4.1: Computational parameters and grid resolution details: $\mathrm{Re}_\delta = U_\infty \delta/\nu$ is the Reynolds number based on the Stokes-layer thickness, $\mathrm{Re}_a = U_\infty a/\nu$ is the Reynolds number based on the wave amplitude, $\mathrm{Re}_D = U_\infty D/\nu$ is the particle Reynolds number, $k_s^+ = u_{\tau,max} k_s/\nu$ is the effective roughness Reynolds number and $D^+ = u_{\tau,max} D/\nu$ is the particle size in wall units. Here, U_∞ is the amplitude of the free-stream velocity, $a = U_\infty/\omega$ is the amplitude of wave oscillation, $k_s \approx 2d$ is the Nikuradse roughness size and $u_{\tau,max}$ is the maximum friction velocity in a flow cycle. Maximum value of the wave friction factor, $f_{w,max} = 2\left(u_{\tau,max}/U_\infty\right)^2$ is also given. Details of calculation of friction velocity are given in Ghodke & Apte (2016). Present study assumes low Froude numbers.

The dimensionless parameters to characterize the flow along with grid resolution details are summarized in Table 4.1. As described in Ghodke & Apte (2016), uniform grids, although not cubic, are employed only in the region surrounding the particles and the grids are stretched in the flow normal direction above z = $8\delta(6\delta)$ for the gravel (sand) using hyperbolic tangent function. For both the cases, grid sizes in the streamwise and spanwise directions, on an average, are less than 8 and 6 wall units, respectively with $\Delta z^+ < 1$ in the near-bed region and were shown to be adequate to capture near-bed flow features (Ghodke & Apte, 2016). Moreover, the present grid resolutions in wall units are also comparable to the values used in existing DNS studies on rough-wall turbulent boundary layers (Coceal *et al.*, 2006; Ikeda & Durbin, 2007; Cardillo *et al.*, 2013; Yuan & Piomelli, 2015). Around 15 flow cycles per case are computed to obtain statistical convergence.

The computational domain similar to (Ghodke & Apte, 2016) consisting of a doubly periodic box in x- and y-directions is used. The flow domain is around $24\delta(28\delta)$ long in the flow direction, $14\delta(16\delta)$ wide in the spanwise direction and 45δ in the wall-normal direction for the gravel (sand) case. Vertical size of the domain is chosen such that all turbulent statistics decay to zero case at almost half the vertical height for large Reynolds number sand case under consideration.

The numerical solver based on fictitious domain algorithm (Apte & Finn, 2013), that facilitates solution of freely moving particles for a wide range of fluid-particle density ratios is used, although the particles are held fixed in the present study. The solver is fully validated for a range of test cases and the details of the algorithm as well as very detailed verification and validation studies have been published elsewhere (Apte *et al.*, 2008; Apte & Finn, 2013). In addition, current flow configuration for the gravel particle is validated against experimental data of Keiller & Sleath (1976) for $\mathrm{Re}_\delta = 95$ to show very good agreement as reported in Ghodke & Apte (2016). Other numerical predictions such as friction factor and boundary layer thickness for Reynolds numbers in the range $\mathrm{Re}_\delta = 95-400$ for the gravel-bed also show good comparison with experimental data, further confirming adequacy of the computational domain, grid resolution and rigid body treatment (Ghodke

& Apte, 2016).

4.3 Results and discussion

4.3.1 *Double averaging approach*

Following Raupach & Shaw (1982); Mignot *et al.* (2009), a double averaging procedure is employed for the analysis described below that decomposes a flow quantity, ϕ into double average $\langle\overline{\phi}\rangle$ (where, overbar and brackets respectively denote phase and homogeneous spatial averages), the spatial disturbance $\widetilde{\phi}$ (also known as the wake fluctuation) of the phase-average quantity and the turbulent fluctuation ϕ',

$$\phi(x, y, z, \omega t) = \langle\overline{\phi}\rangle(z, \omega t) + \widetilde{\phi}(x, y, z, \omega t) + \phi'(x, y, z, \omega t) \tag{4.1}$$

Note that, $\widetilde{\phi}$ is a measure of velocity scale of the wake field and is an artifact of spatial heterogeneity resulting from roughness elements. This term is otherwise absent in smooth wall flows. Such spatial disturbance in the velocity field results in additional stresses in the vicinity of the roughness elements given by, $\langle\widetilde{u_i}\widetilde{u_j}\rangle$ and are called form-induced or dispersive stresses.

4.3.2 *Near-bed flow structures*

To elucidate the turbulence modulation by roughness elements, instantaneous near-bed flow structures are visualized for the gravel and the sand particle case. As noted in Table 4.1, the amplitude based Reynolds number (Re_a) in the sand case is almost two times larger than that in the gravel case. On the other hand, effective roughness Reynolds number (k_s^+) in the gravel case is almost three times higher than that in the sand case. As a result, there exist some differences in the elementary processes that govern the near-bed turbulence structure in the gravel and the sand case. The large size of the gravel particle plays an important role in forming and then breaking the streamwise structures (Ghodke & Apte, 2016). On the other hand,

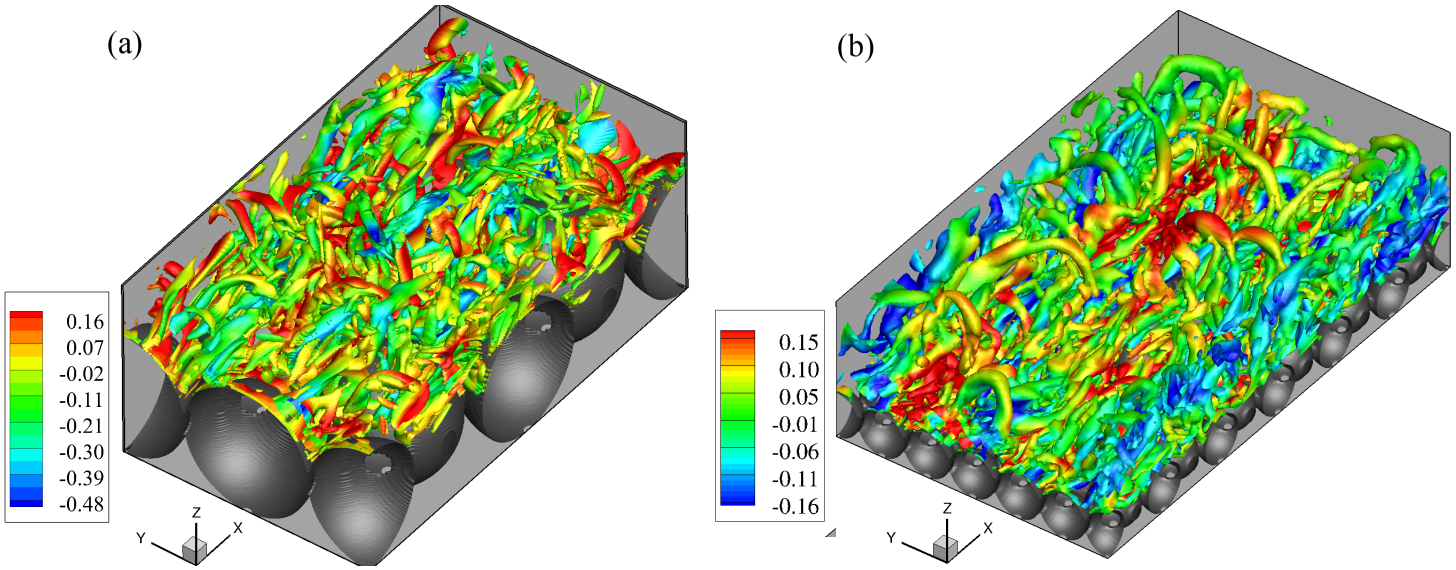

Figure 4.1: Close-up view of the instantaneous iso-surfaces of the λ_2-parameter colored by u'/U_∞ for (a) gravel and (b) sand case plotted at a peak phase, $\omega t = 5\pi/10$. The flow direction is the positive x-direction.

inertial effects play an important role in triggering the turbulence in small diameter sand case. This behavior is depicted in Fig. 4.1 that shows instantaneous near-bed flow structures in the form of λ_2-iso-surfaces (Jeong & Hussain, 1995) plotted at the peak phase for (a) gravel and (b) sand particle. For the gravel-bed, there exists a complex forest of highly densed near-bed structures that appear to be broken and are slightly inclined with respect to the horizontal direction. The disruption of these near-bed structures is attributed to the tendency of the gravel particles to energize the wall-normal velocity fluctuations that in turn distort the streamwise structures and cause flow isotropization, as already discussed in (Ghodke & Apte, 2016). As seen in Fig. 4.1 (b), the presence of larger horseshoe structures that span over more than few particle diameter in the flow direction is clearly evident in the sand case. Contrary to the gravel, these structures appear to be less broken, suggesting lower degree of near-bed flow isotropization in the sand case. Further quantification of flow isotropization for the gravel and the sand particle in terms of variation of Reynolds stresses along with their budgets and non-dimensional structure parameters will be discussed in the following sections.

4.3.3 *Reynolds and dispersive stresses*

Figure 4.2 shows profiles of double-averaged Reynolds stress normalized by $u^2_{\tau,max}$, plotted against wall-normal distance for (a,b,c) gravel and (d,e,f) sand case; where z_b is the zero-displacement plane (it is the effective level at which the bulk drag force is exerted on the roughness). Based on the variation of drag force in the wall-normal direction, the zero-displacement plane is located at $0.7D(0.85D)$ for the gravel (sand) particle. Profiles at three phases in a flow cycle, representing (a,d) acceleration, (b,e) peak and (c,f) deceleration phase are plotted.

In both flow cases, all components of Reynolds stress increase away from the effective bed location, peak close to the roughness crest level, and decay to zero in the outer region away from the roughness crest. In agreement to canonical wall-bounded flows, the streamwise component $\langle\overline{u'^2}\rangle$ increases away from the wall at much faster rate. Some discernible differences are observed in the near-bed

turbulence statistics between two flow cases. As shown in Fig. 4.2 (d,e,f), the peak value of $\langle\overline{u'^2}\rangle$ at all the phases in the sand case is significantly higher than $\langle\overline{v'^2}\rangle$ and $\langle\overline{w'^2}\rangle$. On the contrary, the disparity between peak values of $\langle\overline{u'^2}\rangle$, $\langle\overline{v'^2}\rangle$ and $\langle\overline{w'^2}\rangle$ is significantly smaller in the gravel case shown in Fig. 4.2 (a,b,c). This could be attributed to the effect of particle size and indicates the tendency of the gravel particle to redistribute more energy from streamwise to spanwise and wall-normal stresses, as also reported in Ghodke & Apte (2016). It is also worth noting that the fraction of energy redistributed from streamwise to other two components in the sand case shows some dependence on the flow oscillations, while for the gravel particle it remains almost identical as shown in Fig. 4.2 (a,b,c); quantitative measure of this characteristic will be presented later. As seen in Fig. 4.2 (a,b,c), all the components of Reynolds stress in the gravel case decay to zero at a distance $(z - z_b)/D \approx 1$ away from the effective bed level. Conversely, as a result of high Reynolds number (Re_a) and presence of larger wall-inclined horseshoe structures, Reynolds stresses decrease at much slower rate away from the crest and remain significant until $(z - z_b)/D \approx 2$ in the sand case.

Wall-normal profiles of the dispersive stresses, $\langle\widetilde{u}_i\widetilde{u}_j\rangle$, normalized by $u^2_{\tau,max}$ are plotted in Fig. 4.3 for (a,b,c) gravel and (d,e,f) sand case. Overall variation of the dispersive stresses is almost same as that of Reynolds stresses shown in Fig. 4.2. The region with non-negligible dispersive stress $\langle\widetilde{u}_i\widetilde{u}_j\rangle$, known as roughness sublayer, is smaller for the gravel as that compared to the sand particle with the thickness of approximately $0.5D$ and $2D$ above the zero-displacement plane in the former and the latter case, respectively.

4.3.4 *Budgets of Reynolds and dispersive stresses*

The total kinetic energy in the turbulent flow over roughness elements, $\frac{1}{2}\langle\overline{u_i u_i}\rangle$, may be decomposed into three parts as follows,

$$\frac{1}{2}\langle\overline{u_i u_i}\rangle = \frac{1}{2}\langle\overline{u_i}\rangle\langle\overline{u_i}\rangle + \frac{1}{2}\langle\widetilde{u}_i\widetilde{u}_i\rangle + \frac{1}{2}\langle\overline{u'_i u'_i}\rangle \tag{4.2}$$

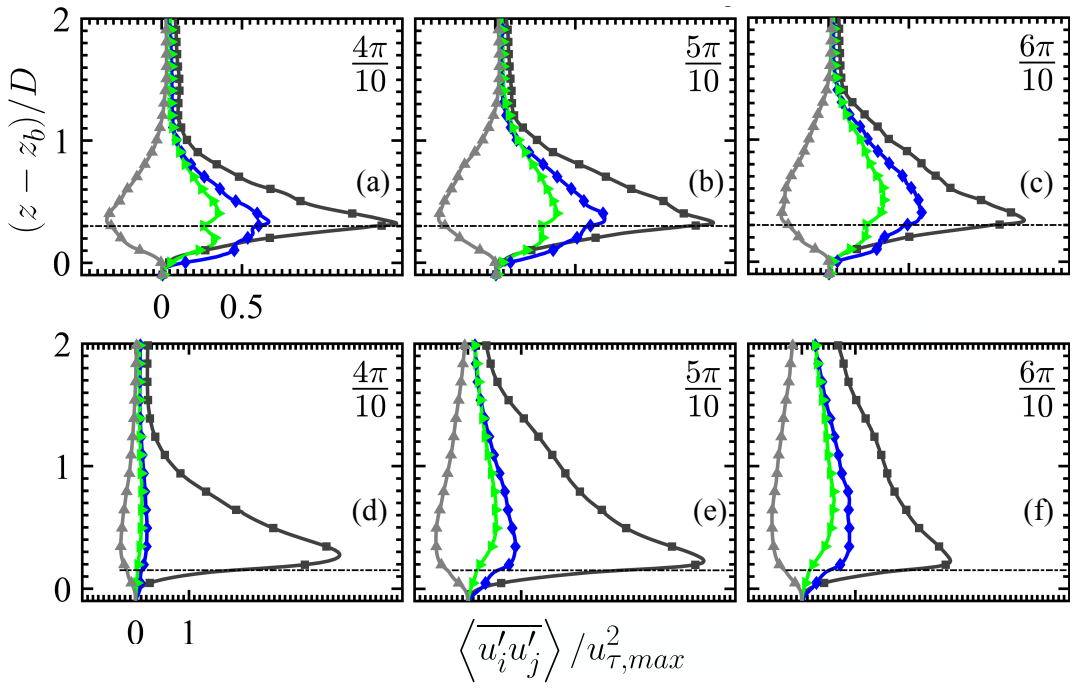

Figure 4.2: Profiles of double-averaged Reynolds stress at various phases in a flow cycle for (a,b,c) gravel and (d,e,f) sand case. Symbols represent: ■, streamwise Reynolds stress $\langle \overline{u'^2} \rangle$; ♦, spanwise Reynolds stress $\langle \overline{v'^2} \rangle$; ►, wall-normal Reynolds stress $\langle \overline{w'^2} \rangle$; ▲, Reynolds shear stress $\langle \overline{u'w'} \rangle$. All the terms are normalized by $u_{\tau,max}^2$. Panels show (a,d) acceleration, (b,e) peak and (c,f) deceleration phase. The dash-dot line at $(z - z_b)/D = 0.3$ in (a,b,c) and at 0.15 in (d,e,f) shows roughness crest level for the gravel and the sand particle, respectively.

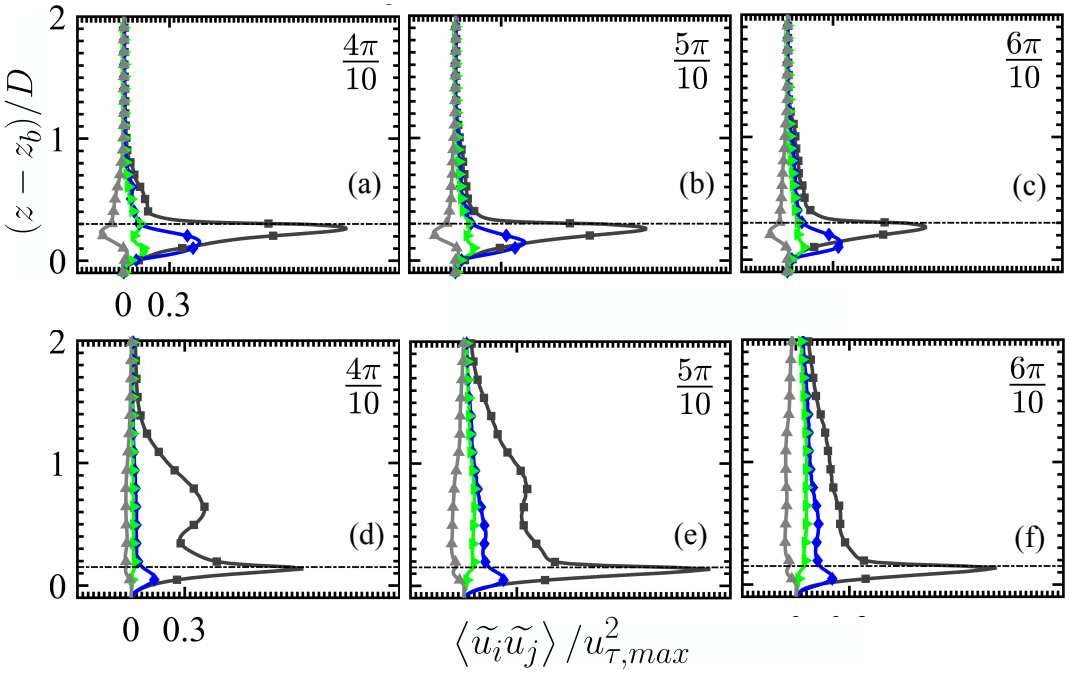

Figure 4.3: Profiles of double-averaged dispersive stress at various phases in a flow cycle for (a,b,c) gravel and (d,e,f) sand case. Symbols represent: ■, streamwise dispersive stress $\langle \widetilde{u}^2 \rangle$; ♦, spanwise dispersive stress $\langle \widetilde{v}^2 \rangle$; ►, wall-normal dispersive stress $\langle \widetilde{w}^2 \rangle$; ▲, shear component of the dispersive stress $\langle \widetilde{u}\widetilde{w} \rangle$. All the terms are normalized by $u^2_{\tau,max}$. Panels show (a,d) acceleration, (b,e) peak and (c,f) deceleration phase. The dash-dot line at $(z - z_b)/D = 0.3$ in (a,b,c) and at 0.15 in (d,e,f) shows roughness crest level for the gravel and the sand particle, respectively.

where, terms on the right-hand side are, respectively, the MKE, the WKE and the TKE.

Schematic representation illustrating various energy transfer mechanisms and their pathways can be found in Fig. 8 from Ghodke & Apte (2016) and is again presented here in Fig. 4.4 for the sake of completeness. As reported by Finnigan (2000), conversion of MKE to the fine-scale TKE takes places in two ways. In the first pathway, the energy goes through the entire energy cascade process converting MKE to TKE and subsequently into heat. In the second alternate pathway (shown in Fig. 4.4 by dashed arrow), the work of mean flow against pressure drag converts MKE to WKE, and WKE then generates TKE of scales smaller than the roughness elements through a process called 'short-circuited' energy cascade (Raupach *et al.*, 1991). Furthermore, as indicated in Fig. 4.4, bi-directional interactions between TKE and WKE can be explained as follows: eddies of all scales larger than the roughness elements work against the pressure drag and lose their TKE to WKE. At the same time, WKE generates TKE of scales smaller than roughness elements through aforementioned short-circuited energy cascade. Take a note that, physical processes represented in this bi-directional exchange involve action on the turbulent eddies rather than the mean flow.

The budget of TKE for the gravel case was reported in (Ghodke & Apte, 2016) where important processes governing TKE–WKE interactions were discussed. In addition, to further explain the phenomenon of redistribution of energy among normal components of Reynolds stresses and illustrate the relative importance of the various processes involved, budgets of normal Reynolds stresses along with normal dispersive stresses are studied here. Based on Raupach & Thom (1981); Mignot *et al.* (2009); Yuan & Piomelli (2014*b*), double-averaged normal Reynolds stress budget equation for flow over roughness with streamwise-spanwise homogeneity is given as,

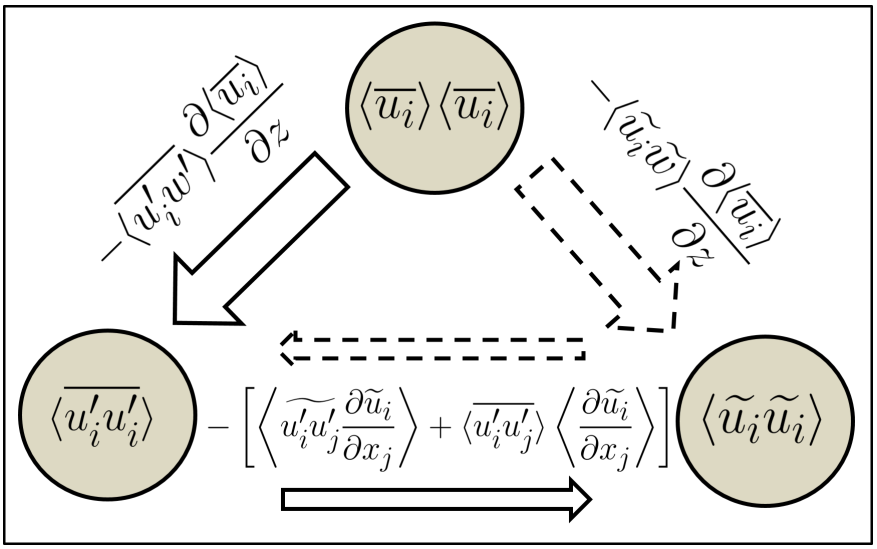

Figure 4.4: Schematic representation of energy transfer mechanisms and their pathways. Dashed arrow path indicates short-circuited energy cascade. Conversion of energy into heat is not illustrated.

$$\frac{\partial\langle\overline{u_\alpha'u_\alpha'}\rangle}{\partial t}=\underbrace{-2\langle\overline{u_\alpha'w'}\rangle\frac{\partial\langle\overline{u}_\alpha\rangle}{\partial z}}_{P_s}+\left[\underbrace{-2\left\langle\widetilde{u_\alpha'u_j'}\frac{\partial\widetilde{u}_\alpha}{\partial x_j}\right\rangle}_{P_w}\underbrace{-2\langle\overline{u_\alpha'u_j'}\rangle\left\langle\frac{\partial\widetilde{u}_\alpha}{\partial x_j}\right\rangle}_{P_m}\right]$$
$$\underbrace{-\frac{\partial}{\partial z}\langle\overline{u_\alpha'u_\alpha'w'}\rangle}_{T_t}\underbrace{-\frac{\partial}{\partial z}\langle\widetilde{u_\alpha'u_\alpha'}\widetilde{w}\rangle}_{T_w}\underbrace{-\frac{2}{\rho}\left\langle\overline{u_\alpha'\frac{\partial p'}{\partial x_\alpha}}\right\rangle}_{\Pi_{\alpha\alpha}}+\nu\frac{\partial^2}{\partial z^2}\langle\overline{u_\alpha'u_\alpha'}\rangle-\langle\overline{\epsilon}_{\alpha\alpha}\rangle \qquad (4.3)$$

where, the eight terms on the right-hand side are, respectively, shear production term, P_s, that represents the work of double-averaged velocity against double-averaged shear; wake production term, P_w, is the work of wake-induced velocity fluctuations against the bed-induced shear. This term represents the net exchange of energy between TKE and WKE; P_m is the work of the bed-induced velocity

fluctuations against double-averaged shear; T_t is turbulent transport, T_w is the bed-induced turbulent transport; $\Pi_{\alpha\alpha}$ is the pressure work followed by seventh term of viscous transport. The last term on the right $\langle\overline{\epsilon}_{\alpha\alpha}\rangle$ represents viscous dissipation rate of $\langle\overline{u_\alpha'^2}\rangle$. Note that the terms P_m, P_w and T_w arise as a result of spatial heterogeneity at roughness element length scale.

Figure 4.5 shows variation of various terms in the budget equation of (a,d) streamwise, (b,e) spanwise and (c,f) wall-normal components of Reynolds stress plotted at a peak phase. Here, panels (a,b,c) show variation in the gravel and (d,e,f) present that in the sand case. The results for gravel and sand case are presented only for the peak phase in a flow cycle. Similar trends albeit with different maxima and minima are observed for rest of the turbulent phases and are presented in Appendix D. Also note that, the quantitative comparison of budget terms in the gravel and the sand case is not reported here as the level of turbulence at peak phase is different in both the cases. Nevertheless, trends discussed here sufficiently elucidate near-bed turbulence characteristics in both flow cases.

As the flow accelerates, standing vortices around the spherical particle begin to form in the streamwise direction; as a result, shear layers start emanating from the upper hemisphere of the particle causing peak in the shear production $P_{s,uu}$ and viscous dissipation ϵ_{uu} close to the roughness crest in both flow cases as shown in Fig. 4.5 (a,d). Consistent with the TKE budget reported in Ghodke & Apte (2016), there exists a negative peak in the wake production term $P_{w,uu}$ close to the roughness crest, indicating the conversion of TKE to WKE. At this location, streamwise component of the Reynolds stress, $\langle\overline{u'^2}\rangle$, contributes most to the TKE and is typically associated with near-bed turbulent structures of length scales larger than the roughness scale. These large-scale structures work against the pressure drag and lose their TKE to WKE, resulting in the negative peak in $P_{w,uu}$. As expected, shear production is almost zero in the budgets of $\langle\overline{v'^2}\rangle$ and $\langle\overline{w'^2}\rangle$, with the only non-negligible production term as the wake production. In both gravel and sand case, $P_{w,vv}$ shows positive peak below the roughness crest indicating conversion of WKE to TKE. At this location, turbulent scales associated with

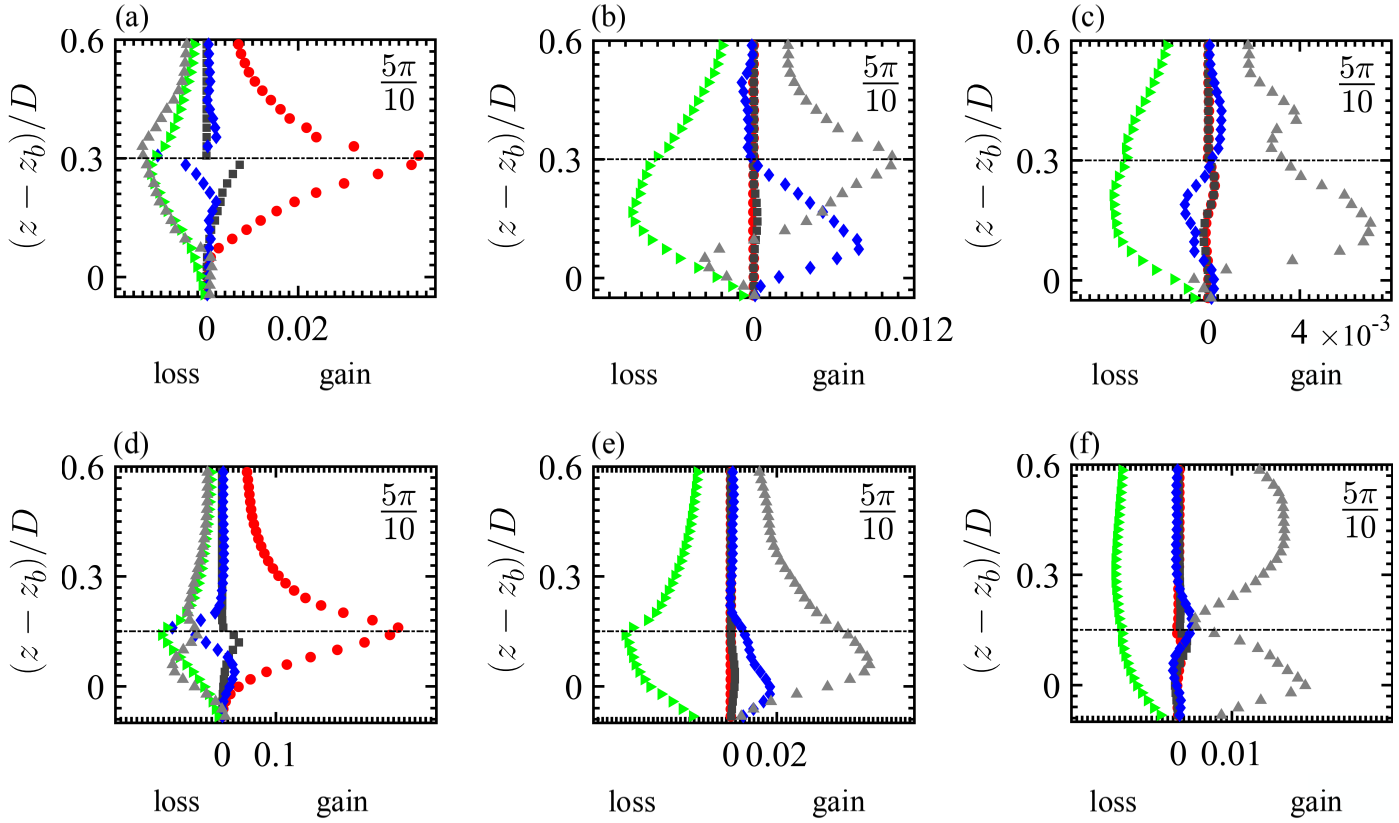

Figure 4.5: Budget at a peak phase ($\omega t = 5\pi/10$) of (a,d) streamwise $\langle\overline{u'^2}\rangle$; (b,e) spanwise $\langle\overline{v'^2}\rangle$; and (c,f) wall-normal $\langle\overline{w'^2}\rangle$ component of Reynolds stress. Symbols represent: ●, P_s; ■, P_m; ◆, P_w; ▶, viscous dissipation; ▲, pressure work. Only selected terms are plotted. Panels (a,b,c) are for the gravel and (d,e,f) are for the sand case. All the terms are normalized by $u^4_{\tau,max}/\nu$. The dash-dot line at $(z - z_b)/D = 0.3$ in (a,b,c) and at 0.15 in (d,e,f) shows roughness crest level for the gravel and the sand particle, respectively.

spanwise Reynolds stress are smaller than the roughness size; therefore converting WKE to TKE through short-circuited energy cascade. Wake production in the budget of $\langle\overline{w'^2}\rangle$ in negligible in comparison with $P_{w,uu}$ and $P_{w,vv}$ for both flow cases. Another production term P_m is slightly positive for both gravel and sand in the streamwise Reynolds stress budget, however is negligible otherwise. In the outer part of the roughness sublayer, all the terms except shear production and dissipation decay to zero, establishing equilibrium outer layer where the rate of production balances the rate of dissipation. Consistent with the gravel case (c.f. Fig. 8) from Ghodke & Apte (2016), net wake production in the TKE budget for sand case (not shown) also exhibits two peaks; positive below the roughness crest and negative close to the crest; indicating transfer of energy from WKE to TKE in the former and TKE to WKE in the latter.

Apart from production and dissipation, another important term in the budget of normal Reynolds stress is the term of pressure work. In both gravel and sand case, pressure work Π_{11} is almost equal to viscous dissipation and acts a dominant sink term in the budget of $\langle\overline{u'^2}\rangle$. Conversely, Π_{22} and Π_{33} are typically positive and serve as source terms in the balance of $\langle\overline{v'^2}\rangle$ and $\langle\overline{w'^2}\rangle$, respectively. Peak in Π_{22} is seen close to the crest in the case of gravel particle and near the zero-displacement plane in the case of sand particle as shown in Fig. 4.5 (b) and (e), respectively. In both gravel and sand case, Π_{33} exhibits two positive peaks; one is located below the roughness crest, while second is above the crest. Magnitudes of these two peaks in the sand case are almost same, however, for the gravel particle, peak in Π_{33} below the roughness crest is almost two times higher than the one above the crest. Presence of these peaks could be attributed to the turbulence–wake interactions in the vicinity of the roughness crest resulting in more enhanced intensification of wall-normal fluctuations, along with increased p' intensity resulting from significant wake-related terms (the second and fourth term) in the source of the p' Poisson equation (Yuan & Piomelli, 2015) given as,

$$\nabla^2 p' = -2\frac{\partial\langle\overline{u_i}\rangle}{\partial x_j}\frac{\partial u_j'}{\partial x_i} - 2\frac{\partial\widetilde{u_i}}{\partial x_j}\frac{\partial u_j'}{\partial x_i} - \frac{\partial^2}{\partial x_i\partial x_j}(u_i'u_j' - \langle\overline{u_i'u_j'}\rangle) - \frac{\partial^2\widetilde{u_i'u_j'}}{\partial x_i\partial x_j} \tag{4.4}$$

As foreshadowed earlier, the positive pressure work terms in both flow cases indicate the tendency of roughness to redistribute energy from streamwise to spanwise and wall-normal fluctuations, resulting in homogenization of the near-wall turbulence.

Following Raupach & Thom (1981); Yuan & Piomelli (2014*b*), double-averaged dispersive Reynolds stress budget equation for flow over roughness with streamwise-spanwise homogeneity is given as,

$$\begin{aligned}\frac{\partial\langle\widetilde{u}_\alpha\widetilde{u}_\alpha\rangle}{\partial t} = \underbrace{-2\langle\widetilde{u}_\alpha\widetilde{w}\rangle\frac{\partial\langle\overline{u}_\alpha\rangle}{\partial z}}_{\widetilde{P}_s} + \Bigg[\underbrace{2\left\langle\widetilde{u_\alpha'u_j'}\frac{\partial\widetilde{u}_\alpha}{\partial x_j}\right\rangle}_{-P_w} + \underbrace{2\langle\overline{u_\alpha'u_j'}\rangle\left\langle\frac{\partial\widetilde{u}_\alpha}{\partial x_j}\right\rangle}_{-P_m}\Bigg] \\ \underbrace{-\frac{\partial}{\partial z}\langle\widetilde{u}_\alpha\widetilde{u_\alpha'w'}\rangle}_{\widetilde{T}_t}\underbrace{-\frac{\partial}{\partial z}\langle\widetilde{u}_\alpha\widetilde{u}_\alpha\widetilde{w}\rangle}_{\widetilde{T}_w}\underbrace{-\frac{2}{\rho}\left\langle\widetilde{u}_\alpha\frac{\partial\widetilde{p}}{\partial x_\alpha}\right\rangle}_{\widetilde{\Pi}_{\alpha\alpha}} + \nu\frac{\partial^2}{\partial z^2}\langle\widetilde{u}_\alpha\widetilde{u}_\alpha\rangle - \langle\widetilde{\epsilon}_{\alpha\alpha}\rangle\end{aligned} \tag{4.5}$$

where, the eight terms on the right-hand side are, respectively, shear production of WKE, $\widetilde{P}_s$; wake production term, $-P_w$; $-P_m$ is the work of the bed-induced velocity fluctuations against double-averaged shear; $\widetilde{T}_t$ is turbulent transport of WKE, $\widetilde{T}_w$ is the transport due to wake; $\widetilde{\Pi}_{\alpha\alpha}$ is the pressure work followed by seventh term of viscous transport and the last term of viscous dissipation rate of $\langle\widetilde{u}_\alpha^2\rangle$. Note that the terms P_w and P_m appear with opposite signs in the budgets of TKE and WKE.

Figure 4.6 shows variation of various terms in the budget equation of (a,d) streamwise, (b,e) spanwise and (c,f) wall-normal components of dispersive Reynolds stress plotted at a peak phase. Again, panels (a,b,c) show variation in the gravel

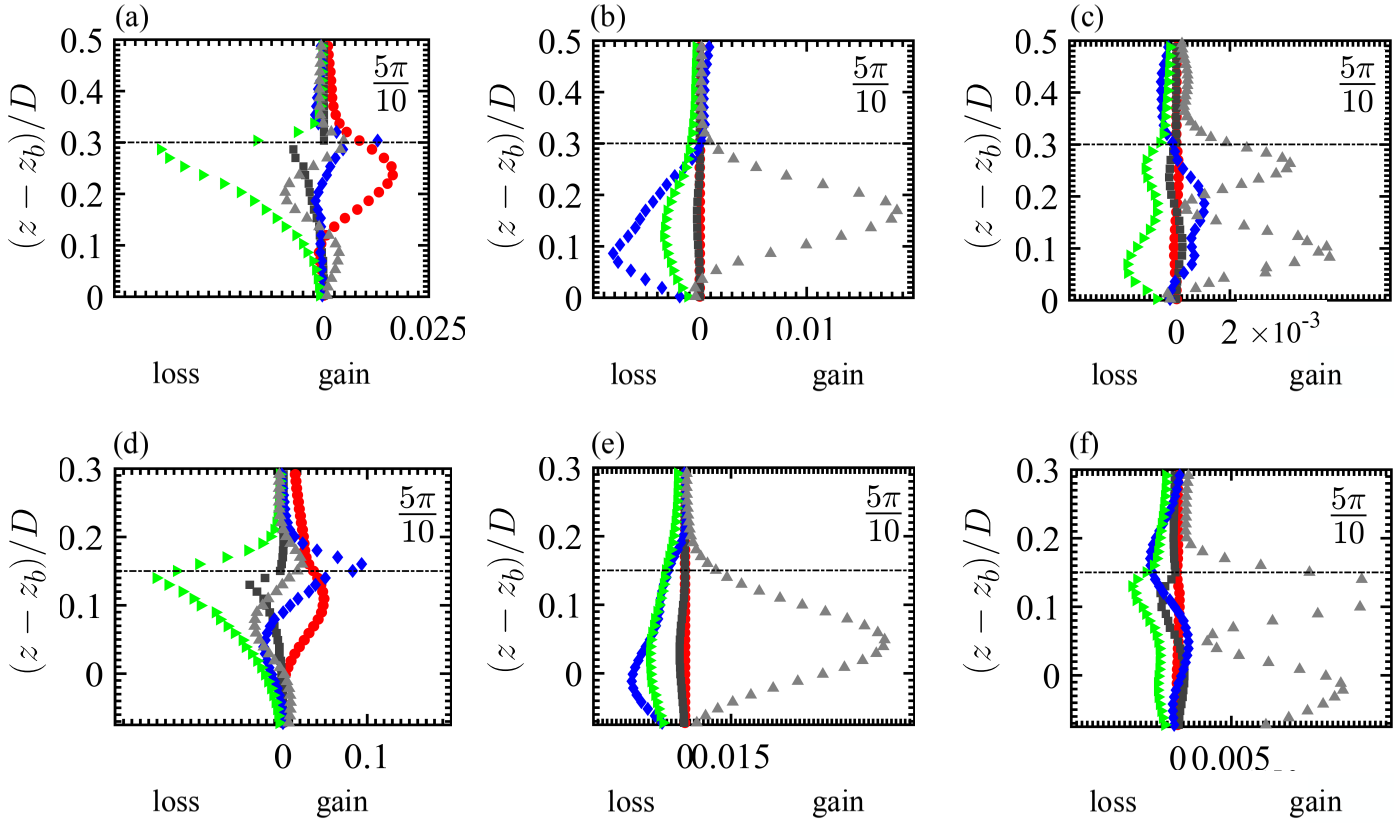

Figure 4.6: Budget at a peak phase ($\omega t = 5\pi/10$) of (a,d) streamwise $\langle\widetilde{u}^2\rangle$; (b,e) spanwise $\langle\widetilde{v}^2\rangle$; and (c,f) wall-normal $\langle\widetilde{w}^2\rangle$ component of dispersive Reynolds stress. Symbols represent: ●, P_s; ■, $(-P_m)$; ♦, $(-P_w)$; ►, viscous dissipation; ▲, pressure work. Only selected terms are plotted. Panels (a,b,c) are for the gravel and (d,e,f) are for the sand case. All the terms are normalized by $u^4_{\tau,max}/\nu$. The dash-dot line at $(z-z_b)/D = 0.3$ in (a,b,c) and at 0.15 in (d,e,f) shows roughness crest level for the gravel and the sand particle, respectively.

and (d,e,f) present that in the sand case. As expected, terms in the dispersive stress budget equation are significant mostly in the vicinity of the crest of gravel and sand particle. As shown in Fig. 4.6 (a,d), the shear production term, $\widetilde{P}_s$, representing the work of the mean flow against the bed-induced stress is significant only for $\langle\widetilde{u}^2\rangle$ and it peaks below the roughness crest in both flow cases. Wake production of the WKE ($-P_{w,uu}$) in the gravel case peaks close to the roughness crest and is almost of the same magnitude as the shear production term $\widetilde{P}_{s,uu}$. On the other hand, interestingly, wake production ($-P_{w,uu}$) in the sand case peaks close to the roughness, however, exceeds the shear production term $\widetilde{P}_{s,uu}$. This is presumably due to elongated streamwise structures in the sand case resulting in large amount of TKE being converted to WKE in comparison to the production of WKE through $\widetilde{P}_{s,uu}$. This suggest that the process of short-circuited energy cascade is less dominant in the sand case. Consistent with normal stress budget, pressure work terms $\widetilde{\Pi}_{22}$ and $\widetilde{\Pi}_{33}$ in both flow cases are typically positive and act as dominant sources below the roughness crest in the balance of $\langle\widetilde{v}^2\rangle$ and $\langle\widetilde{w}^2\rangle$, respectively.

4.3.5 *Turbulence structure*

To further understand the behavior of the near-bed turbulence, large-scale aniostropy and its response to flow oscillations, dimensionless parameters that represent flow structures in turbulent shear flows are examined. As reported by Lee *et al.* (1990), near-wall structures that influence the anisotropy in the turbulent boundary layer are primarily attributed to the effects of mean shear rate. Therefore, to examine the effects of shear rate on the development of near-bed anisotropy in the present flow cases, the shear-rate parameter S^* given as,

$$S^* = \frac{\overline{S}q^2}{2\epsilon}, \tag{4.6}$$

where, $\overline{S} = 2(\overline{S}_{ij}\overline{S}_{ij})^{1/2}$ is the mean strain rate, $\overline{S}_{ij} = (\partial\langle\overline{u}_i\rangle/\partial x_j + \partial\langle\overline{u}_j\rangle/\partial x_i)/2$ is the strain-rate tensor, $q = \langle\overline{u_i'u_i'}\rangle^{1/2}$ is a measure of turbulent velocity scale and ϵ

is the dissipation rate of TKE is calculated. The shear-rate parameter S^* signifies the ratio of turbulence and the mean deformation time scale and quantifies the importance of the mean shear against the shear of the turbulence on the near-bed flow structures. Take a note that, $S^* \approx 10$ is regarded as a lower threshold for observing near-bed horseshoe structures (Lee *et al.*, 1990). Figure 4.7 compares the shear-rate parameter S^* in the gravel and sand case. To examine the effects of flow oscillations, variation at three phases in a flow cycle, i.e. acceleration, peak and deceleration phase is plotted. As shown in Fig. 4.7 (a), the shear-rate parameter in the gravel case attains its maximum, $S^*_{max} \approx 12$, at the gravel crest level and interestingly, does not show any dependence on the flow oscillations. Further away from the gravel crest, in agreement with the conclusions of Lee *et al.* (1990), S^* is close to 5, which implies that elongated coherent structures cannot form. Small difference in S^* values in the inner and outer layer highlights the incompetence of the mean shear to affect the turbulent eddy shape and the Reynolds stress anisotropy in the gravel case. In the case of sand-bed shown in Fig. 4.7 (b), S^* peaks just above the particle crest and takes the maximum value of 30 towards the end of an acceleration cycle at $\omega t = 4\pi/10$, eventually decreasing to $S^*_{max} \approx 12$ later in the flow cycle. Consistent with Lee *et al.* (1990), S^* attains the value between 4 to 5 in the outer part of the roughness sublayer. Contrary to the gravel case, shear-rate parameter for the sand particle shows some dependence on the flow oscillations, especially in the vicinity of the roughness crest. Large values of S^* in the vicinity of the sand particle crest indicate the existence of longer streamwise structures as also visualized in Fig. 4.1 (b). This also implies that the response time of the turbulence in that region is typically higher, and its shape is significantly modified by stretching of the vortex elements leading to the state of $1D$ turbulence on the Lumley's triangle (Choi, 2001).

Following (Yuan & Piomelli, 2015), the ratio of turbulence time scale and that of the bed-induced (wake) strain given by,

$$S^*_w = \frac{S_w q^2}{2\epsilon}, \tag{4.7}$$

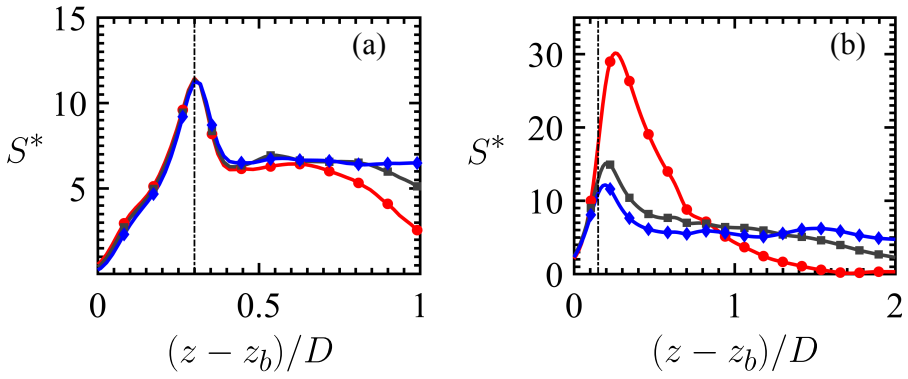

Figure 4.7: Variation of the shear-rate parameter S^* inside the roughness sublayer for (a) gravel and (b) sand case. Symbols represent variation at: ●, acceleration phase $4\pi/10$; ■, peak phase $(5\pi/10)$; ♦, deceleration phase $(6\pi/10)$. The dash-dot lines at $(z-z_b)/D = 0.3$ in (a) and 0.15 in (b) show roughness crest level for gravel and sand, respectively.

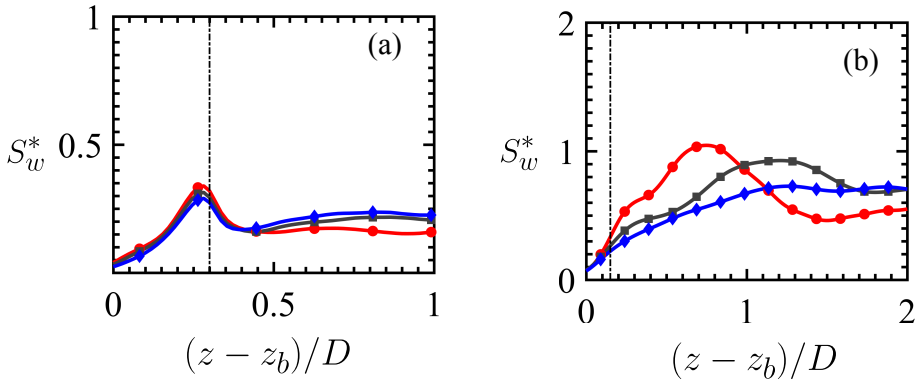

Figure 4.8: Variation of S_w^* inside the roughness sublayer for (a) gravel and (b) sand case. Symbols are same as in Fig. 4.7.

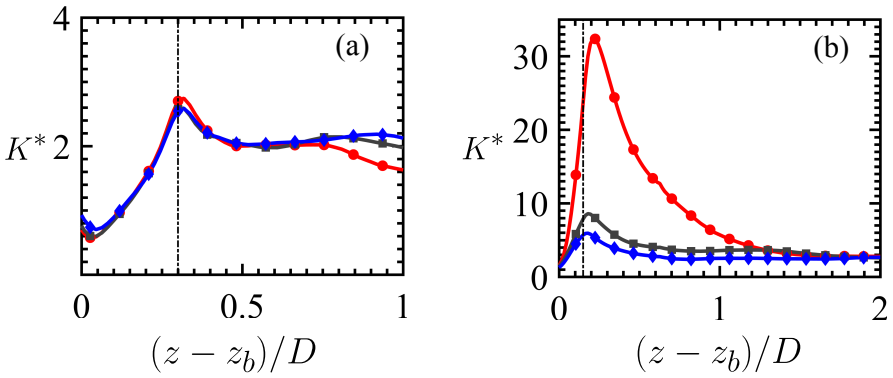

Figure 4.9: Variation of the energy-partition parameter K^* inside the roughness sublayer for (a) gravel and (b) sand case. Symbols are same as in Fig. 4.7.

where, wake strain S_w is approximated as $\langle \widetilde{u}^2 \rangle^{1/2}/D$ is also plotted in Fig. 4.8. Similar to S^*, the variation of S_w^* in the gravel case reveals no dependence on the flow oscillations. As seen in Fig. 4.8 (a), maxima in the S_w^* are found just below the gravel crest with overall values inside the roughness sublayer less than one. In the sand case, S_w^* peaks much away from the particle crest showing reduced dependence on the flow oscillations with overall values of the order of one. These results indicate that the wake strain rate is not sufficient to change the near-bed aniostropy in both flow cases.

In addition, the anisotropic nature of the near-bed structures is also quantified by calculating energy-partition parameter (Lee *et al.*, 1990) given as,

$$K^* = \frac{2\overline{u'^2}}{\overline{v'^2} + \overline{w'^2}} \tag{4.8}$$

where, K^* is a measure of high concentration of TKE in the streamwise component of the normal Reynolds stress. Note that, $K^* = 1$ in the isotropic turbulence and according to Lee *et al.* (1990), the near-bed elongated streaks are known to exist when $K^* > 5$.

Figure 4.9 (a) and (b) shows variation of K^* inside the roughness sublayer for gravel and sand particle, respectively. Consistent with earlier observations, K^* in

the gravel case shows no differences for various phases in a flow cycle and takes values of the order one. This indicates the absence of elongated streaky structures and further corroborates the observation of near-bed flow isotropization in the gravel case. Conversely, in the case of sand particle, $K^*_{max} \approx 33$ towards the end of an acceleration cycle ($\omega t = 4\pi/10$), eventually decreasing to $K^*_{max} \approx 10$ at the peak phase ($\omega t = 5\pi/10$). This reduction in the value of K^*_{max} with flow acceleration is attributed to the intensification of near-bed bursting phenomenon close to the peak phase, leading to enhanced redistribution of the energy from streamwise to other two components of the normal Reynolds stress. However, in comparison to the gravel case, the extent of near-bed flow isotropization is typically less for the sand-bed.

4.4 Conclusions

A numerical study of oscillatory turbulent flow over a bed of closely packed spherical particles of diameter 375 (125) in wall units, corresponding to the gravel (sand) particle, in a very rough turbulent flow regime is carried out. Detailed characterization of the near-bed turbulence by employing double-averaging technique is reported.

It was shown that the roughness leads to a wake field that in turn results in dispersive stresses in the vicinity of the particle-bed. In the case of gravel, such bed-induced stresses were significant mostly in the vicinity of the particle crest, while for the sand case, their effect was seen to penetrate up to the distance of $2D$ above the particle-bed.

The spatial inhomogeneity at roughness length scale introduced additional production and transport terms in double-averaged Reynolds stress budget. In both flow cases, negative peak in the wake production term $P_{w,uu}$ is observed close to the roughness crest and was attributed to the conversion of TKE to WKE as a result of larger turbulent scales that are associated with $\langle\overline{u'^2}\rangle$ at this location. In addition, positive peak in the wake production $P_{w,vv}$ of spanwise component of the Reynolds stress was observed close to the effective bed location, indicating

the conversion of WKE to TKE of scales smaller than roughness length scale at this location. The pressure work term in the budget of $\langle\overline{u'^2}\rangle$ for both gravel and sand case remained negative and worked as a dominant sink. On the other hand, intensified turbulence–wake interactions led to positive pressure work in the budgets of $\langle\overline{v'^2}\rangle$ and $\langle\overline{w'^2}\rangle$, resulting in redistribution of energy between components of Reynolds stresses. In both flow cases, bed-induced transport term was found to be negligible.

For the grave-bed, amount of WKE converted from TKE (through $-P_{w,uu}$) is of the same order as that received from MKE (through $\widetilde{P}_{s,uu}$). On the contrary, presence of elongated streamwise structures in the sand case resulted in augmentation of the wake production term $-P_{w,uu}$ that is larger compared to shear production term $\widetilde{P}_{s,uu}$. This therefore suggests that the process of short-circuited energy cascade is less dominant in the sand case.

The large size of the gravel particles was seen to play an important role in forming and then breaking the streamwise structures, leading to isotropization of the near-bed flow; while in the sand case, elongated horseshoe structures formed as a result of high shear rate. Small values of the shear-rate parameter in the gravel case highlights the incompetence of the mean shear to affect the turbulent eddy shape and the Reynolds stress anisotropy. Contrary to this, large shear-rate parameter in the sand case indicated the importance of mean strain rate in modifying the shape of the near-bed turbulence.

Variation of the normal components of the Reynolds stress showed fraction of energy from streamwise component being redistributed to other two components, more so for the gravel case as that compared to the sand. As also evident from energy-partition parameter, redistribution of energy in the gravel case showed no dependence on the flow oscillations, while for the sand particle it is more pronounced towards the end of an acceleration cycle.

Acknowledgments

This work is supported by the National Science Foundation (NSF-CBET - 1133363). The computations were performed on the Texas Advanced Computing Center's Stampede machine.

Chapter 5: Concluding remarks

A detailed conclusion section is provided in each of the preceding chapters. In this section, salient features of the present investigation are reiterated in a more general perspective.

The work is motivated by the fact that lack of accurate criteria for onset of sediment erosion under oscillatory turbulent flow conditions remains one of the biggest hurdles in developing better predictive models for coastal sediment transport. These flows are typically turbulent in nature and to study the dynamics of particle-bed mobility, it is important to understand the complex interactions between turbulence and sediment grains. Several studies have investigated steady, unidirectional flow (representative of stream and river environments) over sediment beds, however, such detailed findings pertaining to oscillatory turbulent flows have not been well documented. Main focus of the study was, therefore, to perform detailed characterization of the turbulent flow field along with statistical analyses of unsteady hydrodynamic forces on the particle-bed subjected to oscillatory flow environment.

Particle-resolved direct numerical simulations were performed to investigate the behavior of an oscillatory flow field over a bed of closely packed fixed spherical particles for a range of Reynolds numbers in transitional and rough turbulent regime. The presence of particles was seen to greatly affect the structure of the near-bed turbulence, indicated by increased bed shear stress, energized sweep-burst motions, non-Gaussian flow distribution and marked changes in turbulent energy transport mechanisms. It was also reported that the roughness facilitates redistribution of energy from more energetic streamwise structures to other two components of the Reynolds stress, therefore, severely modifying the shape of the near-bed turbulent structures resulting in reduction in the near-bed anisotropy.

A double-averaging technique of the flow field revealed spatial inhomogeneities

at the roughness scale and alternate pathways of energy transport mechanism. The presence of wake field in the vicinity of the roughness elements resulted in additional bed-induced stresses that act like source or sink terms in the turbulent kinetic energy balance. As a result, the wake field promotes pronounced inner–outer layer interactions in turbulent boundary layer.

Statistical descriptions of unsteady hydrodynamic forces on the particle-bed, their temporal correlations as well as cross-correlations with near-bed turbulent flow field were reported. Near-bed turbulent flow structures were found to be responsible for governing the time scales of fluctuating forces on the particle-bed, therefore, substantiating the presence of the link between near-bed structures and unsteady hydrodynamic forces on sediment particles. The spectral content of drag and lift fluctuations was examined to reveal roughly two scaling regions for the mid- and high-frequency range, identical to other unidirectional flow cases. This therefore, indicates universal nature of the force fluctuations on the roughness-bed. Based on the concept of impulse, intermittency in the drag and lift forces was also investigated. Typically, intermittency in the lift force was found higher as that compared to the drag, also evident from higher kurtosis values for the lift. Moreover, the implications of selecting a certain threshold criterion for erosion onset based on the intermittency in the drag and lift forces were also discussed. These finding will hopefully provide better understanding of the oscillatory turbulence over roughness elements.

APPENDICES

Appendix A:

Table A.1 tabulates the parameters used to perform grid resolution study for $Re_\delta = 400$. Uniform grids are used in the region surrounding the roughness bed (up to z = 10δ) and grids are stretched in the wall-normal direction (above z = 10δ) using a hyperbolic tangent function. Case C1 represents current simulation parameters, while case C2 is finer grid resolution. To limit the computational requirements in case C2, grid points are clustered up to z = 8δ region with around 375 points per particle diameter. Furthermore, appropriateness of vertical extent of the domain was also tested by running case C3 with the increased domain height of 45δ (grid resolution in the near-bed region is kept same as that of case C1).

As seen in Fig. A.1, velocity profile is unchanged even after increasing the number of grid points (case C2), therefore, confirming the adequacy of the present grid resolution (case C1). It can also be seen that, increasing the vertical extent of the domain (case C3) has no impact on the near-bed velocity distribution. In addition, the normalized boundary layer thickness, maximum friction factor, and also the maximum values of period-averaged turbulence intensities showed no discernible impact of increasing the number of grid points.

Case	Nx	Ny	Nz	Nz/D	Height
C1 (present)	208	152	832	300	30δ
C2	250	180	832	375	30δ
C3	208	152	832	300	45δ

Table A.1: Grid resolution study for $\mathrm{Re}_\delta = 400$.

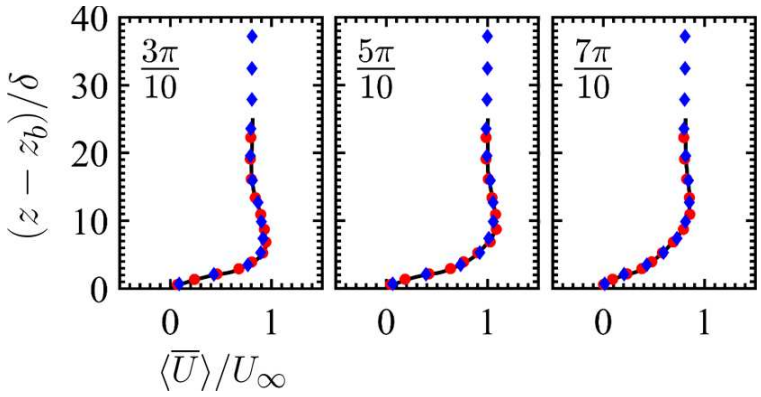

Figure A.1: For $\mathrm{Re}_\delta = 400$, phase evolution of normalized double-averaged streamwise velocity profile. Symbols represent: $-$, C1 (present grid resolution and domain); •, C2 (refined grid resolution); ♦, C3 (present grid resolution and larger domain).

Appendix B:

The domain size in the periodic directions is verified to be sufficiently large by calculating two-point spatial velocity correlation functions, in both streamwise and spanwise directions, by doubling the domain. Figure B.1 and Fig. B.2 show two-point velocity spatial correlation functions for the gravel and the sand case, respectively. The correlations showed no significant effect of the domain size, and confirm the adequacy of the present domain to accommodate the largest turbulent structures.

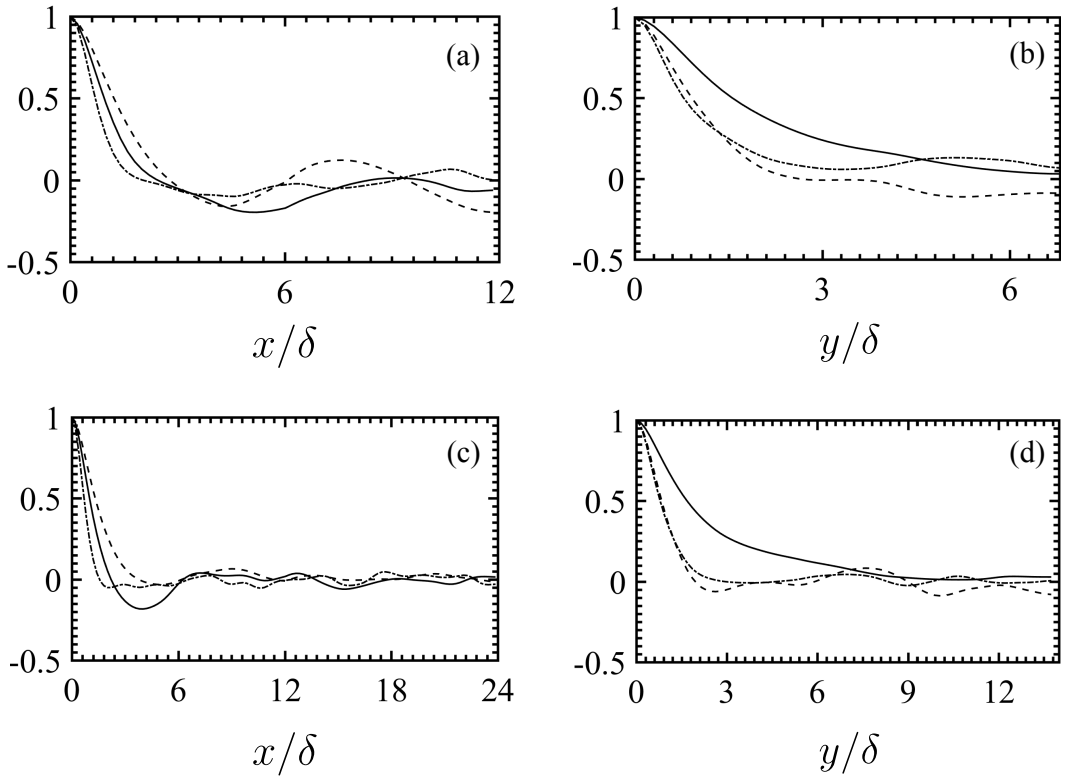

Figure B.1: Two-point velocity spatial correlation functions for the gravel case ($\mathrm{Re}_\delta = 400$) along (a,c) streamwise direction and (b,d) spanwise direction. Panels (a,b) and (c,d) show correlations in the small and large domain, respectively. Lines represent: (—), streamwise velocity; (- - -), spanwise velocity; (···), vertical velocity component. Plots span half the computational domain.

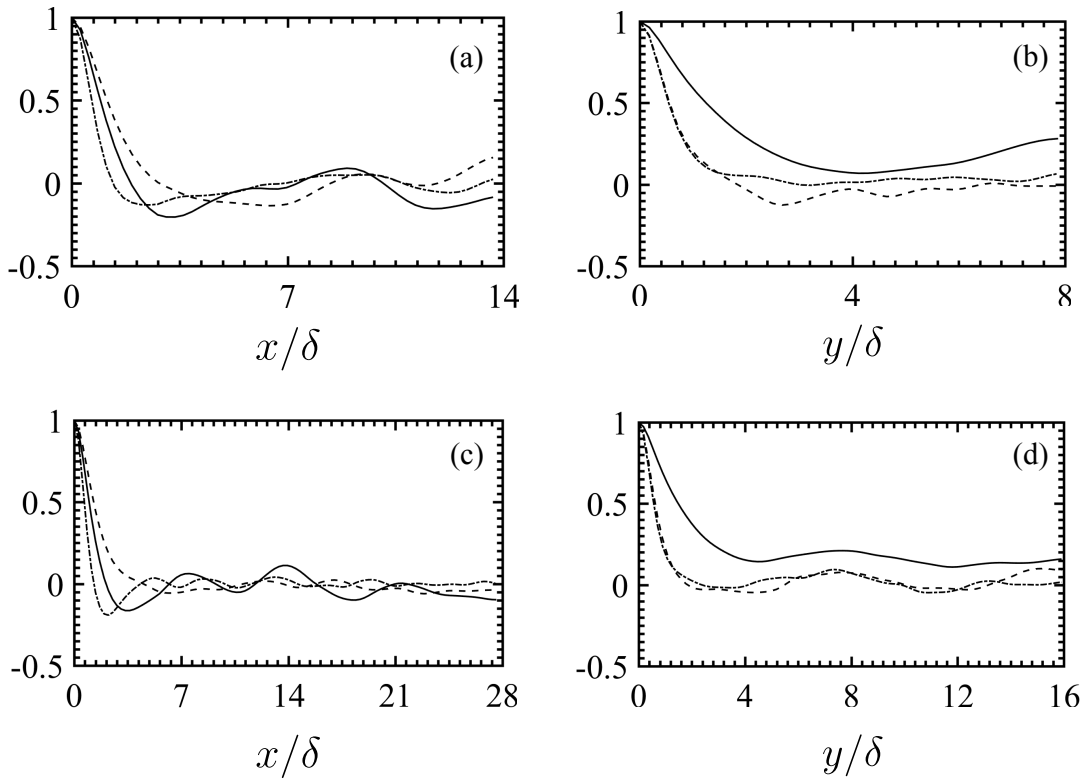

Figure B.2: Two-point velocity spatial correlation functions for the sand case (Re_δ = 545) along (a,c) streamwise direction and (b,d) spanwise direction. Panels (a,b) and (c,d) show correlations in the small and large domain, respectively. Lines represent: (—), streamwise velocity; (- - -), spanwise velocity; (···), vertical velocity component. Plots span half the computational domain.

Appendix C:

In addition to validation shown in Fig. 2.3, instantaneous velocity data at several points above the sphere crest for $\mathrm{Re}_\delta = 95$ is plotted in Fig. C.1 and can be compared against (c.f. Fig. 2) from experimental work of Keiller & Sleath (1976). Figure C.1 is presented in the fluid-frame to be consistent with experimental convention. The plot should therefore approach a sinusoidal profile in the limit as βz (normalized height with $\beta = 1/\delta$) approaches zero. It should be noted that, our overall values are similar in magnitude at various phases compared to the experiments, however, the data of Keiller & Sleath (1976) features fluctuations in the limit ($\beta z < 0.4$) which are not present in the simulations. Test have been conducted with refined meshes and larger domains without observing much change in the magnitudes of these high frequency oscillations. Brief explanation conjecturing the reasons for this small discrepancy is given as following.

As noted earlier, experiments by Keiller & Sleath (1976) were performed by oscillating the rough-bed in still water, whereas, present simulations corresponds to oscillatory fluid flow over a fixed bed. In theory, such change in reference frame can have some small effects and differences. For example, when a body moves in an otherwise still water, there will be no pressure gradient created by the acceleration of the outer flow and therefore Froude-Krylov force will be absent. However, when the body is stationary and the fluid oscillates, Froude-Krylov force will be non-zero owing to the axial pressure gradient created by the acceleration of the outer flow. Changing the frame of reference to facilitate the comparison with experimental data only accounts partially for these effects. For example, data of Keiller & Sleath (1976) do not show any significant oscillations for location away from the bed ($z/\delta = 2.29$). In contrast to Keiller & Sleath (1976), present simulation data employs oscillatory flow over a fixed bed and predicts higher oscillations (with magnitudes on the order of $0.1U_\infty$) in the velocity measured at a location away from the bed

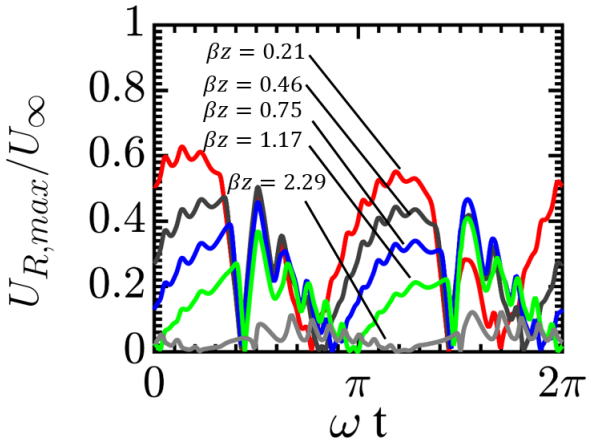

Figure C.1: For $\mathrm{Re}_\delta = 95$, variation of normalized fluid-frame velocity over a cycle, plotted at various heights above the roughness crest location.

($z/\delta = 2.29$); which may potentially be attributed to the way harmonic motion is imposed, either on fluid (or body) and resultant presence (or absence) of additional axial pressure gradients due to Froude-Krylov force.

Appendix D:

Figure D.1 and Fig. D.2 show variation of various terms in the budget equation of (a,d) streamwise, (b,e) spanwise and (c,f) wall-normal components of Reynolds stress plotted at accelerating ($\omega t = 4\pi/10$) and decelerating ($\omega t = 6\pi/10$) phase, respectively. Here, panels (a,b,c) show variation in the gravel and (d,e,f) present that in the sand case.

Figure D.3 and Fig. D.4 show variation of various terms in the budget equation of (a,d) streamwise, (b,e) spanwise and (c,f) wall-normal components of dispersive Reynolds stress plotted at accelerating ($\omega t = 4\pi/10$) and decelerating ($\omega t = 6\pi/10$) phase, respectively. Again, panels (a,b,c) show variation in the gravel and (d,e,f) present that in the sand case.

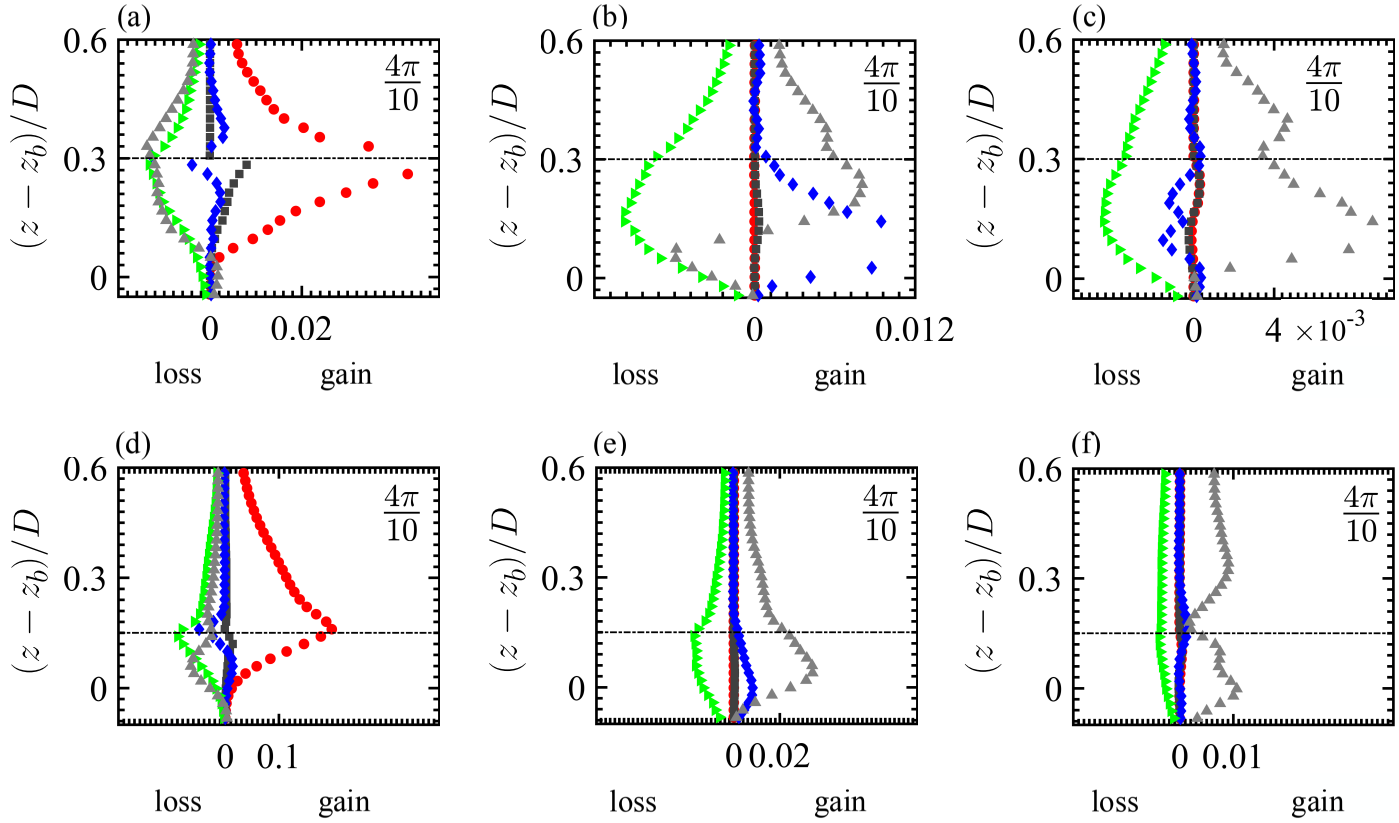

Figure D.1: Budget at an accelerating phase ($\omega t = 4\pi/10$) of (a,d) streamwise $\langle\overline{u'^2}\rangle$; (b,e) spanwise $\langle\overline{v'^2}\rangle$; and (c,f) wall-normal $\langle\overline{w'^2}\rangle$ component of Reynolds stress. Symbols represent: ●, P_s; ■, P_m; ♦, P_w; ►, viscous dissipation; ▲, pressure work. Only selected terms are plotted. Panels (a,b,c) are for the gravel and (d,e,f) are for the sand case. All the terms are normalized by $u^4_{\tau,max}/\nu$. The dash-dot line at $(z-z_b)/D = 0.3$ in (a,b,c) and at 0.15 in (d,e,f) shows roughness crest level for the gravel and the sand particle, respectively.

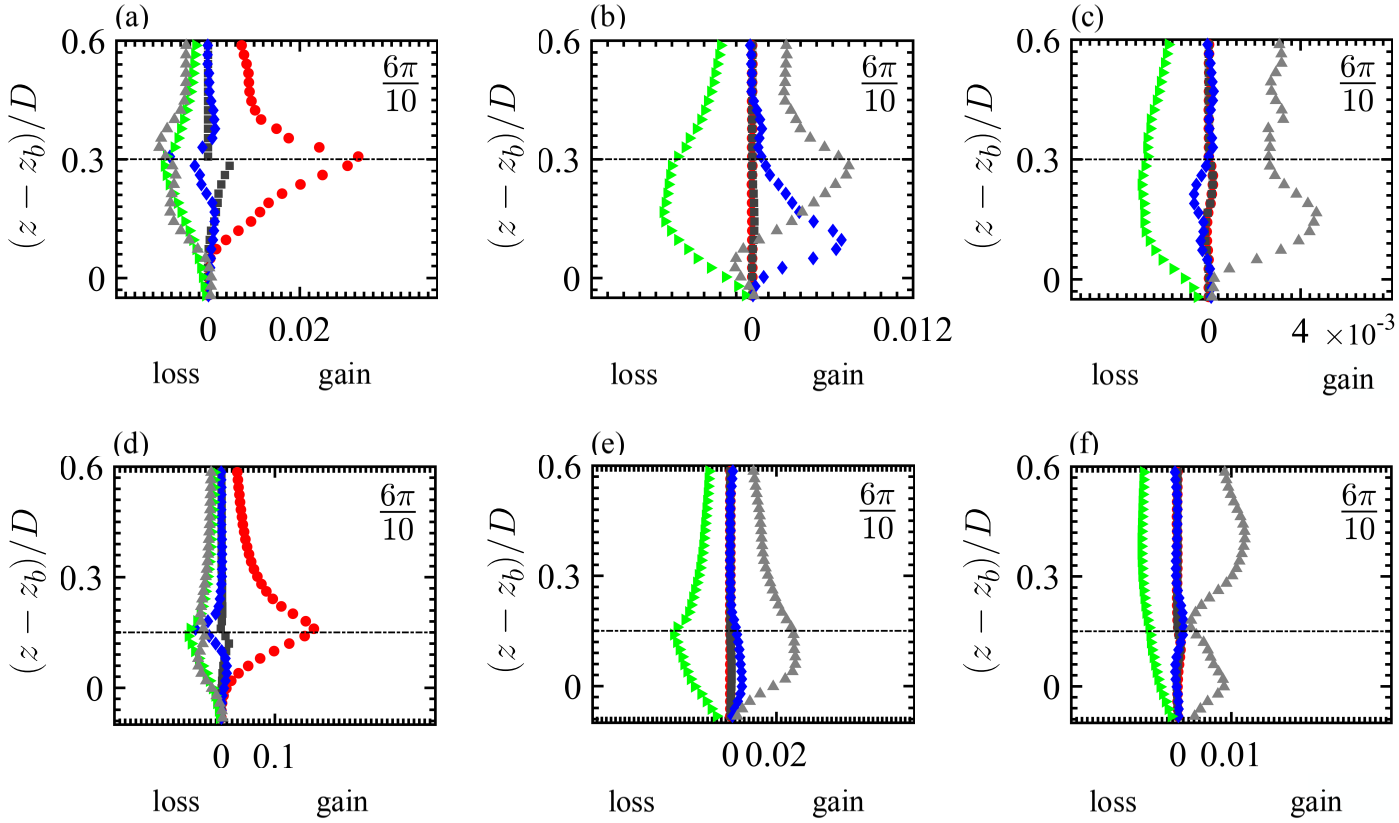

Figure D.2: Budget at a decelerating phase ($\omega t = 6\pi/10$) of (a,d) streamwise $\langle\overline{u'^2}\rangle$; (b,e) spanwise $\langle\overline{v'^2}\rangle$; and (c,f) wall-normal $\langle\overline{w'^2}\rangle$ component of Reynolds stress. Symbols represent: ●, P_s; ■, P_m; ◆, P_w; ▶, viscous dissipation; ▲, pressure work. Only selected terms are plotted. Panels (a,b,c) are for the gravel and (d,e,f) are for the sand case. All the terms are normalized by $u^4_{\tau,max}/\nu$. The dash-dot line at $(z-z_b)/D = 0.3$ in (a,b,c) and at 0.15 in (d,e,f) shows roughness crest level for the gravel and the sand particle, respectively.

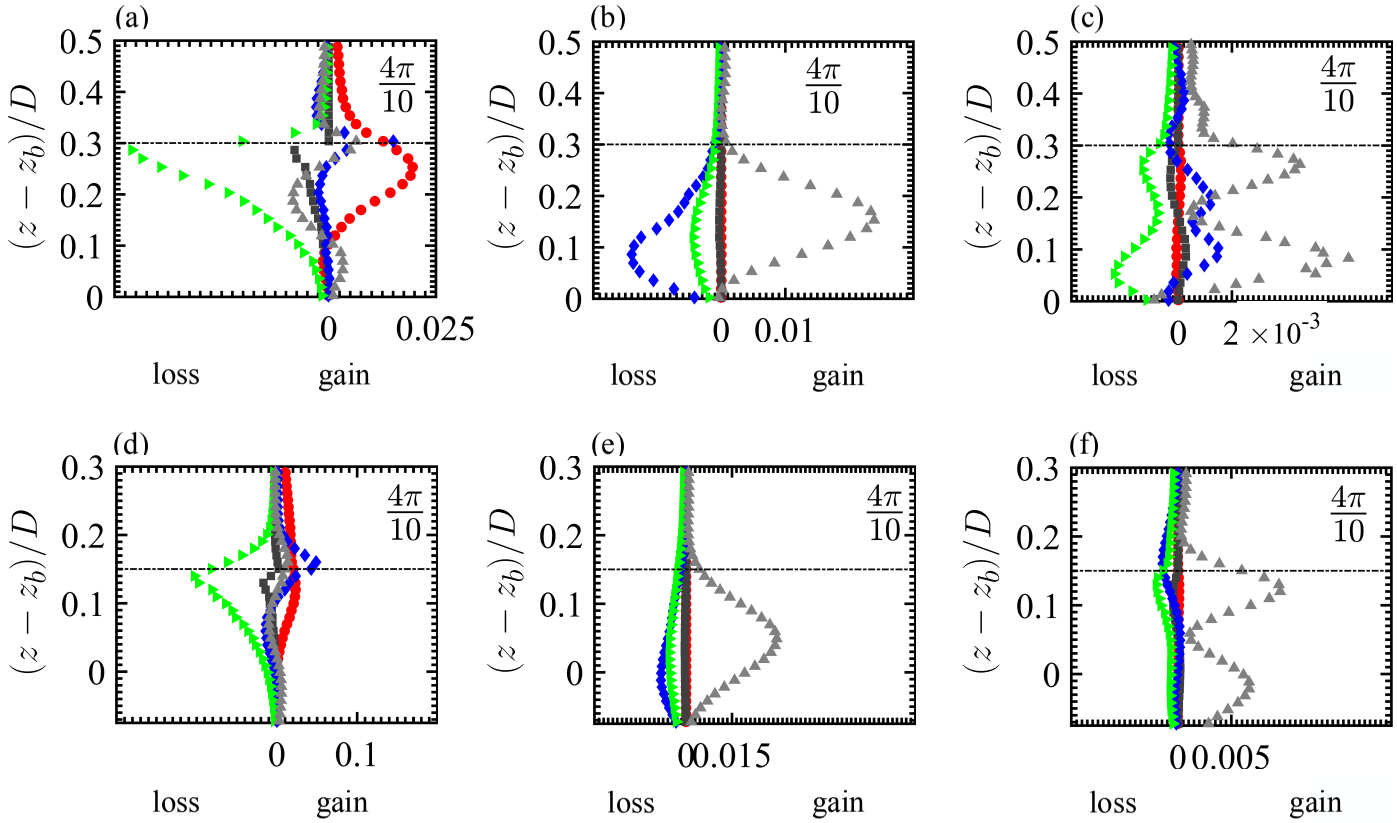

Figure D.3: Budget at an accelerating phase ($\omega t = 4\pi/10$) of (a,d) streamwise $\langle\widetilde{u}^2\rangle$; (b,e) spanwise $\langle\widetilde{v}^2\rangle$; and (c,f) wall-normal $\langle\widetilde{w}^2\rangle$ component of dispersive Reynolds stress. Symbols represent: ●, P_s; ■, $(-P_m)$; ♦, $(-P_w)$; ►, viscous dissipation; ▲, pressure work. Only selected terms are plotted. Panels (a,b,c) are for the gravel and (d,e,f) are for the sand case. All the terms are normalized by $u^4_{\tau,max}/\nu$. The dash-dot line at $(z-z_b)/D = 0.3$ in (a,b,c) and at 0.15 in (d,e,f) shows roughness crest level for the gravel and the sand particle, respectively.

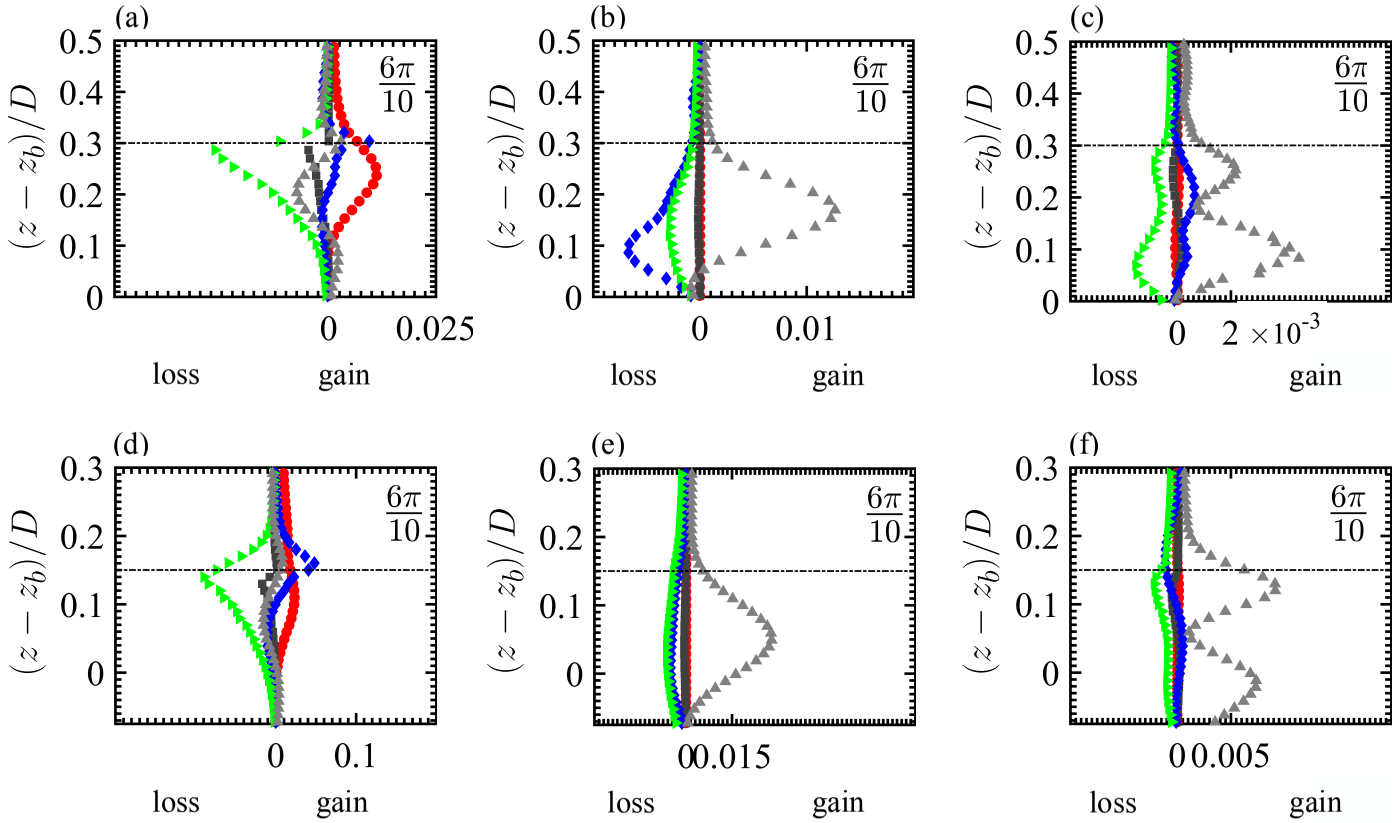

Figure D.4: Budget at a decelerating phase ($\omega t = 6\pi/10$) of (a,d) streamwise $\langle\widetilde{u}^2\rangle$; (b,e) spanwise $\langle\widetilde{v}^2\rangle$; and (c,f) wall-normal $\langle\widetilde{w}^2\rangle$ component of dispersive Reynolds stress. Symbols represent: ●, P_s; ■, $(-P_m)$; ♦, $(-P_w)$; ▶, viscous dissipation; ▲, pressure work. Only selected terms are plotted. Panels (a,b,c) are for the gravel and (d,e,f) are for the sand case. All the terms are normalized by $u^4_{\tau,max}/\nu$. The dash-dot line at $(z-z_b)/D = 0.3$ in (a,b,c) and at 0.15 in (d,e,f) shows roughness crest level for the gravel and the sand particle, respectively.

Bibliography

van der A, Dominic., O'Donoghue, T., Davies, A.G. & Ribberink, J.S. 2011 Experimental study of the turbulent boundary layer in acceleration-skewed oscillatory flow. *J. Fluid Mech.* **684**, 251–283.

Amir, M., Nikora, V.I. & Stewart, M.T. 2014 Pressure forces on sediment particles in turbulent open-channel flow: a laboratory study. *J. Fluid Mech.* **757**, 458–497.

Antonia, R.A. & Krogstad, P.-A. 2001 Turbulence struture in boundary layers over different types of surface roughness. *Fluid Dyn. Res.* **28**, 139–157.

Apte, S.V. & Finn, J.R. 2013 A variable-density fictitious domain method for particulate flows with broad range of particle-fluid density ratios. *J. Comput. Phys.* **243**, 109–129.

Apte, S.V., Mahesh, K. & Moin, P. 2009*a* Large–eddy simulation of evaporating spray in a coaxial combustor. *Proc. Combust. Inst.* **32**, 2247–2256.

Apte, S.V., Mahesh, K., Moin, P. & Gorokhovski, M. 2009*b* Stochastic modeling of atomizing spray in a complex swirl injector using large–eddy simulation. *Proc. Combust. Inst.* **32**, 2257–2266.

Apte, S.V., Mahesh, K., Moin, P. & Oefelein, J.C. 2003 Large-eddy simulation of swirling particle-laden flows in a coaxial-jet combustor. *Int. J. Mult. Flow* **29** (8), 1311–1331.

Apte, S.V., Martin, M. & Patankar, N.A. 2008 A numerical method for fully resolved simulation (FRS) of rigid particle-flow interactions in complex flows. *J. Comput. Phys.* **228** (8), 2712–2738.

Bagnold, R.A. 1966 An approach to the sediment transport problem from general physics. *US Geological Survey Professional Paper* **422** (1), 1–37.

Cardillo, J., Chen, Y., Araya, G., Newman, J., Jansen, K. & Castillo, L. 2013 DNS of a turbulent boundary layer with surface roughness. *J. Fluid Mech.* **729**, 603–637.

Celik, A., Diplas, P. & Dancey, C. 2013 Instantaneous turbulent forces and impulse on a rough bed: Implications for initiation of bed material movement. *Water Resources Res.* **49**, 2213–2227.

Celik, A., Diplas, P. & Dancey, C. 2014 Instantaneous pressure measurements on a spherical grain under threshold conditions. *J. Fluid Mech.* **741**, 60–97.

Celik, A., Diplas, P., Dancey, C. & Valyrakis, M. 2010 Impulse and particle dislodgement under turbulent flow conditions. *Physics. Fluids* **22**.

Chan-Braun, C. 2012 Turbulent open channel flow, sediment erosion and sediment transport. PhD thesis, Karlsruhe Institute of Technology,Germany.

Chan-Braun, C., Garcia-Villalba M & Uhlmann, M. 2011 Force and torque acting on particles in transitionally rough open-channel flow. *J. Fluid Mech.* **684** (441).

Chan-Braun, C., Garcia-Villalba M & Uhlmann, M. 2013 Spatial and temporal scales of force and torque acting on wall-mounted spherical particles in open channel flow. *Phy. Fluids* **25** (7).

Chen, D., Chen, C., Tang, F.-E., Stansby, P. & Li, M. 2007 Boundary layer structure of oscillatory open-channel shallow flows over smooth and rough beds. *Exp. Fluids* **42** (5), 719–736.

Cheng, N. & Chiew, Y. 1998 Pick-up probability for sediment entrainment. *J. hydaulic Eng.* **124**.

Cheng, N. & Law, A. Wing-Keung 2003 Fluctuations of turbulent bed shear stress. *J. Eng. Mech.* **129**, 126–130.

Choi, K.and Lumley, J. 2001 The return to isotropy of homogeneous turbulence. *J. Fluid Mech.* **436**, 59–84.

Coceal, O., Thomas, T. G., Castro, I. P. & Belcher, S. E. 2006 Mean flow and turbulence statistics over groups of urban-like cubical obstacles. *Boundary-Layer Meteorol.* **121**, 491–519.

Corvaro, S., Miozzi, M., Postacchini, M., Mancinelli, A. & Brocchini, M. 2014 Fluid-particle interaction and generation of coherent structures over permeable beds: an experimental analysis. *Adv. Water Res.* **72**, 97–109.

Detert, M., Weitbrecht, V. & Jirka, G.H. 2010 Laboratory measurements on turbulent pressure fluctuations in and above gravel beds. *J. Hydraulic Eng.* **136**, 779–789.

Dey, S. & Das, R. 2012 Gravel-bed hydrodynamics: double-averaging approach. *J. Hydraulic Eng.* **138**, 707–725.

Ding, L. & Zhang, Q-H. 2010 Lattice Boltzmann simulation to characterize roughness effects of oscillatory boundary layer flow over a rough bed. *Proc. 32nd Conference on Coastal Eng.* pp. 1–11.

Diplas, P., Dancey, C., Celik, A., Valyrakis, M., Greer, K. & Akar, T. 2008 The role of impluse on the initiation of particle movement under turbulent flow conditions. *Science* **322**.

Dixen, M., Hatipoglu, F., Sumer, B. M. & Fredsøe, J. 2008 Wave boundary layer over a stone-covered bed. *Coastal Eng.* **55**, 1–20.

Drake, T.G., Shreve, R.L., Dietrich, W.E., Whiting, P.J. & Leopold, L.B. 1988 Bedload transport of fine gravel observed by motion-picture photography. *J. Fluid Mech.* **192**, 193–217.

Dwivedi, A. 2010 Mechanics of sediment entrainment. PhD thesis, The University of Auckland.

Dwivedi, A., Melville, B. & Shamseldin, A.Y. 2010 Hydrodynamic forces generated on spherical sediment particle during entrainment. *J. Hydraulic Eng.* **136**, 756–769.

Einstein, H. 1950 The bed-load function for sediment transportation in open channel flows. *U.S. Dept. of Agriculture, Washington, DC* .

Finn, J. & Apte, S. V 2013 Relative performance of body fitted and fictitious domain simulations of flow through fixed packed beds of spheres. *Int. J. Mult. Flow* **56**, 54–71.

Finnigan, J. 2000 Turbulence in plant canopies. *Annual Rev. Fluid Mech.* **32**, 519–571.

Flores, N. & Sleath, J. 1998 Mobile layer in oscillatory sheet flow. *J. Geophysical Reseach* **103**.

Fornarelli, F. & Vittori, G. 2009 Oscillatory Boundary Layer Close to a Rough Wall. *European J. of Mechanics B/Fluid* **28**, 283–295.

Fredsøe, J. & Deigaard, R. 1992 *Mechanics of Coastal Sediment Transport*. World Scientific.

George, W.K., Beuther, P.D. & Arndt, R.E. 1984 Pressure spectra in turbulent free shear flows. *J. Fluid Mech.* **148**, 148–191.

Ghodke, C.D. & Apte, S.V. 2016 DNS study of particle-bed–turbulence interactions in an oscillatory wall-bounded flow. *J. Fluid Mech.* **792**, 232–251.

Ghodke, C.D., Apte, S.V. & Urzay, J. 2014*a* Direct numerical simulations of oscillatory wall-bounded flow over a closely-packed fixed bed of spherical particles. *Proc. Center for Turbulence Research Summer Prog.* pp. 47–55.

Ghodke, C.D., Skitka, J. & Apte, S.V. 2014*b* Characterization of oscillatory boundary layer over a closely packed bed of sediment particles. *J. Comput. Multiphase Flows* **6** (4), 187–197.

Hofland, B. 2005 Rock and roll, turbulence-induced damage to granular bed protections. PhD thesis, Delft University of Technology, Netherlands.

Hofland, B. & Battjes, J. 2006 Probability density function of instantaneous drag forces and shear stresses on a bed. *J. Hydraulic Eng.* **132**, 1169–1175.

Hofland, B., Battjes, J. & Booij, R. 2005 Measurement of fluctuating pressures on coarse bed material. *J. Hydraulic Eng.* **131**, 770–781.

Ikeda, T. & Durbin, P.A. 2007 Direct simulations of a rough-wall channel flow. *J. Fluid Mech.* **571**, 235–263.

Jensen, B.L., Sumer, B.M. & Fredsøe, J. 1989 Turbulent oscillatory boundary layers at high reynolds numbers. *J. Fluid Mech.* **206**, 265–297.

Jeong, J. & Hussain, F. 1995 On the identification of a vortex. *J. Fluid Mech.* **285**, 69–94.

Jiménez, J. 2004 Turbulent flow over rough walls. *Annual Rev. Fluid Mech.* **36**, 173–196.

Jonsson, I.G. & Carlsen, N.A. 1976 Experimental and theoretical investigations in an oscillatory turbulent boundary layer. *J. Hydraulic Research* **14**, 45–60.

Keiller, D.C. & Sleath, J.F.A. 1976 Velocity measurements close to a rough plate oscillating in its own plane. *J. Fluid Mech.* **73** (04), 673–691.

Kemp, P.H. & Simons, R.R. 1982 The interaction of waves with a turbulent current: waves propagating against the current. *J. Fluid Mech.* **130**, 73–89.

Kempe, T., Vowinckel, B. & Frőhlich, J. 2014 On the relevance of collision modeling for interface-resolving simulations of sediment transport in open channel flow. *Int.J. Multiphase Flow* **58**, 214–235.

Kim, J., Moin, P. & Moser, R. 1987 Turbulence statistics in fully developed channel flow at low reynolds number. *J. Fluid Mech.* **177**, 133–166.

Krogstad, P.-A., Andersson, H.I., Bakken, O.M. & Ashrafin, A. 2005 An experimental and numerical study of channel flow with rough walls. *J. Fluid Mech.* **530**, 327–352.

Krogstad, P.-A. & Antonia, R.A. 1994 Stucture of turbulent boundary layers on smooth and rough walls. *J. Fluid Mech.* **277**, 1–21.

Krogstad, P.-A., Antonia, R.A. & Browne, L.W.B. 1992 Comparison between rough and smooth-wall turbulent boundary layers. *J. Fluid Mech.* **245**, 599–617.

Krstic, R.V. & Fernando, H.J.S 2001 The nature of rough-wall oscillatory boundary layers. *J. Hydraulic Res.* **30**, 655–666.

Lee, M.J., Kim, J. & Moin, P. 1990 Structure of turbulence at high shear rate. *J. Fluid Mech.* **216**, 561–583.

Mahesh, K., Constantinescu, G., Apte, S., Iaccarino, G., Ham, F. & Moin, P. 2006 Large-eddy simulation of reacting turbulent flows in complex geometries. *J. Applied Mechanics* **73**, 374.

Mignot, E., Bartheleemy, E. & Hurther, D. 2009 Double-averaging analysis and local flow characterization of near-bed turbulence in gravel-bed channel flows. *J. Fluid Mech.* **618**, 279–303.

Mingmin, H. & Qiwei, H. 1982 Stochastic model of incipient sediment motion. *J. Hydraulic Div.* **108**, 211–224.

Moin, P. & Apte, SV 2006 Large-eddy simulation of realistic gas turbine combustors. *AIAA Journal* **44** (4), 698–708.

Moin, P. & Mahesh, K. 1998 Direct numerical simulation: A tool in turbulence research. *Annual Rev. Fluid Mech.* **30** (1), 539–578.

Mujal-Colilles, A., Mier, J.M., Christensen, K.T., Bateman, A. & Garcia, M.H. 2014 PIV experiments in rough-wall, laminar-to-turbulent, oscillatory boundary-layer flows. *Exp. Fluids* **55**.

Nelson, J.M., Schmeeckle, M.W., Shreve, R.L. & McLean, S.R. 2000 Sediment entrainment and transport in complex flows. *Selected Papers of the Int. Assoc. Hydraulic Research Symp. on River, Coastal and Estuarine Morphodynamics, Genova, Italy* .

Nikora, V., Goring, D., McEwan, I. & Griffiths, G. 2001 Spatially averaged open-channel flow over rough bed. *J. Hydraulic Eng.* **127**, 123–133.

Nino, Y., Lopez, F. & Garcia, M. 2003 Threshold for pArticle entrainment into suspension. *Sedimentology* **50** (2), 247–263.

Papanicolaou, A., Diplas, P., Evaggelopoulos, N. & Fotopoulos, S. 2002 Stochastic incipient motion criterion for spheres under various bed packing conditions. *J. Hydraulic Eng.* **128**, 369–380.

Raupach, M., Antonia, R. & Rajagopalan, S. 1991 Rough-wall boundary layers. *Appl.Mech.Rev* **44**, 1–25.

Raupach, M.R. & Shaw, R.H. 1982 Averaging procedures for flow within vegetation canopies. *Boundary-Layer Meteorol.* **22**, 79–90.

Raupach, M. & Thom, A. 1981 Turbulence in and above plant canopies. *Annual Rev. Fluid Mech.* **13**, 97–129.

Rosenthal, G.N. & Sleath, J.F.A. 1986 Measurements of lift in oscillatory flow. *J. Fluid Mech.* **164**, 449–467.

Schmeeckle, M.W., Nelson, J.M. & Shreve, R.L. 2007 Forces on stationary particles in near-bed turbulent flows. *J. Geophy. Res.* **112** (F02003).

Shields, A. 1936 Anwendung der ahnlichkeitsmechanik und der turbulentzforschung auf die geshiebebewegung, mitt. preuss. versuchsanst. wasserbau schiffbau, vol. 26, 26 pp. (english translation by w. p. ott and j. c. van uchelen, 1936. rep. 167, 36 pp., calif. inst. of technol., pasadena) .

Sleath, J.F.A. 1987 Turbulent oscillatory flows over rough beds. *J. Fluid Mech.* **182**, 369–409.

Sleath, J. 1995 Sediment transport by waves and currents. *J. Geophysical Reseach* **100**.

Sleath, J. 1999 Conditions for plug formation in oscillatory flow. *Continental Shelf Reseach* **13**.

Suekane, T., Yokouchi, Y. & Hirai, S. 2003 Inertial flow structures in a simple-packed bed of spheres. *AIChE Journal* **49** (1), 10–17.

Townsend, A.A. 1961 Equilibrium layers and wall turbulence. *J. Fluid Mech.* **11**, 97–120.

Valyrakis, M., Diplas, P., Dancey, C., Greer, K. & Celik, A. 2010 Role of instantaneous force magnitude and duration on particle entrainment. *J. Geophysical Research* **115**.

Wallace, J.M., Eckelmann, H. & Brodkey, R.S. 1972 The wall region in turbulent shear flow. *J. Fluid Mech.* **54**, 39–48.

Welch, P.D. 1967 The use of fast fourier transform for the estimation of power spectra: a method based on time averaging over short, modified periodograms. *IEEE Trans. Audio Electroacoust.* **15**, 70–73.

Wu, Fu-Chun & Chou, Y-Ju 2003 Rolling and lifting probabilities for sediment entrainment. *J. Hydraulic Eng.* **129**, 110–119.

Wu, Fu-Chun & Kuo-Hsin, Yang 2004 Entrainment probabilities of mixed-size sediment incorporating near-bed coherent flow structures. *J. Hydraulic Eng.* **130**, 1187–1197.

Yuan, J. & Piomelli, U. 2014*a* Numerical simulations of sink-flow boundary layers over rough surfaces. *Physics. Fluids* **26**.

Yuan, J. & Piomelli, U. 2014*b* Roughness effects on the Reynolds stress budgets in near-wall turbulence. *J. Fluid Mech.* **760**.

Yuan, J. & Piomelli, U. 2015 Numerical simulation of a spatially developing accelerating boundary layer over roughness. *J. Fluid Mech.* **780**, 192–214.